Improvement of the photocatalytic activity of titanium dioxide by forming composites with different materials

Ph.D. Dissertation

Boglárka Hampel

Supervisors:

Prof. Klára Hernádi

Dr. Zsolt Pap

Doctoral School of Environmental Sciences

Department of Applied and Environmental Chemistry

Faculty of Science and Informatics

University of Szeged

Szeged

2022

Table of Contents

List of abbreviations **4**

List of figures **5**

List of tables **8**

1. Introduction **9**

2. Literature review **10**

2.1. Advanced oxidation processes **10**

2.2. Heterogeneous photocatalysis **10**

2.3. About the acclaimed titanium dioxide **12**

2.4. Overview of the UV-, visible- and near-infrared light active photocatalysts **15**

2.5. Photocatalysis in near-infrared light **19**

2.6. General summary of upconversion luminescence materials **20**

2.6.1. The categories of the rare earth ions in the upconverting process 21

2.6.2. Energy transfer mechanism of the upconversion materials 22

3. Objectives of the thesis **25**

4. Experimental part **26**

4.1. Materials **26**

4.2. Synthesis of the titania-based composites **27**

4.2.1. With noble metal nanoparticles (binary composites) 27

4.2.2. With copper nanoparticles 29

4.2.3. With $NaYF_4$ and Au nanoparticles (ternary composites) 29

4.3. Methods and instrumentation **30**

4.4. Evaluation of the photocatalytic activity **31**

4.4.1. H_2 production 33

5. Results and discussion **34**

5.1. Composites consisting of TiO_2 and noble metals **34**

5.1.1. Characterization 34

5.1.2. Photocatalytic activity 40

5.1.3. Photocatalytic hydrogen production 41
5.1.4. Changing the ratio between the two noble metals 44
5.2. Composites consisting of copper nanoparticles and TiO_2 52
5.3. Composites consisting of lanthanide doped $NaYF_4$, TiO_2 and Au nanoparticle 55
5.3.1. Characterization 55
5.3.2. Photocatalytic activity 64
5.3.3. Photoluminescence measurements and the origin of the activity 67
6. Summary 69
7. Összefoglalás 73
8. Acknowledgements 77
References 78

List of abbreviations

AOP	Advanced oxidation process
AA	Aldrich anatase
AR	Aldrich rutile
BET	Brunauer-Emmett-Teller isotherm/method
CR	Cross-relaxation
CSU	Cooperative sensitization upconversion
DLS	Dynamic light scattering
DRS	Diffuse reflectance spectroscopy
EDAX	Energy dispersive X-ray analysis
ESA	Excited-state absorption
ET	Energy transfer
ETU	Energy transfer upconversion
GC	Gas chromatography
HPLC	High performance liquid chromatography
HRTEM	High resolution transmission electron microscopy
JCPDS	Joint committee of powder diffraction standards
NYF	Lanthanide doped $NaYF_4$
NIR light	Near-infrared light
PA	Photon avalanche
SEM	Scanning electron microscopy
SHG	Second harmonic generation
SPR	Surface plasmon resonance
STPA	Simultaneous two-photon absorption
TEM	Transmission electron microscopy
UV	Ultraviolet light
Vis	Visible light
XRD	X-ray diffraction

List of figures

Figure 1. Band structure of the semiconductors (*A =acceptors, D=donors).

Figure 2. The crystal structure of TiO_2: (a) rutile, (b) anatase and (c) brookite. This figure was taken from ref. [26], p. 892.

Figure 3. Comparing the number of publications in the past 15 years: it is clear that more and more published papers appear every year studying photocatalysis (information acquired using the Web of Science Core Collection, April, 2021, search parameters: TOPIC: (Photocata*) Timespan: 2005-2020.)

Figure 4. Comparing the published papers concerning photocatalysis in visible and near-infrared light in the past 10 years. (information acquired using the Web of Science Core Collection, April, 2021, search parameters: TOPIC: (*Photocatal**) AND TOPIC: (*visible*) *Timespan: 2010-2020*. and TOPIC: (*Photocatal**) AND TOPIC: (*Near-infrared*) *Timespan: 2010-2020.*

Figure 5. Mechanism of the near-infrared photocatalysis based on upconverting nanoparticle and UV or visible light active photocatalyst (*ET = energy transfer).

Figure 6. Single cell of cubic polymorph (a) and supercell of hexagonal polymorph of $NaYF_4$. This figure was taken from ref. [143], p. 5081.

Figure 7. The possible mechanisms of the upconversion processes, from left to right: excited-state absorption (ESA), energy transfer upconversion (ETU), cooperative sensitization upconversion (CSU), cross-relaxation (CR) and photon avalanche (PA). The red, violet, and green lines represent photon excitation, energy transfer, and emission processes. This figure was revised from ref. [125], p. 5.

Figure 8. The synthesis and purification of TiO_2-Au and/or Pt nanocomposites by the means of chemical reduction using in situ and impregnation as possible pathways of the reaction.

Figure 9. The used reactors for the determination of the photocatalytic activity (A-UV, B-visible, C-NIR).

Figure 10. The used reactors for the determination of the photocatalytic hydrogen production.

Figure 11. XRD patterns of different commercial TiO_2 photocatalysts used as base photocatalysts in the synthesis of titania/noble metal(s) nanocomposites.

Figure 12. The influence of the noble metals on the optical properties of three commercial titanias (A.-AA, B.-AR, C.-P25, D.-band gap energy comparison using the in situ sample series-right and impregnation series-left). The influence was significant when P25 was

considered as the base photocatalyst, while in the other cases no changes were observed in their spectra.

Figure 13. HR-TEM and STEM-HAADF micrographs of P25_is series, showing 2-4 nm sized Au and or Pt nanoparticles.

Figure 14. STEM-HAADF (b) micrograph, HR-TEM (d, f) images and EDS spectra (a,c and e) of P25_im-Au/Pt sample, showing the presence of both Au and Pt. No core shell particles and no alloys were detected, just nanoparticles, which show Pt and/or Au presence.

Figure 15. Noble metal nanoparticle size distribution of sample P25_is-Au/Pt, counting 100 nanoparticles. The distribution was nearly the same for all the materials.

Figure 16. The oxalic acid degradation performances after 1 h of the obtained nanocomposites under UV light. All the composites showed higher photocatalytic activity then their corresponding base photocatalyst. The photocatalytic performances after two hours were omitted at each composite degraded totally the oxalic acid.

Figure 17. The photocatalytic H_2 production capacities of the used nanocomposites. The bare photocatalyst were not shown, as they do not produce hydrogen under these experimental conditions.

Figure 18. DLS measurements of the composites prepared with most efficient reduction method, which was in most cases Au/Pt composites and their bare counterparts (A-P25, B-AA, C-AR).

Figure 19. The oxalic acid degradation performances after 1 h of the obtained nanocomposites under UV light. Only in the case of the AR based composites improved the photocatalytic activity the change in the composition.

Figure 20. Degradation curves for oxalic acid – those composites are marked which had the best activity for each base catalyst (P25, AA, AR).

Figure 21. Degradation curves of salicylic acid (A - P25 and its composites, B - AA and its composites, C - AR and its composites) – the AA based composites achieved higher activity than the base catalyst.

Figure 22. Comparison of the degradation of oxalic acid and salicylic acid of the samples – generally the P25 and AR based composites had higher activity for oxalic acid degradation than for salicylic acid.

Figure 23. The photocatalytic hydrogen production capacities of the composites. The obtained volume of H_2 is expressed in mL for each composite.

Figure 24. Time resolved hydrogen production rates of the composites which produced the most H_2 – the best value of all the samples is P25_im-Pt/Au.

Figure 25. Degradation of methyl orange under UV illumination (A.-P25 based composites, B.-AA based composites) - the composites did not show better activity than the corresponding bare titania. P25-based composites proved to be more efficient than the AA-based ones.

Figure 26. Photocatalytic degradation efficiencies of rhodamine B solution under UV light (A.-P25 based composites, B.-AA based composites) - the P25-based composites showed better activity than the AA-based ones.

Figure 27. Degradation of ketoprofen under the irradiation of UV light (A.-P25 based composites, B.-AA based composites) - some of the composites achieved better activity than the base catalyst but only in the case of P25.

Figure 28. H_2 evolution of the composites (A.-P25 based composites, B.-AA based composites), showing the enhanced H_2 production of P25-based composites.

Figure 29. A. - XRD patterns of the composites containing both NYF and TiO_2. The reflections of both materials can be observed, while the reflections of Au nanoparticles were not detectable. B. – XRD patterns of the composites without NYF. The dots indicate the reflections of TiO_2, while the stars indicate the reflections of NYF.

Figure 30. SEM micrographs of the prepared photocatalysts: the first column contains the base catalysts, while the second column contains their heat-treated counterparts.

Figure 31. EDAX spectrum of the sample named NYF-TiO_2_calc-Au. All of the constituent elements are present in the composite.

Figure 32. TEM micrograph of NYF-TiO_2_calc-Au: the arrows indicate the positions of the Au nanoparticles, which have spherical shape and an average size of 5–7 nm.

Figure 33. Particle size distribution curve for Au (A) and TiO_2 (B) nanoparticles. The average size of Au being 5-7 nm, while for TiO_2 12-14 nm.

Figure 34. The specific surface area of the composite samples determined by nitrogen adsorption.

Figure 35. DRS spectra of the prepared samples.

Figure 36. UV-visible spectrum of the gold nanoparticles.

Figure 37. Photocatalytic activity of the composites under UV light.

Figure 38. Photocatalytic activity of the composites under visible light.

List of tables

Table 1. The as produced commercially available titania based and noble metal nanoparticle composites.

Table 2. The as produced TiO_2, NYF and Au nanoparticle composites.

Table 3. Band gap energy values (eV) obtained from the DRS measurements, showing the effect of the noble metal nanoparticles on the optical properties of titania.

Table 4. The as produced composites of commercially available titanias and Au and Pt with the changed ratio.

Table 5. Primary crystallite mean size, the specific surface area, band gap energy of the composites.

Table 6. The degradation efficiencies under UV and visible light for the investigated samples.

1. Introduction

It is a known fact that, without water, there is no life because this is the compound that is the most common on Earth. Seventy-one percent of our planet is covered by water, of which 2.5% is fresh water, and the rest is saltwater (seas, oceans), while the human body contains approximately 60% of water. A sad fact is that the amount of potable water of the Earth is dropping drastically and is becoming more and more contaminated. A large number of pesticides, detergents, phenols, oil, and oil derivatives, etc., can be found in our environment, causing great damage.

Noting the severity of this global problem the next reasonable step was to look for solutions that could solve the purification of the contaminated waters. This is important not only for the current generation, but even more for the next one.

Besides traditional physical, chemical, and biological wastewater treatment technologies, various alternative methods have been developed for water purification, and this circle is expanding. This includes advanced oxidation processes (AOPs), whereby undesirable compounds are degraded via photolysis or generated reactive radicals (•OH radical) [1]. The most common AOPs are based on ozone [2], hydrogen peroxide (Photo-Fenton reaction: light $+Fe^{2+}+$ hydrogen peroxide) [1], and on heterogeneous photocatalytic methods [3].

The essence of heterogeneous photocatalysis is that when a semiconductor is irradiated with light of a proper wavelength, it could decompose the organic pollutant (*via* possible intermediates/in several steps) into CO_2 and H_2O. Moreover, this method is non-selective, meaning that organic pollutants of any kind can be degraded [4].

In my Ph.D. dissertation I investigated TiO_2 based ternary composites. The main idea was to broaden the applicability spectrum of titania by forming composites with different materials, such as with noble metal nanoparticles, copper nanoparticles, or with lanthanide doped $NaYF_4$ in order to utilize upconverted light as well. During the experiments I had to recognize that sometimes the theory does not match the practice, and so I tried to find link between the properties of the composites and their photocatalytic activity.

2. Literature review

2.1. Advanced oxidation processes

Advanced oxidation processes (AOPs) are used for the decomposition of organic pollutants in air and water [5]. AOPs require the generation of free reactive radicals (hydroxyl radicals) in sufficient amount to be efficient in water purification [6,7]. Hydroxyl radicals are one of the strongest oxidizing agents: they are reactive, none-selective, thus capable of degrading organic pollutants [8]. They are considered to be the most favorable among the powerful oxidants, as they do not generate additional waste, they are not toxic, have a short lifetime and they are not corrosive [2].

The following methods are used for hydroxyl radical generation: chemical, photochemical, sonochemical or radiolysis-based methods (and combinations thereof) [9]. These free radicals can react with the available organic molecules, breaking them down to fragments [10], until the complete mineralization [11].

The advanced oxidation processes can be divided into four categories:

1. processes based on oxidizing agents (ozone, hydrogen peroxide)
2. methods based on radiolysis
3. ultraviolet or high energy vacuum ultraviolet (VUV) photolysis methods
4. heterogeneous photocatalytic process using illuminated semiconductor nanoparticles.

Although the *heterogeneous photocatalysis* in terms of efficiency remains superior compared to the other methods, it needs to be highlighted that in terms of environmental impact and operating costs it comes inferior to the others.

This is the reason why I chose to study this latter topic in detail for my Ph.D. dissertation.

2.2. Heterogeneous photocatalysis

Heterogeneous photocatalysis is one of the advanced oxidation processes, which might provide a favorable alternative to solve one of the major problems of our time: the pollution of our natural waters [12–14]. This process is based on the presence of a solid semiconductor photocatalyst [15].

Semiconductors are materials that, depending on the circumstances, can act as both conductors and insulators. Their band structure is illustrated in **Figure 1.** Within the

electron band structure of semiconductors, the highest occupied molecular orbital is called conduction band, while the lowest unoccupied molecular orbital is the valence band [16]. In the ground state the valence electrons are located in the valence band. The difference between the two energy levels is the band gap, which indicates the energy level where electrons cannot be present. If the semiconductor is excited with an energy source (UV/ visible/ near-infrared (NIR) light) greater than, or equal to the energy value of the band gap, the electron in the valence band is excited and then promoted to the conduction band, leaving a positively charged so-called "hole" (h^+) [17–19]. If this electron is not used in a reaction, recombination takes place, during what heat is released and the electron is returned to the valence band.

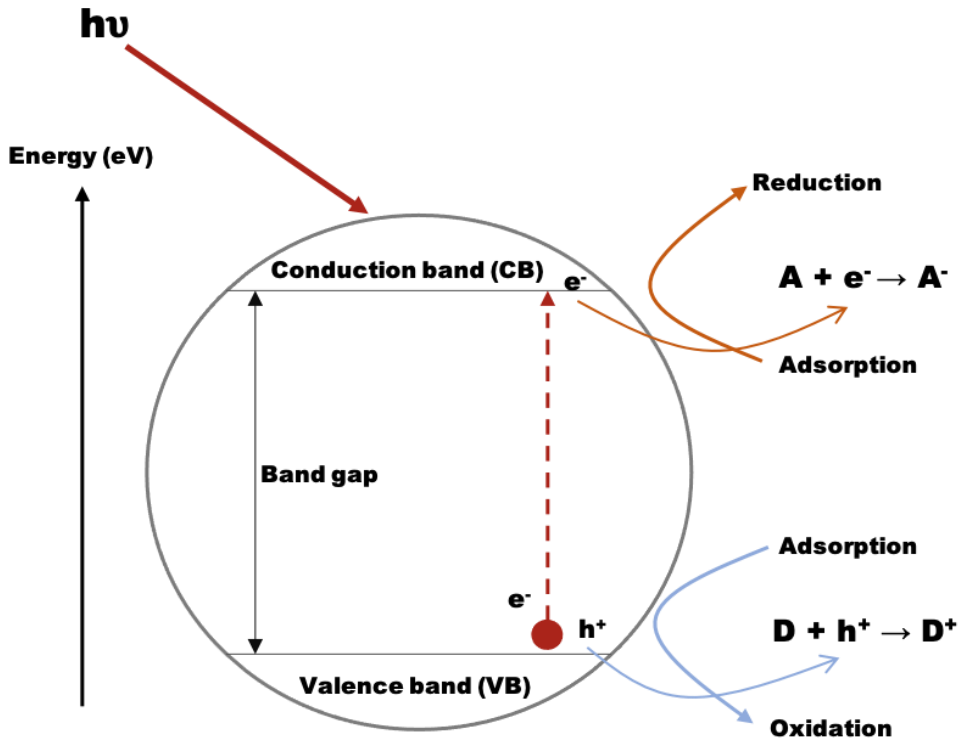

Figure 1. Band structure of the semiconductors (*A =acceptors, D=donors).

The presence of electron donors (D) and acceptors (A) is necessary on the surface of the excited semiconductor in order to start a series of chemical reactions, which lead to mineralization. If TiO_2 is used as an example for the excited semiconductor photocatalyst, these reactions may proceed as follows:

$TiO_2 + h\nu \rightarrow TiO_2 (h_{VB}^+ + e_{CB}^-)$ (1)

$h_{VB}^+ + H_2O \rightarrow \bullet OH + H^+$ (2)

$h_{VB}^+ + OH^- \rightarrow \bullet OH$ (3)

$$\bullet OH + \text{pollutant} \rightarrow H_2O + CO_2 \quad (4)$$

$$e_{CB}^- + O_2 \rightarrow O_2^{\bullet -} \quad (5)$$

$$O_2^{\bullet -} + H^+ \rightarrow \bullet OOH \quad (6)$$

$$O_2^{\bullet -} + \text{pollutant} \rightarrow H_2O + CO_2 \quad (7)$$

$$\bullet OOH + \text{pollutant} \rightarrow H_2O + CO_2 \quad (8)$$

In the first step TiO_2 is excited, where charge carriers are generated (1), which can migrate to the surface and initiate redox reactions with adsorbates [20].

The positive holes can oxidize OH^- or H_2O to •OH (2), (3).

Then the hydroxyl radicals can oxidize the organic pollutants, transforming them to H_2O, CO_2 and other inorganic compounds (4).

On the other side the electrons in the conduction band can be easily trapped by molecular oxygen adsorbed on TiO_2, which can be reduced to superoxide radical anion ($O_2^{\bullet -}$) (5).

The superoxide radical anion can further react with H^+ to generate hydroperoxyl radical (•OOH) (6).

These reactive oxygen species play an important role in the oxidative processes, which lead to the degradation of the pollutants (7) (8).

2.3. About the acclaimed titanium dioxide

Titanium is the ninth most common element in the Earth's crust, and interacts with oxygen to form titanium oxides, commonly found in ores, indigenous dusts, sands and soils [21].

As shown in **Figure 2.**, titanium dioxide generally appears in three crystalline structures: rutile, anatase and brookite [22]. Rutile and anatase have tetragonal, while brookite has orthorhombic crystal system [23]. Among these, rutile is the stable form, anatase and brookite being metastable, which easily transform to rutile upon heating [24]. That is the reason why rutile is the most commonly used in the industry. The band gap energy of rutile is known to be 3 eV, of anatase 3.2 eV, while of brookite 3.0-3.6 eV [25].

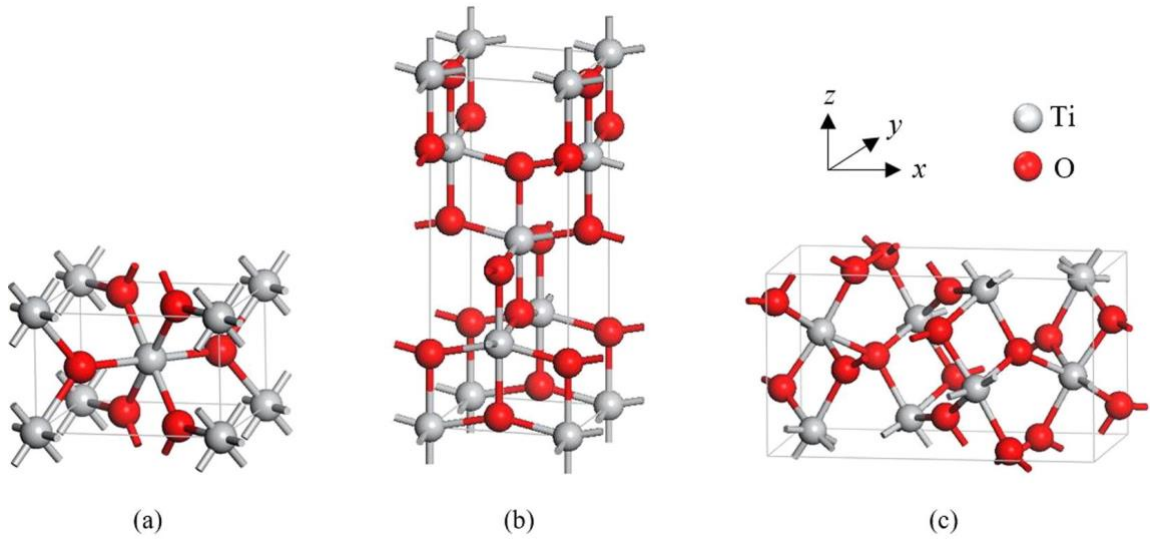

Figure 2. The crystal structure of TiO_2: (a) rutile, (b) anatase and (c) brookite. This figure was taken from ref. [26], p. 892.

TiO_2 can be found in all kind of paints, printing inks, plastics, different type of papers, synthetic fibers, rubber, condensers, paint pigments, crayons, and in ceramics as whitening agents [27]. Titanium dioxide nanoparticles are used in food industry (E171), although starting from July 2022 the European Commission has banned the use of TiO_2 in food additives because it is considered to be no longer safe. Titanium dioxide is also utilized in the processing and in the packing of food [28]. Titania can often be found in different cosmetic products, such as toothpaste, sunscreen, etc. [29] and it is often used as an important component in self-cleaning tiles, windows [30]. Among the many applications of TiO_2 what is currently the most interesting – at least for my dissertation – is heterogeneous photocatalysis.

It started back in 1972, when Fujishima and Honda used TiO_2 for hydrogen production, using UV light [31]. After this, plenty of studies appeared in the field of photocatalysis [32–35]. After almost 50 years, TiO_2 is still the most studied photocatalyst, because it is rather cheap, not toxic for the environment, and can produce extremely oxidizing holes [36].

For photocatalytic purposes mainly rutile and anatase TiO_2 was used. The anatase TiO_2 crystals consist the thermodynamically stable {101} facets, rather than the much more reactive {001} facets [37]. However, the production of high-quality single crystal anatase titania with large number of the reactive facets holds difficulties [38]. In addition to this, anatase has a higher density of active sites [39]. Moreover, the concentration of oxygen vacancies on anatase is higher than on rutile, which means the charge separation efficiency is increased also [40]. The larger band gap of anatase results in a bit higher redox capability than rutile [39]. Thanks to the above-mentioned favorable properties anatase is generally more active than rutile. In

order to improve the photocatalytic activity, attempts were made to form TiO_2 heterojunction between its crystalline structures. The best known anatase/rutile containing material is P25 (previously manufactured by Degussa but now made by Evonik Industries), which is often used as a reference catalyst [41]. This material is made up of 89 wt% anatase and 11 wt% rutile and it is obtained *via* flame pyrolysis [42].

The major drawback of titanium dioxide is that it can be excited only by UV light [43]. Therefore, attempts were made in order to extend the excitation spectrum of TiO_2 [44]. It is well known that the photocatalytic activity can be increased if different (noble) metals are deposited on the surface of semiconductors, such as Ag [45–47], Au [48–50], Pd [51–53], Pt [54–56], Cu [57,58]. Composites were formed with non-metallic elements: S [59,60], N [61,62] or nanocarbons, or with semiconductors of narrower band gap [63]. The conclusions are interesting from the point of view of composition of the composites. It was found that, the best photocatalytic activity was achieved when less than 5 wt.% of noble metal was present on the semiconductors' surface [64,65]. When Au and Ag metals were used for the preparation of ternary composites the ratio of them is also important: 1:3 [66] or 1:4 [67] metal ratio was used. Even if there are still some controversies about the enhancement mechanism, is widely agreed that noble metal particles on the surface of the semiconductor oxide can act as electron-traps, storing and shuttling photogenerated electrons, facilitating the charge carrier separation and reducing the recombination rate [68]. It was also proved that the use of bimetal nanoparticles could lead to enhanced activity as well. Some earlier experiments were already published concerning this subject and there it was shown that 0.3-1.0 wt% Pt and 1.0-2.0 wt% Au were beneficial to the activity [69].

During my experiments for my dissertation the two investigated noble metals were gold and platinum. These two can be also used in alloy systems as suggested above and were tested in various applications. The alloys made of Au and Pt were used as electrocatalyst for the oxidation of formic acid and the results showed that the composition of the alloy also influenced the electrocatalytic activity. The suggested composition of the alloy was the 35 wt% Pt and 65 wt% Au [70]. Au/Pt nanoparticles were also immobilized to polytyramine for the DNA hybridization detection [71], while another study presents Au-Ag alloys as plasmonic photocatalysts that exhibit better activity towards stearic acid degradation then TiO_2 [72]. Pd and Pt alloys were deposited on TiO_2, and the photocatalytic activity was evaluated for methyl orange decomposition. The small particle size and small amount of the nanoparticles on high surface area TiO_2 enhanced the photocatalytic activity [73]. For phenol degradation the best activity was achieved when 0.5 wt% Pt - 0.5 wt% Pd was deposited on TiO_2 [74]. Platinum

was also used as cocatalyst in a system made of titania and Sn and it was proved that it not only helps the prevention of the charge recombination, but it is present also as a catalytic active site [75].

In the other part of my dissertation, with the purpose of achieving cheaper photocatalysts I used copper nanoparticles beside titanium-dioxide. Copper nanoparticles possess many intriguing properties which provide them many applications, such as antibacterial, antifungal, and antiviral applications [76–78]. A great deal of work can be found concerning the application of copper nanoparticles in electrochemistry [79,80] and electroanalysis [81]. Interesting applications, such as the enhancement of thermal conductivity of ethylene glycol, can also be found [82]. Among the publications, several show the application of copper nanoparticles in the field of catalysis [83–85]. Forming composites with TiO_2, Cu nanoparticles proved to be good as photocatalysts, too. Many publications can be found on the deposition of Cu nanoparticles on TiO_2. It was shown that depositing 1–10% Cu on titania issued in beneficial effect on the decomposition of acetic acid into biogas and hydrogen [86], on the degradation of methyl orange [87], CO_2 photoreduction [88], aqueous hexavalent chromium [89], or humic acid degradation [90]. In another study, 2.5 wt.% Cu doped TiO_2 composites showed a higher reaction ability than P25 [91]. Researchers proved that, if copper nanoparticles are present in a higher amount, CuO crystallization can take place [92].

2.4. Overview of the UV-, visible- and near-infrared light active photocatalysts

If one types the word ‘photocatalysis’ in Google© there are almost 4 million results, so it can be safely said that this is an increasingly researched area, especially in the past 15 years, which is illustrated in **Figure 3.** as well.

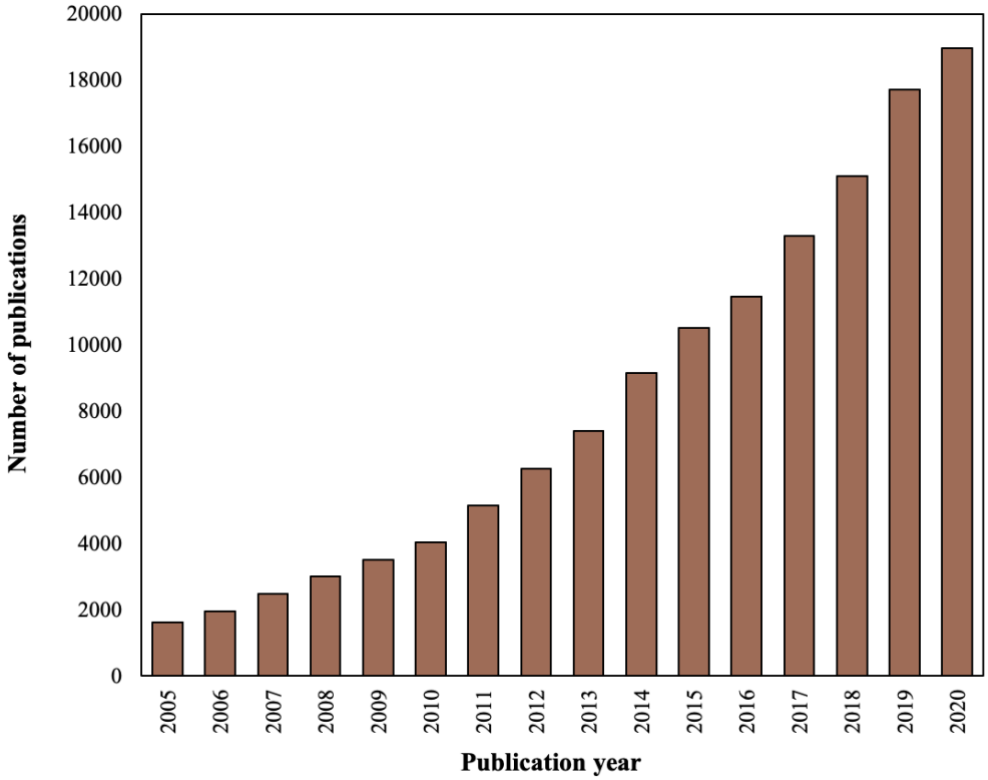

Figure 3. Comparing the number of publications in the past 15 years: it is clear that more and more published papers appear every year studying photocatalysis (information acquired using the Web of Science Core Collection, April, 2021, search parameters: TOPIC: (Photocata*) Timespan: 2005-2020.)

It is worth mentioning that there is photocatalysis in UV light beyond titania. ZnO was successfully used in photocatalysis as a substitute for titanium-dioxide [93–95]. Another prosperous candidate is ZrO_2 [95–97]. Reduced graphene oxide (rGO) with its zero band gap and fast internal electron transport is a newly trending co-photocatalyst [98]. It has been used along with $NaTaO_3$ [99], ZnO [100,101], V_2O_5 [102].

As the UV light is only ~5% of the sunlight, it was reasonable to broaden the set of photocatalysts in order to achieve more, which are active in higher wavelengths as well. One of the most popular visible light driven photocatalysts is CdS [103], however the photogenerated electron-hole pairs have high recombination rate [98]. Therefore composites were formed with Ni nanosheets [104], MoS_2 [105], ZnO [106], graphene [107], etc.. There is a series of oxides, which proved to be suitable for visible light photocatalysis, such as: WO_3 [108], CuO [109], Ag_2O [110], Bi_2WO_6 [111] or $BiVO_4$ [112]. Before moving on to the next thought it is essential mentioning the carbon-based materials, which also proved to be efficient: carbon quantum dots [113], carbon nanodots [114], graphitic carbon nitride [115], carbon

nanotubes [116], graphene [117]. Carbon nanospheres have also been successfully used as template [118–122].

The third light-range for photocatalysis is the near-infrared (NIR) light. This area is not as well-studied, as the previous two, it still has some challenges for the researchers [44]. It has to be highlighted that most photocatalysts do not have activity in NIR light, although the structure of composites allows to absorb the NIR light, convert it to shorter wavelengths and use that for photocatalysis [123]. For this upconversion process lanthanides and lanthanide fluorides are the most fitting, because the setup of their energy levels [124], $NaYF_4$ being the most commonly used one [125].

Many oxides have been used beside the upconverting materials for photocatalysis. Among these TiO_2 is the most studied candidate. The core-shell approach is widely used, as this formation of composites promotes the process of upconversion photocatalysis. If the upconverting material is the core then it is protected from surface quenching and the energy transfer could be increased [126]. The photocatalytic activity of TiO_2 was improved *via* forming core-shell composites with $NaYF_4$:Yb, Tm and CdS quantum dots [127]. The CdS quantum dots were deposited on the surface of TiO_2 shell, while $NaYF_4$:Yb, Tm was the core. The photocatalytic activity was investigated in white light, visible and near-infrared light: under any irradiation the composite had better activity than the pure TiO_2, what can be contributed to the fact that the quantum dots can extend the absorption region of TiO_2 and the upconversion effect of $NaYF_4$:Yb, Tm. Double core-shell structures were also prepared. First a core-shell structure was prepared as follows: $NaYF_4$:Yb^{3+}, Tm^{3+} was prepared as the core, then $NaYF_4$:Yb^{3+}, Nd^{3+} was deposited as a shell covering it, and lastly TiO_2 became the second shell of this core-shell structure [128]. This system may seem complicated at first but has 4.4 times as high degradation rate constant of rhodamine B under 980 nm laser irradiation than $NaYF_4$:Yb^{3+}, Tm^{3+}-TiO_2. Another way to the double core-shell structure is a double-shell formation of composites. β-$NaYF_4$:Yb^{3+},Tm^{3+}/Er^{3+} nanocrystals were the core, SiO_2 as a mid-shell and TiO_2 as the outer shell [129]. These structures were applied in the photocatalytic degradation of rhodamine B. β-$NaYF_4$:Yb^{3+},Tm^{3+} or β-$NaYF_4$:Yb^{3+},Er^{3+} based catalysts had similar activity in NIR light, both of them decomposed all of the pollutant, by contrast those materials which did not contain these upconverting materials showed no photocatalytic activity under NIR light at all.

Among the noble metal nanoparticles Au had been studied the most for upconversion photocatalysis. This, beside increasing the lifetime of electron-hole pairs is due to the surface plasmon resonance (SPR) exhibited by gold nanoparticles [130]. This SPR-induced hot

electrons can be directly induced from gold nanoparticles to the conduction band of a semiconductor [131]. Using this information researchers attempted to achieve composites by combining SPR and upconversion effects. One study presents the design of a composite containing TiO_2, upconverting Yb^{3+} and Er^{3+} doped $NaYF_4$ and plasmonic gold nanoparticles [132]. Results showed that by employing SPR and upconversion effects together the solar light utilization can be improved. Rare earth vanadates and gold nanoparticle composites had been studied as well. Au nanoparticles were deposited onto $NdVO_4$, which resulted great photocatalytic activity for the degradation of methyl orange under solar light [133]. $GdVO_4$:Eu and Au core-shell nanoparticles were synthetized [134]. It was found that these materials had high specific surface area and they integrate SPR and fluorescence which suggests that it may be potential in photocatalytic applications.

In **Figure 4.** a comparison of the published papers concerning photocatalysis in visible and near-infrared light in the past 10 years can be seen. The reason why the UV photocatalysis is not presented in the chart is that there are far more publications on this topic. If all three sections would be presented on one diagram, then it would be harder to interpret, since the numbers for UV overshadow the others. In **Figure 4.** the number of the published articles from 2010 to 2020 about near-infrared photocatalysis is presented in the inner circle, while in the external are the ones about visible light. It can be seen that the visible light-driven photocatalysis is still much more researched then the NIR. This gave the motivation to complement my study with photocatalysis under NIR light as well and upconversion luminescence materials.

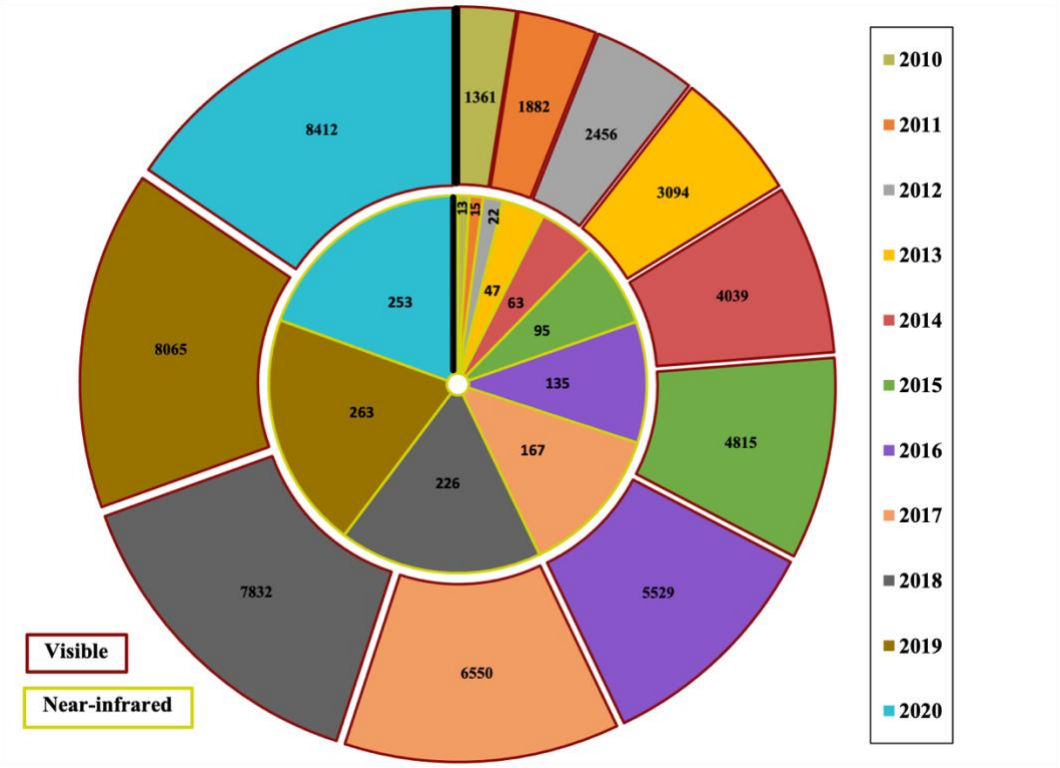

Figure 4. Comparing the published papers concerning photocatalysis in visible and near-infrared light in the past 10 years. (information acquired using the Web of Science Core Collection, April, 2021, search parameters: TOPIC: (*Photocatal**) AND TOPIC: (*visible*) *Timespan: 2010-2020*. and TOPIC: (*Photocatal**) AND TOPIC: (*Near-infrared*) *Timespan: 2010-2020.*

2.5. Photocatalysis in near-infrared light

As mentioned beforehand, photocatalysis is an increasingly researched are. However, the most studied light-ranges are the UV and visible. A new approach to utilize more of the sunlight is developing composite-systems, which show photocatalytic activity in near-infrared light, which makes up ~44% of the sunlight [135].

Since most of the photocatalysts do not have photocatalytic activity in near-infrared light, this is an indirect realization of photocatalysis [98]. During the process, the NIR light is converted to UV or visible light, which is then utilized for the degradation [136]. The upconversion process takes place as described in section 2.6.1. The presence of a UV or visible light active photocatalyst is essential beside the upconverting nanoparticle, because the actual photocatalysis will be performed by them [124]. The schematic illustration of the mechanism of NIR photocatalysis is presented in **Figure 5.** In brief, the upconverting nanoparticle converts

the NIR light to UV or visible light. The photocatalyst uses this upconverted light to oxidize organic pollutants [137].

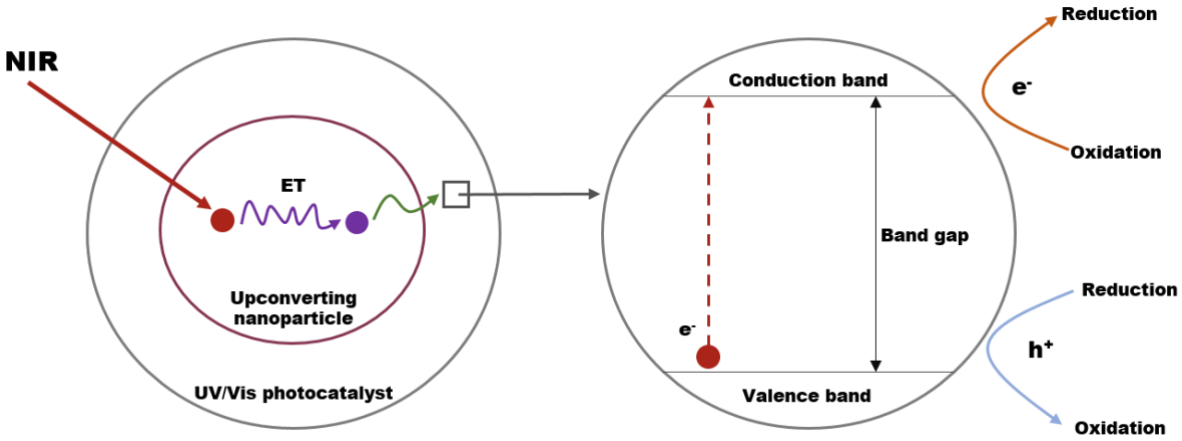

Figure 5. Mechanism of the near-infrared photocatalysis based on upconverting nanoparticle and UV or visible light active photocatalyst (*ET = energy transfer).

2.6. General summary of upconversion luminescence materials

Luminescence occurs when an atom or molecule emits radiation, after absorbing photons, radiation, chemical or biochemical reactions [138]. This phenomenon is provoked by the movement of the electrons within the material from higher energy levels to lower ones, resulting the emission of light without giving off heat. The two main types of luminescence are: fluorescence and phosphorescence. The difference between these two is the delay between the absorption and emission of light. In case of fluorescence the endurance of the light emission is relatively short, 10^{-6}-10^{-8} s, while for phosphorescence is 10^{-6} s and longer (sometimes even minutes, hours) [139]. Stokes law states that emitted light is always of longer wavelength than the absorbed one [140]. The photoluminescent materials generally follow this. In some cases, the emitted photon has higher energy than the absorbed one, this happens to be the anti-Stokes shift, which appears in three ways: simultaneous two-photon absorption (STPA), second-harmonic generation (SHG), and upconversion [141]. Among these the upconversion will be discussed in detail.

2.6.1. The categories of the rare earth ions in the upconverting process

A typical upconversion material consists of two components: an inorganic host matrix and doping ions [142]. Most of these materials include trivalent rare earth ions (Pr^{3+}, Nd^{3+}, Er^{3+}, Tm^{3+}, Yb^{3+}), which act as active components [143]. The reason why these ions play such important role is due to their relevant electronic states in their inner 4f shell [144]. The outer 5s and 6p shells participate in the bonding, however the f states are insensitive to the nature of the host lattice, resulting a great number of excited f states. These states lead to upconversion, as their lifetime is long enough to be part of the process. Generally, inorganic crystals do not show upconversion luminescence at room temperature [145]. Accordingly, lanthanide dopants are added in low concentration to the host lattice, in the role of localized luminescence centers [146]. After excitation, the dopant ion radiates to a higher energetic state, which is the result of the non-radiative transfer of the energy from another dopant ion. The activator is the ion that emits the radiation, while the donator of the energy is the sensitizer [147].

Activators: The upconversion process requires multiple metastable levels, that is why the lanthanides are used most of the times [148]. The lanthanides, from lanthanum to lutetium, fill up the 4f shell and their most stable oxidation state is as trivalent ions (Ln^{3+}). Most of lanthanide ions have more than one excited 4f energy level, except La^{3+}, Ce^{3+}, Yb^{3+} and Lu^{3+}. Hypothetically, all lanthanides could be used for upconversion, yet for efficient upconversion process there is one more condition. The energy difference between each excited level and its lower-lying intermediate level (ground level) shall be close enough to promote photon absorption and energy transfer. The most frequently used activators are Er^{3+}, Tm^{3+} and Ho^{3+}, because of their ladder-like arranged energy levels [149].

Sensitizers: The concentration of the doping ion is crucial. Operating with high doping level may cause the quenching of excitation energy [150]. Therefore, the concentration of the activator has to be low and precisely adjusted. Nevertheless, if the doping level is too low, the absorption of the pump light is also low, which results in low emission luminescence efficiency. Thus, sensitizers are essential because they are strongly absorbing and provide efficient energy transfer to the activator. Yb^{3+} is the most widely used sensitizer for Er^{3+} and Tm^{3+}. Yb^{3+} has a very simple energy level structure, with only one 4f level. The separation energy between the ground and excited states of Yb^{3+} corresponds to the transient states of Er^{3+}, this promotes the efficient energy transfer between the two ions [147].

Host materials: Choosing the host material is just as important step as choosing the dopant ions. The lattice of the host material determinates the distance between the dopant ions, their relative spatial position, coordination numbers, and the type of anions surrounding the dopant [151]. The two most important properties of the host material are: low phonon energy and small lattice mismatch to the dopant ions [152]. Heavy halides, like chlorides, bromides, and iodides show low phonon energies, but they are hygroscopic and of limited use [153]. Oxides have high chemical stability, but their phonon energies are relatively high. By contrast, fluorides show low phonon energies and high chemical stability, that is why they are the most frequently used as host materials for upconversion [154]. Among these the most widely used are Na^+ and Ca^{2+} fluorides, particularly, $NaYF_4$ appears to be the most efficient one [155].

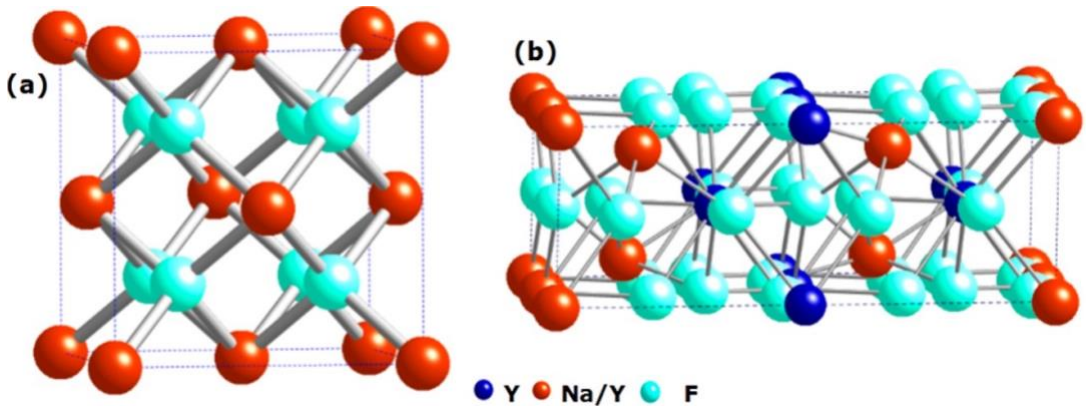

Figure 6. Single cell of cubic polymorph (a) and supercell of hexagonal polymorph of $NaYF_4$. This figure was taken from ref. [156], p. 5081.

$NaYF_4$ is widely used in various application fields, like flat panel displays[157], sensing [158], solar-energy harvesting [159], biological sensing [160] or as fluorescent probes for biomedical imaging [161]. $NaYF_4$ has two phases: hexagonal and cubic (**Figure 6.**), however for the optical application the hexagonal phase is the superior one [162]. This can be explained by the fact that in hexagonal phase are less nonharmonic phonon modes [163].

2.6.2. Energy transfer mechanism of the upconversion materials

Typically, upconversion is a nonlinear optical process, when two or more photons are absorbed in a row, which results in real intermediate energy states and luminescence is emitted with a wavelength shorter than the absorbed light, therefore it can be considered as an anti-Stokes mechanism [125]. There are five main upconversion mechanisms, which are presented in **Figure 7.**: excited-state absorption (ESA), energy transfer upconversion (ETU), cooperative sensitization upconversion (CSU), cross-relaxation (CR) and photon avalanche (PA).

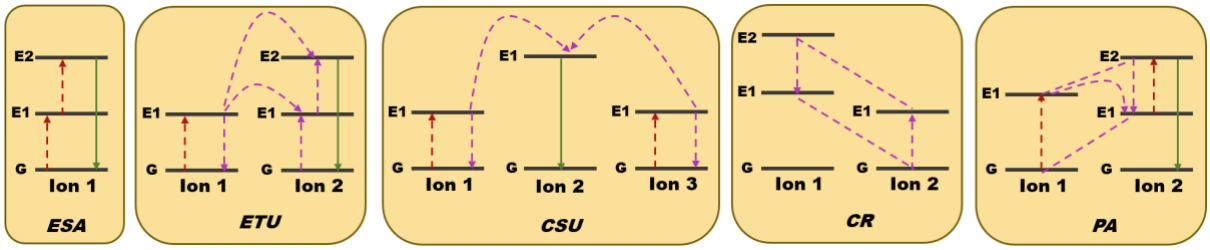

Figure 7. The possible mechanisms of the upconversion processes, from left to right: excited-state absorption (ESA), energy transfer upconversion (ETU), cooperative sensitization upconversion (CSU), cross-relaxation (CR) and photon avalanche (PA). The red, violet, and green lines represent photon excitation, energy transfer, and emission processes. This figure was revised from ref. [152], p. 5.

Excited-state absorption (ESA): the sequential absorption of pump photons by a single ground-state ion. In **Figure 7.** a three-level system is presented, where the ion is excited from ground state (G) to E1 level. During this another pump photon has the possibility to promote the ion from E1 level to the higher-lying E2 level. This results the upconversion, before it sets back to the ground state [164]. Therefore, the upconversion will take place from the E2 level. Highly adequate ESA occurs when the lanthanide ion has a ladder-like arrangement of the energy states. Only a few lanthanide ions, like Er^{3+}, Ho^{3+}, Tm^{3+} and Nd^{3+} have such energy level structures [165].

Energy transfer upconversion (ETU): very similar to ESA, as they both operate with sequential absorption of two photons. The difference between them is, that ETU process requires two neighboring ions: Ion1 as a sensitizer, while Ion2 as an activator (**Figure 7.**). As it is illustrated in **Figure 7.**, the sensitizer ion absorbs the pump photons, which excites it from the ground state to the metastable E1 energy level. Ion1 successively transfers this harvested energy to the ground state and to the excited state E1 level of Ion2, exciting Ion2 to its upper emitting state E2, whilst the sensitizer ion relaxes back again to the ground state [166]. The efficiency of ETU process strongly depends on the concentration of the sensitizer and activator ions, as it determinates the average distance between the neighboring ions.

Cooperative sensitization upconversion (CSU): involves the presence of three ion centers. As shown in **Figure 7.** Ion1 and Ion3 act as sensitizers: after absorbing pump photons, they both are excited to the excited state E1. Both Ion1 and Ion3 will interact with Ion2 (activator) and will excite it to the higher state E1 by transferring the absorbed energy simultaneously and cooperatively. The excited Ion2 can emit the upconverted photon by relaxing back to the ground state [125]. Although CSU has lower efficiency then ESA or ETU,

it provides opportunity to gain high-resolution imagining, which is not possible from any other upconverting process.

Cross-relaxation (CR): energy transfer process between two ions. This occurs from ion-ion interaction, where Ion1 transfers a part of its absorbed energy to Ion2. The process is shown is **Figure 7** and it can be described as follows: E2 (Ion1) + G (Ion2) → E1 (Ion1) + E1 (Ion2). In this process Ion1 and Ion2 can either be the same or different, and Ion2 in some cases can be in excited form. The CR efficiency depends on the dopant concentration. This process is responsible for 'concentration quenching mechanism' of emission, however it can be used for tuning emission color of upconversion materials, as well as for composing efficient photon avalanche mechanism [164].

Photon avalanche (PA): requires a certain threshold of excitation power. If the pump intensity is below the threshold upconversion luminescence barely appears, while if it is above it, then stronger upconverted luminescence occurs. PA process is a circle, including ESA for excitation light and CR that produces feedback. The process starts with the population of the E1 level of Ion2 by non-resonant weak ground-state absorption, which is followed by the ESA process populating the emitting E2 level. After this comes a CR process: E2 (Ion2) + G (Ion1) → E1 (Ion2) + E1 (Ion1), both ions occupy the intermediate level E1. The two ions easily populate level E2, to launch cross-relaxation and increase the E2 level population by ESA, which produces upconversion emission [167].

3. Objectives of the thesis

After finishing my B.Sc. and M.Sc. programs at the Babeș-Bolyai University I started my Ph.D. studies at the Doctoral School of Environmental Sciences in the Department of Applied and Environmental Chemistry.

If I had to sum up my objectives for my doctoral studies in a few words that would be: **to improve the photocatalytic activity of TiO_2**. Of course, if this were so easy, I would stop right here, but I'm not going to, since my aims include multiple steps and methods, which I would like to present in the next few lines.

For the first, crucial step of my research, as a preliminary study I am going to prepare binary composites by the simultaneous deposition of **gold and platinum nanoparticles** on **three different commercial titania** photocatalysts: *Evonik Aeroxide P25, Aldrich rutile, and Aldrich anatase*. I intend to use two synthesis strategies: **in situ and impregnation**. As for the noble metal deposition routes also two reduction approaches were proposed: **two sequential** (Au/Pt, Pt/Au) and **one simultaneous** (Au&Pt).

After processing the first round of results I am going to select the samples that most efficiently decompose oxalic acid or samples that produce the most hydrogen. For the sake of further fine-tuning, from each series of composites - made with the best in situ and impregnation – I am going to change the composition. I plan to modify the initial ratio between the two noble metals (0.5-0.5%) to *0.25% - 0.75%* and *0.75% - 0.25%*, respectively.

With the aim of searching for a *cheaper method* of preparing composites with TiO_2. I plan to deposit **copper nanoparticles** on two of the previously mentioned commercial titanias: *Evonik Aeroxide P25* and *Aldrich anatase.*

Considering the part presented so far complete, I got a new idea of how to improve the photocatalytic activity of titania even further. My new target was to obtain composites with anatase TiO_2, gold nanoparticles and $Yb^{3+,}$ Er^{3+} and Tm^{3+} doped $NaYF_4$. Theoretically, TiO_2 and gold nanoparticles can utilize the upconverted light, derived from the lanthanide doped $NaYF_4$.

The morphological and structural properties of the prepared materials will be studied/investigated by using *XRD, SEM, EDAX, TEM, HRTEM, BET method, DLS, DRS and photoluminescence measurements*. The evaluation of the *photocatalytic performances* of the composites will be carried out under ***UV, visible and NIR irradiation***, through *degradation of oxalic acid, salicylic acid, rhodamine B, methyl orange, ketoprofen or through photocatalytic hydrogen production*.

4. Experimental part

4.1. Materials

During the experiments, the following materials were used without further purification: Evonik Aeroxide P25 (89 wt. % anatase, 11 wt. % rutile; 99.5% trace metal basis, with a surface area of 56 $m^2 \cdot g^{-1}$), Aldrich anatase (99.7 % trace metal basis, with a surface area of 45 $m^2 \cdot g^{-1}$) and Aldrich rutile (99.995% trace metals basis, with a surface area of 50 $m^2 \cdot g^{-1}$) – will be henceforward denoted as P25, AA and AR, respectively. The AA and AR nanopowders were purchased from Sigma-Aldrich, the P25 from Evonik Aeroxide. For the synthesis of TiO_2 the following materials were used: isopropanol (C_3H_8O, 100%, VWR); diethylenetriamine (DETA, $C_4H_{13}N_3$, Sigma-Aldrich); titanium isopropoxide (97%, $Ti[OCH(CH_3)_2]_4$, Aldrich) and ethanol (C_2H_5OH, VWR).

The gold precursor was $HAuCl_4 \cdot 4H_2O$ (99.99 %; trace metal basis, Sigma-Aldrich) and it was used as a 12.7 $mmol \cdot L^{-1}$ aqueous solution, the platinum precursor was $H_2PtCl_6 \cdot 6H_2O$ (37.5 % Pt basis; Merck) and it was used as a 11.87 $mmol \cdot L^{-1}$ solution, while the copper precursor was $CuCl_2$ (≥99.995% trace metals basis; Sigma-Aldrich) and it was used in a 0.3 $mmol \cdot L^{-1}$ aqueous solution. Trisodium citrate ($Na_3C_3H_5O(COO)_3$) (99.99 % purity; Alfa-Aesar) was used as a solution of 0.063 $mmol \cdot L^{-1}$ for the stabilization of the (noble) metal particles' size because of its inhibitory role in aggregation. During the preparation, the sodium borohydride solution acted as a reducing agent. For the reduction of the (noble) metal precursors, sodium borohydride ($NaBH_4$; 96 % purity; acquired from Merck) was used as a solution of 0.15 $mol \cdot L^{-1}$.

For the lanthanide doped $NaYF_4$ (NYF) the following materials were used: $Y(NO_3)_3$ (0.5 $mol \cdot L^{-1}$), $Yb(NO_3)_3$ (0.5 $mol \cdot L^{-1}$), $Er(NO_3)_3$ (0.01 $mol \cdot L^{-1}$), and $Tm(NO_3)_3$ (0.01 $mol \cdot L^{-1}$) stock solutions (all purchased from Alfa Aesar, 99.9%); NaF (Fluka AG); urea (CH_4N_2O, 99.4% Molar); trisodium citrate ($Na_3C_3H_5O(COO)_3$, 99.99% purity; Alfa-Aesar) as 0.5 $mmol \cdot L^{-1}$ aqueous solution.

During the assessment of the photocatalytic activity and the hydrogen production capacity, high purity oxalic acid (99.99 %, Spektrum 3D) was used as 5 and 50 $mmol \cdot L^{-1}$ solution, rhodamine B (99.9%, Reanal) was used as a 10 $\mu mol \cdot L^{-1}$ stock solution, methyl orange (99.9%, Alfa Aesar) was used as a 125 $\mu mol \cdot L^{-1}$ stock solution and ketoprofen (≥98%, Sigma-Aldrich) was used as a 100 $\mu mol \cdot L^{-1}$ stock solution.

4.2. Synthesis of the titania-based composites

4.2.1. With noble metal nanoparticles (binary composites)

As it is essential for every research procedure to have a preliminary study, binary composites were prepared. Gold and platinum nanoparticles were simultaneously deposited on the three different commercial titanias: Aldrich anatase, Aldrich rutile and Evonik Aeroxide P25. The synthesis strategies applied are presented below.

For the two noble metal nanoparticle and titania containing composites the following synthesis strategies were proposed: in situ reduction and impregnation [168]. In all cases the total noble metal content was 1 wt. % In the case of in situ reduction titanium dioxide (P25, AA or AR) was added before the synthesis of the noble metals, while in the case of impregnation titania was added after the synthesis of the Au and Pt. The schematic diagram of the two synthesis approaches is illustrated in **Figure 8.**

As already stated before, the composites consisted of 99 wt. % TiO_2 and 1 wt. % noble metals:

- 0.5 % Au and 0.5 % Pt
- 1 % Au and 0 % Pt – reference sample
- 0 % Au and 1 % Pt. – reference sample

When 0.5 % Au and 0.5 % Pt was targeted, three reduction approaches were used: two sequential and one simultaneous approach.

During the sequential method 53.5 mL distilled water was introduced in a beaker, then 7.75 mL trisodium citrate solution was added, followed by the addition of one of the noble metals' (1 mL gold or 1.07 mL platinum) precursor. After homogenization, 1.23 mL freshly prepared sodium borohydride solution (5 °C, in cold water) was added to reduce the noble metal precursor. In the next step the reaction mixture was further homogenized at room temperature to achieve the full decomposition of the remaining $NaBH_4$. After that the precursor of the other noble metal was added, it was followed by a second addition of $NaBH_4$ (also 1.23 mL) solution. The homogenization step was repeated once more and finally the suspension was purified by centrifugal washing using ultrapure Milli-Q water (3 × 15 min; 6000 rpm), then dried (12 h; 40 °C). The simultaneous reduction method was similar to the sequential one. The main difference was that the two noble metal precursors were added and reduced at the same time.

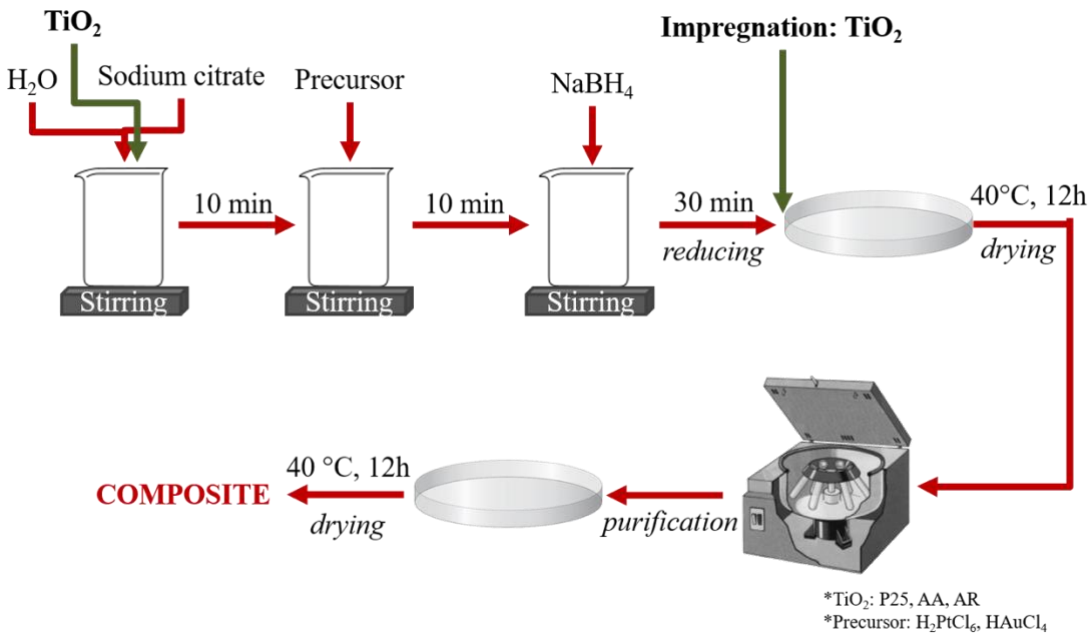

Figure 8. The synthesis and purification of TiO_2-Au and/or Pt nanocomposites by the means of chemical reduction using in situ and impregnation as possible pathways of the reaction.

The nomenclature of the samples was defined as follows: the abbreviation of the titania photocatalyst + ”_is” for the samples obtained by in situ reduction, or “_im” for the samples made with impregnation. This was completed with: “Au/Pt” when Au was reduced before Pt; “Pt/Au” when Pt was reduced before Au; or “Au&Pt” when both noble metals were obtained simultaneously. A relevant example is the case of ***AA_im_Au/Pt*** which was obtained from Aldrich anatase (AA), Au then Pt was reduced (Au/Pt) using the impregnation method (im). **Table 1.** summarizes the prepared composites.

Table 1. The as produced commercially available titania based and noble metal nanoparticle composites.

Base catalyst	**Synthesis strategy**							
	_im			_is				
P25	Au/Pt	Pt/Au	Au&Pt	Au/Pt	Pt/Au	Au&Pt	Au	Pt
AA	Au/Pt	Pt/Au	Au&Pt	Au/Pt	Pt/Au	Au&Pt	Au	Pt
AR	Au/Pt	Pt/Au	Au&Pt	Au/Pt	Pt/Au	Au&Pt	Au	Pt

4.2.2. With copper nanoparticles

During my studies I often got asked is it worth using the expensive noble metal nanoparticles? Isn't there a cheaper way to enhance the photocatalytic activity of titania? The answer is yes, so I completed a side study of the deposition of Cu nanoparticles on two of the previously used commercial titanias: P25 and AA. As for the synthesis, the same route was used as for the binary composites (presented in **Figure 8.**): in situ reduction was used and the copper nanoparticles were obtained from $CuCl_2$.

In order to investigate the effect of the Cu nanoparticles on the commercial titania, the mass content of copper was varied; therefore, five different samples were prepared for both base catalysts, with: 0.5%, 1%, 1.5%, 5%, and 10% copper. The nomenclature of the samples was hereby defined: the abbreviation of the base catalyst (P25 or AA) + the number of the percentage of the copper nanoparticles + Cu. For example: P25-0.5Cu is when P25 was the base catalyst and 0.5% Cu was reduced on it, or AA-1Cu is when AA was the base and 1% Cu was used.

4.2.3. With $NaYF_4$ and Au nanoparticles (ternary composites)

Considering the last part about the binary composites complete, the next intent was to further improve the photocatalytic activity of TiO_2 by preparing ternary composites. The other two components were Au nanoparticles and Yb^{3+}, Eb^{3+} and Tm^{3+} doped $NaYF_4$. The synthesis methods are presented below.

The **Yb^{3+}, Eb^{3+} and Tm^{3+} doped $NaYF_4$** samples were prepared by adding 1.488 mL $Y(NO_3)_3$ (0.5 M), 0.5 mL $Yb(NO_3)_3$ (0.5 M), 0.1 mL $Er(NO_3)_3$, 0.5 mL $Tm(NO_3)_3$ stock solutions to 15 mL of 0.5 mM trisodium-citrate. After stirring for 1 hour, 4 mmol of NaF and 20 mmol of urea were added and stirred again for 1 hour with a magnetic stirrer. The sample was then placed in a Teflon® lined autoclave for 12 hours at 180 °C. As the autoclave cooled to room temperature, the sample was separated and washed by centrifugation (5×5 minutes, 4400 rpm), 3 times with 40 mL ethanol and 2 times with 40 mL distilled water. Finally, the sample was dried for 12 hours at 40 °C in an oven.

The next step was the synthesis of **lanthanide doped $NaYF_4$-TiO_2 composites**. 0.05 g of the previously prepared $NaYF_4$ was dispersed in 42 mL of isopropanol and then 0.04 mL of diethylenetriamine (DETA) was added. After stirring for 10 minutes, 2 mL of 97% titanium isopropoxide was added. After mixing, the sample was hydrothermally treated for 24 hours at

200 °C in a Teflon® lined autoclave. The as-formed composite was separated and washed by centrifugation using 40 mL ethanol (3×5 minutes, 4400 rpm). Then it was dried in an oven at 40 °C for 12 hours [44]. In certain cases, calcination was carried out at 350 °C for 2 hours at a heating rate of 5 °C/min.

The TiO_2 reference sample was synthesized by carrying out the same steps, just without adding $NaYF_4$ to the system.

For the synthesis of **Au-containing composites** the same pathway was used as described in section 4.2.1. In all cases the in situ reduction was used and the Au content was 1 wt.%, which was based on the fact that in the literature the 1-2 % Au content proved to be the most beneficial to improve the photocatalytic activity [69]. During the synthesis only the reduction of Au took place, because it is not possible to reduce the Ti in TiO_2, because this process needs extremely high temperature and inert atmosphere [169].

The nomenclature of the samples was defined as follows: lanthanide-doped $NaYF_4$ was abbreviated as NYF. If the TiO_2 or the NYF-TiO_2 composite was calcinated it is marked with '_calc'. The order of the components indicates the order of the synthesis (for example: *NYF-TiO_2_calc* means that the NYF was synthesized firstly, then a composite was formed with TiO_2, then finally it was calcined). Consistently, if -Au appears at the end of a sample name that means that gold nanoparticles are present too. **Table 2.** summarizes the prepared composites.

Table 2. The as produced TiO_2, NYF and Au nanoparticle composites.

Base catalyst	**Not calcinated**		**Calcinated**	
TiO_2	no Au	Au	no Au	Au
NYF-TiO_2	no Au	Au	no Au	Au

4.3. Methods and instrumentation

The crystalline phase compositions and mean primary crystallite sizes of the photocatalysts were determined by **X-ray diffraction** (**XRD**) with a Rigaku diffractometer using Cu-Kα radiation (λ = 1.5406 Å) equipped with a graphite monochromator. The primary crystallite size of the prepared semiconductors was evaluated using the well-known Scherrer equation [170].

The morphological properties were investigated by **transmission electron microscopy (TEM)**. TEM micrographs were obtained using a FEI Tecnai G2 20 X-Twin HRTEM instrument to determine the composition of the samples. HRTEM micrographs were obtained

JEOL 2100 FEG S/TEM microscope equipped with a spherical aberration probe corrector and a GATAN Tridiem energy filter operating at 200 kV.

During the **scanning electron microscopy (SEM)** measurements a Hitachi S-4700 Type II FE-SEM was used to determine the average particle size and morphology of the samples. The applied acceleration voltage was 10.0 kV.

The **BET isotherm** was used to calculate the specific surface areas of the composite samples, for which a BELCAT-A device was used to record the isotherms at 77 K via N_2 adsorption.

In the case of **diffuse reflectance spectroscopy (DRS)** the light absorption properties of the solid samples were measured. The spectra of the samples (λ = 300-800 nm) were registered by using a JASCO-V650 spectrophotometer with an integration sphere (ILV-724). The indirect band gap of the photocatalysts was determined via the Kubelka-Munk method [171]. The (10) equation was used to calculate the band gap energies from the reflectance.

$$Tr\_KB = \sqrt{h\nu \frac{1-R}{2R}} \qquad (10)$$

UV-Vis measurements were performed using a JASCO-V650 spectrophotometer, using distilled water as reference.

HPLC measurements was performed on a Merck Hitachi device fitted with an L-4250 UV-VIS detector (Merck KGaA, Darmstadt, Germany) and a GROM Resin ZH 8 μm column.

GC measurements were carried out on a Hewlett Packard 5890 gas chromatograph fitted with a 5Å molecular sieve column and a thermal conductivity detector.

4.4. Evaluation of the photocatalytic activity

Photocatalytic activities of the composites were determined by the decomposition of rhodamine B solution under UV- (λ_{max}=365 nm), visible- (λ>400 nm) and near-infrared light (λ>850 nm) irradiation; or oxalic acid solution; or salicylic acid solution; or methyl orange solution; or ketoprofen solution under UV light. The reactor was surrounded either by 6 × 6 W black light lamps (9.53 W/m^2 energy flux at the reactor position) or 4 × 24 W conventional compact fluorescent lamps (Düwi 25920/R7S-24W; 81.37 W/m^2 energy flux at the reactor position) or 4 × 150 W NIR lamps (Philips IR RED R250 250 W; 52.25 W/m^2 energy flux at the reactor position). The energy fluxes were given by the lamp manufacturer. The three reactors used are presented in **Figure 9.**

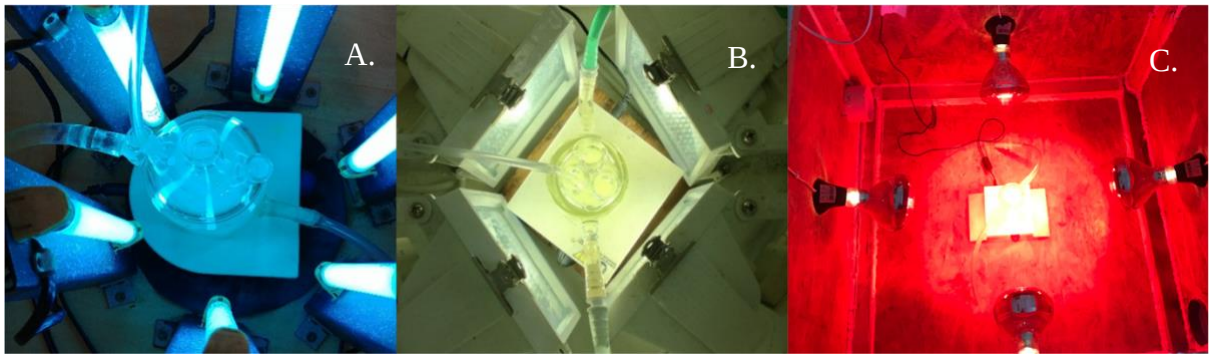

Figure 9. The used reactors for the determination of the photocatalytic activity (A-UV, B-visible, C-NIR).

A rhodamine B stock solution (10 μmol·L^{-1})/ oxalic acid stock solution (5mmol·L^{-1})/ salicylic acid solution (0.5 mmol·L^{-1})/methyl orange stock solution (125 μmol·L^{-1})/ ketoprofen stock solution (100 μmol·L^{-1}) and a 1 g·L^{-1} photocatalyst suspension were prepared, which was determined jointly by our research group before the start of my research and has been used in the measurements ever since. The reason for using these model pollutant lies in the fact that before starting my research, I always looked through the literature to find out which composite system was best suited for which model pollutant. The composites containing titanium dioxide and noble metal (Au, Pt) were promising in terms of oxalic acid decomposition, so I used this model contaminant as well. Further, when copper nanoparticles were deposited on titanium dioxide, oxalic acid was no longer applicable because copper could no longer resist the reducing effect of oxalic acid, so I decided to study dyes. However, when the decomposition experiments were not successful, I wondered to what extent these composites decompose a real contaminant as well, so I also tried the decomposition of ketoprofen. In the last stage of my research, when I investigated the photocatalytic activity of tertiary composites (NYF, TiO_2, Au), based on the data in the literature, these composites were the most suitable for decomposing dyes. This is how I decided to break down rhodamine B.

After the preparation of the suspensions an ultrasonic bath was used to distribute the catalyst more efficiently, then the system was stirred for 15 minutes in dark for adsorption to occur, after that the photocatalytic degradation reaction was initiated by turning on the lamp (either UV-, visible- or NIR light-emitting, with the above-mentioned wavelengths). The rate of adsorption was negligible after the 15 minute adsorption time (approximately 1-2% was adsorbed on the catalyst surface) and is therefore not included in the calculation. During the experiments continuous magnetic stirring and thermostating at 20 C° was applied. In the case of the NIR tests the water was supplemented for each 2 h (except night), while the experiment

length was 24 h. 2 mL of the samples were taken every 10 min (1 h for NIR) in the first hour (6 h NIR and one sample 2 h later and the last sample before finishing the experiment) of the experiment and every 20 min in the second hour. After the centrifugation (3 min, 13,800 rpm) and filtration (with a Whatman Anotop 25 0.02 µm syringe filter) of the samples, the rhodamine B/oxalic acid/salicylic acid/methyl orange/ketoprofen concentrations were measured by HPLC or UV-Vis spectroscopy.

In all the cases the conversion was calculated with the (9) equation. Hereinafter the words conversion, yield and efficiency will be used as synonyms.

$$Degradation\ (\%) = \frac{Concentration\ of\ the\ pollutant\ at\ the\ given\ time}{Concentration\ of\ the\ stock\ solution} \times 100 \qquad (9)$$

4.4.1. H_2 production

For the H_2 production measurements the freshly prepared, washed catalyst was dispersed in 50 mmol·L^{-1} oxalic acid solution and poured into a glass reactor (total volume: 150 mL), and it was irradiated with 10 × 15 W UV fluorescent lamps (λ_{max} =365 nm, LightTech Kft., Budapest, Hungary), as presented in **Figure 10.** The well homogenized suspension (catalyst = 1 g·L^{-1}) was purged with N_2 (99.995 %, Messer Kft., Budapest, Hungary) at a flow rate of 50 mL·min^{-1} to ensure O_2-free conditions. The reactor was connected through a PTFE tube to a gas chromatograph. Samples were taken from the gas flow with a 2 mL sampling valve, every 10 min in the first hour of the experiment and every 20 min in the second hour. The rate of H_2 evolution was calculated using the calibration (carried out with certified 5:95 H_2:N_2 gas) and the applied N_2 flow rate.

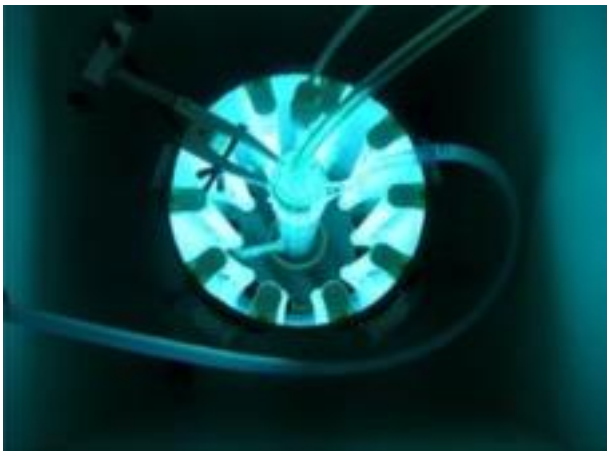

Figure 10. The used reactors for the determination of the photocatalytic hydrogen production.

5. Results and discussion

5.1. Composites consisting of TiO_2 and noble metals

After the preparation of the binary composites, it was needed to investigate their morphological and structural properties with different characterization methods. Based on the results of the photocatalytic activity and hydrogen production the composition of some of the composites was changed. For more details it is worth to read on the following chapters.

5.1.1. Characterization

As a first step of characterization process, the crystallite mean size and phase composition was evaluated using **X-ray diffraction**. The semiconductors composition remained unchanged during/after the deposition of noble metal nanoparticles, as follows: Aldrich anatase (AA) contained only anatase crystal phase (≈80-100 nm), Aldrich rutile (AR) contained mainly rutile phase with larger particles (≈300 nm) and a small amount of anatase (≤4 wt.%) as well, while Evonik Aeroxide P25 (P25) contained anatase and rutile (89 wt.%, ≈25 nm *vs.* 11 wt.%, ≈40 nm, **Figure 11.**). It must be mentioned that the noble metal nanoparticles were not detectible, as their concentration was lower than the detection limit of the instrumentation and some of the most intensive diffraction peaks (e.g. for at 38º (2θº) for Au) were covered by the triplet signal of anatase in the same region.

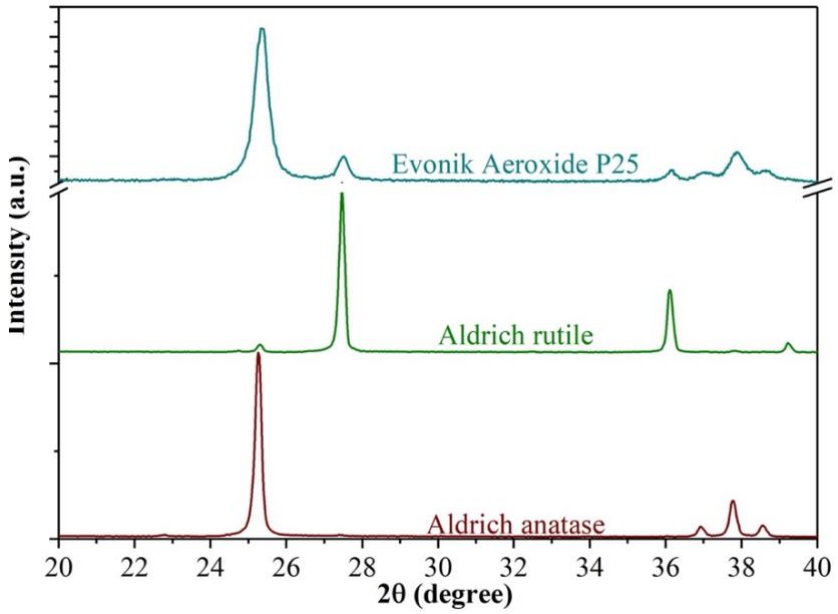

Figure 11. XRD patterns of different commercial TiO_2 photocatalysts used as base photocatalysts in the synthesis of titania/noble metal(s) nanocomposites.

The next crucial parameter determining the photocatalytic activity, was the light-absorption properties of the composites. In first instance, in the **DRS** spectra of the composites (**Figure 12.**) the reflectance values in visible light region were higher for unmodified commercial catalysts than for the composites (while the color of the commercial materials were white, the composites' color varied from grey to purple, giving reflectance values between ≈40-60 % at visible light wavelengths).

As it could be observed, the deposition of noble metal nanoparticles induced significant changes in the optical properties of some commercial titania-based photocatalysts, which were quantified by calculating the band gap energies using the Kubelka-Munk equation [171]. In **Table 3.** it can be observed that all composites have smaller band gap energies compared to their base catalyst.

Table 3. Band gap energy values (eV) obtained from the DRS measurements, showing the effect of the noble metal nanoparticles on the optical properties of titania.

Sample	**P25**		**AA**		**AR**	
	in situ	**impr.**	**in situ**	**impr.**	**in situ**	**impr.**
Au/Pt	2.57	2.50	3.13	3.19	2.92	2.86
Pt/Au	2.56	2.67	3.14	3.19	2.84	2.89
Au&Pt	2.58	2.51	3.16	3.17	2.89	2.90
Au	2.47	-	3.17	-	2.88	-
Pt	2.75	-	3.15	-	2.82	-
Base catalyst	3.04		3.24		2.99	

In the case of Aldrich anatase and rutile, the decrease was less (3.24 eV for AA, 3.13 - 3.19 eV for AA-based composites – **Figure 12A., 12D.** - while 2.99 for AR and 2.82 - 2.92 eV for AR-based composites, **Figure 12B., 12D.**) than that of P25-based catalysts (**Figure 12C., 12D.**), where the band gap values decreased with ≈ 0.30 - 0.57 eV (from 3.04 eV to 2.47-2.75 eV). This difference can originate from the fact that the particles that build up the base catalysts are significantly smaller in the case of P25 than for AA and AR, and the differences were more accentuated for these particles than for larger particles of the catalysts [54], due to the ratio between the noble metal and semiconductor nanoparticles.

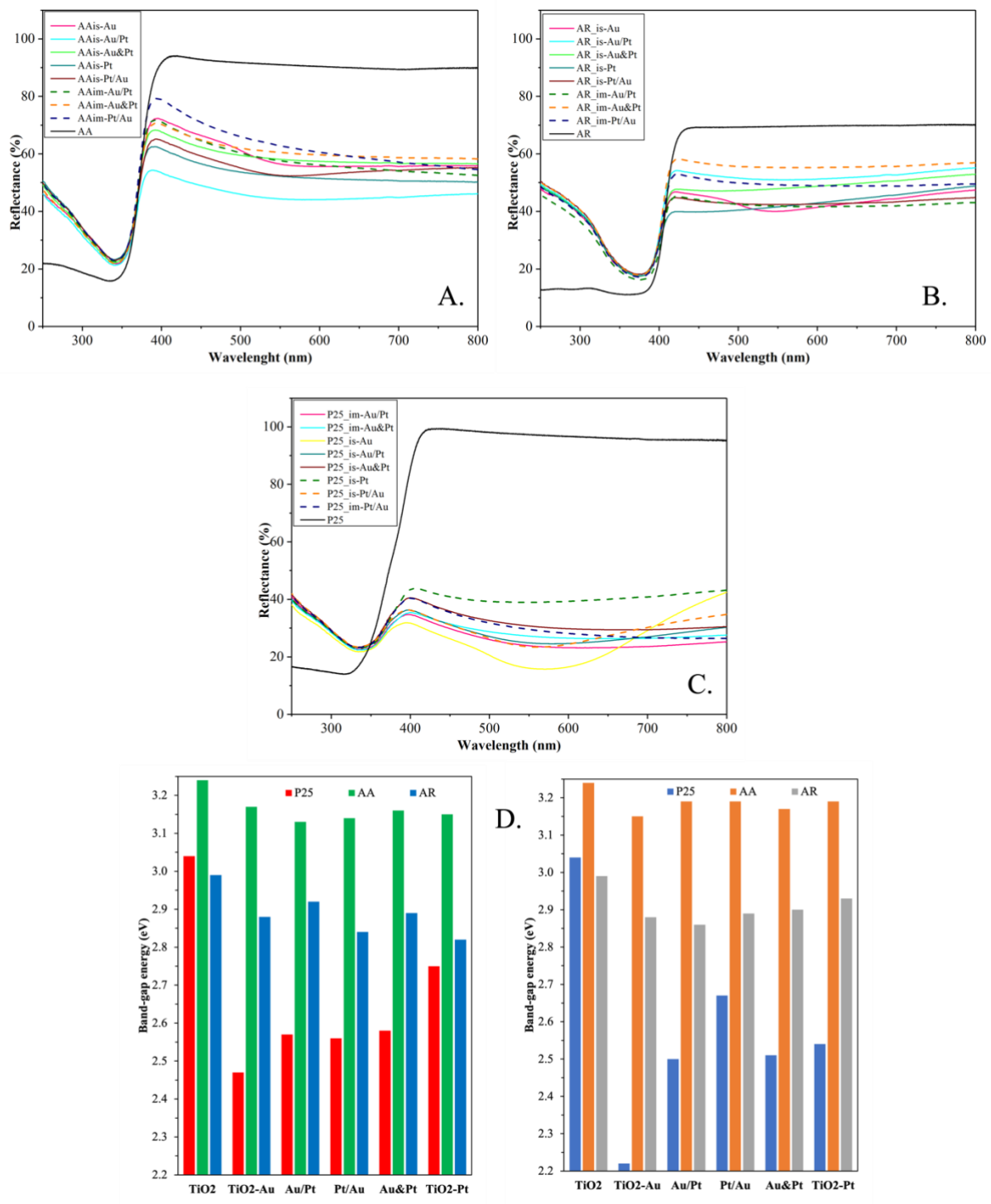

Figure 12. The influence of the noble metals on the optical properties of three commercial titanias (A.-AA, B.-AR, C.-P25, D.-band gap energy comparison using the in situ sample series-right and impregnation series-left). The influence was significant when P25 was considered as the base photocatalyst, while in the other cases no changes were observed in their spectra.

Analyzing the plasmonic bands of the Au-based and the binary composites (**Figure 12.**) it can be observed that the characteristic plasmonic bands of Au nanoparticles have disappeared when the reduction of Au and Pt was performed simultaneously using both synthesis pathways, i.e., impregnation and in situ. This spectral alteration could have two explanations:

- the Pt "covers" the Au nanoparticles, forming a so-called core-shell nanostructure [172];
- the two noble metals are forming alloys in these binary composites.

When the reduction of the metals was carried out separately, using the in situ method, the plasmonic bands of the Au remained observable at ≈550 nm, driving us to the conclusion, that in this case, the nanoparticles were deposited separately onto the surface of the catalysts, while using the impregnation method we can observe that the plasmonic band of the Au disappears, offering a similar explanation for this phenomenon as that given for the same-time reduction method. In the third case, when the Au was reduced after Pt (Pt/Au), no plasmonic bands were observable. This phenomenon can be explained only by the formation of alloys, because, in this case, the formation of Pt-Au core-shell particles should have plasmonic bands (Pt being in the core and Au the shell of the nanostructure). Using in situ reduction one can see the predicted results for AA and P25-based composites (**Figure 12A-C.**), with visible plasmonic bands, showing the possible appearance of core-shell nanoparticles or the particles that are deposited separately on the surface of the catalyst. Furthermore, it can be also seen (**Figure 12D.**) that the band gap energy values of the composites that contain two noble metals were between the values of the two reference samples TiO_2-Au and TiO_2-Pt (in each case), suggesting the simultaneous presence of both noble metals. As it was detailed above, different composite build-up scenarios were possible in the case of all binary composites, that is why the visualization of the particles was mandatory using electron microscopy techniques.

To elucidate the (partial) discrepancies from DRS, **HRTEM** and **EDS** measurements were involved in morphological and structural investigations. In **Figure 13.** it is now clearly visible that noble metal nanoparticles were obtained in both synthesis procedures (in situ and impregnation). The smallest (2-4 nm) nanoparticles were found when both precursors were reduced simultaneously (samples TiO_2-Au&Pt). In this case, a high number of noble metal clusters were also detected. However, the question concerning the relationship between gold and platinum is still open. That is why STEM-HAADF, HRTEM and EDS spectra were simultaneously investigated (**Figure 14.**) to reveal the nature of the nanoparticles. It was found that the individual nanoparticles were of Au (studying the lattice fringes), while in

case of twin and larger noble metal nanoparticles the signature of Pt (using EDS) was also detected. This points out that Pt is present in any case in the form of very small nanoclusters. This result excluded the presence of core-shell nanoparticles as well. Also, a size distribution of the noble metal nanoparticles was carried out (**Figure 15.**) to verify if the first size estimations were correct. The results supported our statement that the obtained size of Au or Pt was between 1 and 5 nm, with a dominance of 3.5 nm particles. This gained information was crucial for the explanation of the photoactivity (presented later), knowing that the activity depends on several structural and morphological characteristics, too.

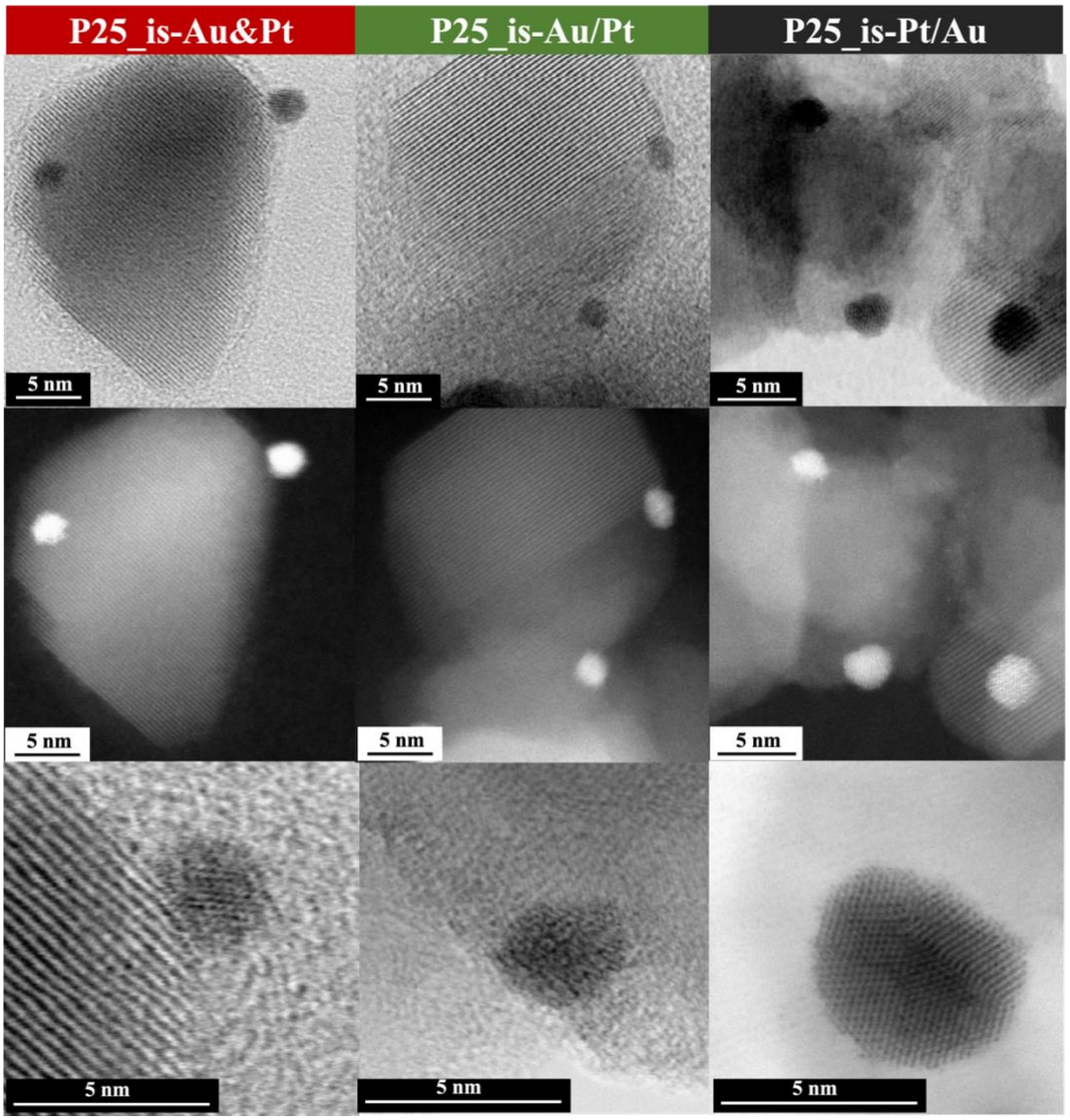

Figure 13. HR-TEM and STEM-HAADF micrographs of P25_is series, showing 2-4 nm sized Au and or Pt nanoparticles.

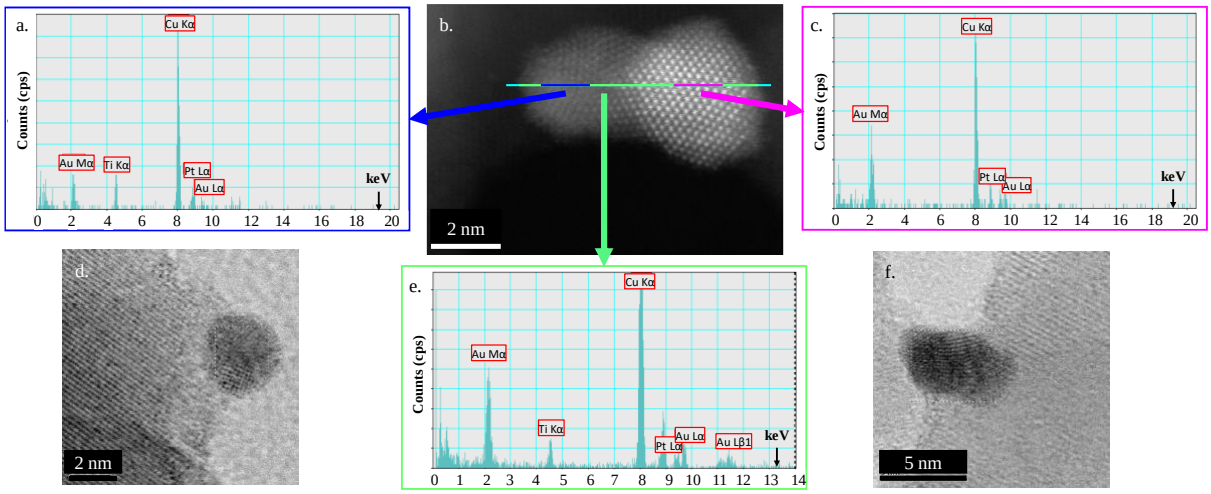

Figure 14. STEM-HAADF (b) micrograph, HR-TEM (d, f) images and EDS spectra (a,c and e) of P25_im-Au/Pt sample, showing the presence of both Au and Pt. No core shell particles and no alloys were detected, just nanoparticles, which show Pt and/or Au presence.

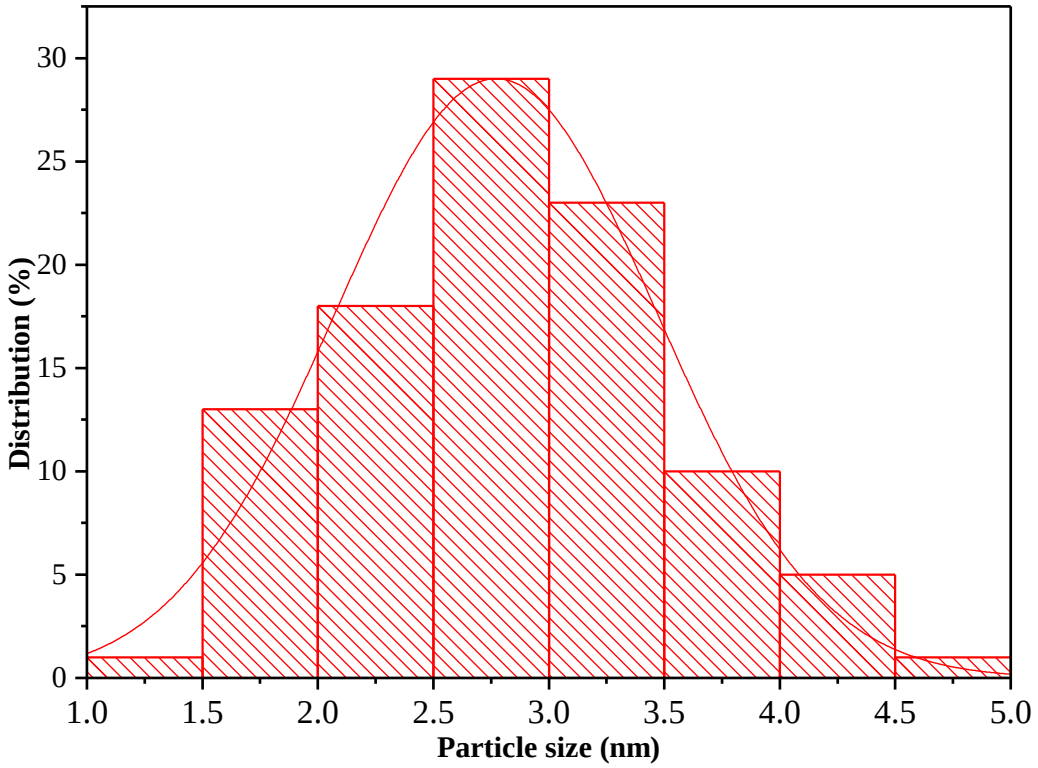

Figure 15. Noble metal nanoparticle size distribution of sample P25_is-Au/Pt, counting 100 nanoparticles. The distribution was nearly the same for all the materials.

5.1.2. Photocatalytic activity

The photocatalytic degradation of oxalic acid (the chosen model pollutant) was followed for one hour using HPLC. By looking at the photodegradation data, the first impression was that the degradation of oxalic acid depends on the synthesis pathway, type of commercial TiO_2 and the used co-catalyst nanoparticles (**Figure 16.**).

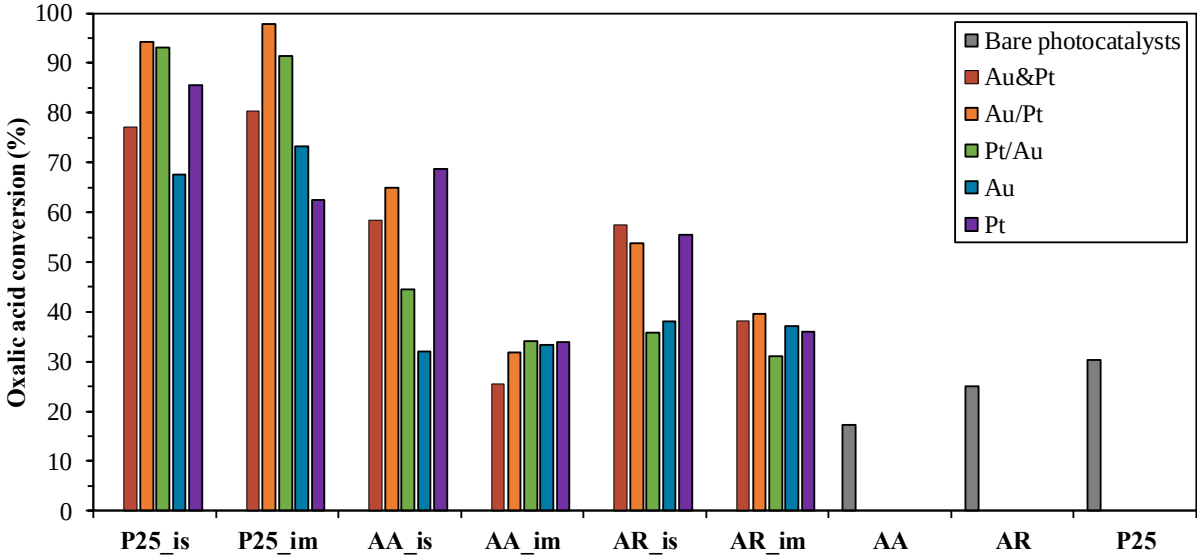

Figure 16. The oxalic acid degradation performances after 1 h of the obtained nanocomposites under UV light. All the composites showed higher photocatalytic activity then their corresponding base photocatalyst. The photocatalytic performances after two hours were omitted at each composite degraded totally the oxalic acid.

In general, it can be observed, that the P25-based composites showed the highest photocatalytic efficiencies, degrading more than 75% of the model pollutant. The highest degradation values (≈95%) were obtained for both binary composite synthesis pathways, where Pt was deposited after Au (*P25_is_Au/Pt* and *P25_im_Au/Pt*). Regarding the of AA-based composite series the highest decomposition (69 %) was obtained with the monometallic Pt containing composite (*AA_is_Pt*), prepared by in situ reduction, which was followed closely by the bimetallic composite (Au and Pt - *AA_is_Au/Pt*), having a degradation efficiency of ≈ 65 % while the composites made by impregnation showed a lower yield, between 32-35%. The AR-based catalysts showed interesting results as in case of these materials the highest performing one was *AR_is_Au&Pt* (58%) followed by *AR_is_Au/Pt* (54%). It should be mentioned that the reference photocatalyst *AR_is_Pt* showed a 56% of oxalic acid degradation. All samples from the AR series which were obtained by impregnation showed lower photocatalytic activity compared to their in situ counterparts (30-40% oxalic acid removal).

Comparing the yields, we can conclude that, the presence of noble metal nanoparticles increased the efficiency of the catalyst. By comparing the performances of the nanocomposites obtained by different synthesis pathways some tendencies can be noticed. Thus, the Aldrich-titania-based composites have lower efficiencies when the impregnation method was used (yields in the 25-34% range for AA impregnation and in the 32-69% range for in situ, and in the 31-41% range for AR impregnation and in the 35-58% range for in situ). For P25-based catalysts this tendency is inverted, as the materials prepared with impregnation have slightly higher conversion in two cases comparing to those with in situ method.

On the other hand, the efficiency values obtained for P25-based composites were higher, while the efficiencies obtained in the case of AA-based composites were not so low, compared to the relatively small surface area of the base catalyst [54]. This behavior can be explained by the relatively large number of available charges on the surface of the catalyst normalizing to their specific surface area.

Among the reference photocatalyst, in the case of platinum in situ samples were more efficient than the impregnated ones, while in case of Au containing reference materials near the same efficiencies were observed, except in case of P25 where the impregnated version was the better one (**Figure 16.**).

5.1.3. Photocatalytic hydrogen production

As already shown in the previous section, the synthesis pathway, the deposition sequence of the noble metals and the structural differences of the base catalysts are crucial parameters for the photocatalytic activity, influencing differently the commercial titanias. Consequently, it was expected that a similar effect will show up in the case of photocatalytic hydrogen production, where also oxalic acid was used as the sacrificial agent.

In general, as it was slightly predictable, P25-based composites gave the highest H_2 production rates. As it can be seen in **Figure 17.** the best performing composite came also from this series, as the *P25_im_Pt/Au* had the highest H_2 production rate, namely 1567 µmol of H_2 during the whole experiment (2 hours). It is interesting to observe, that the *P25_is_Au&Pt / P25_is_Au/Pt* and *P25_im_Au&Pt / P25_im_Au/Pt* composite pairs have relatively small difference in their H_2 production efficiencies (1429 µmol vs. 1417 µmol / 1289 µmol vs. 1221 µmol), although their build-up was quite different, as it was shown in the previous sections. In the case of the reference samples, the Pt based ones were the ones with the highest efficiency (1126 µmol of H_2 – P25_im_Pt). While in case of both noble metals the reference samples

which were obtained by impregnation were slightly more efficient (P25_im_Pt - 1126 µmol vs 986 µmol - P25_is_Pt; P25_im_Au - 750 µmol vs 657 µmol - P25_is_Au).

About the Aldrich-based composites, it can be summarized that their photocatalytic efficiency was generally lower than that of P25-based composites. The hydrogen production rates showed significantly different values for the materials obtained using different composite synthesis pathways: the in situ preparation method generally resulted in higher efficiencies than those obtained by the impregnation method, including for all the reference samples, while this difference was not so accentuated for the P25-based composites. On the other hand, it can be also observed, that the noble-metal deposition sequence has a much stronger influence on the activity of the anatase-based composites in comparison with those achieved for the samples synthesized by using Aldrich rutile, where the performances were decreased with 44-85% comparing the results obtained by impregnation to their in situ analogues. The differences between rutile-based composites were smaller, but generally, the in situ preparation pathway resulted in higher yields (with 5-53%) comparing to their analogues prepared with impregnation.

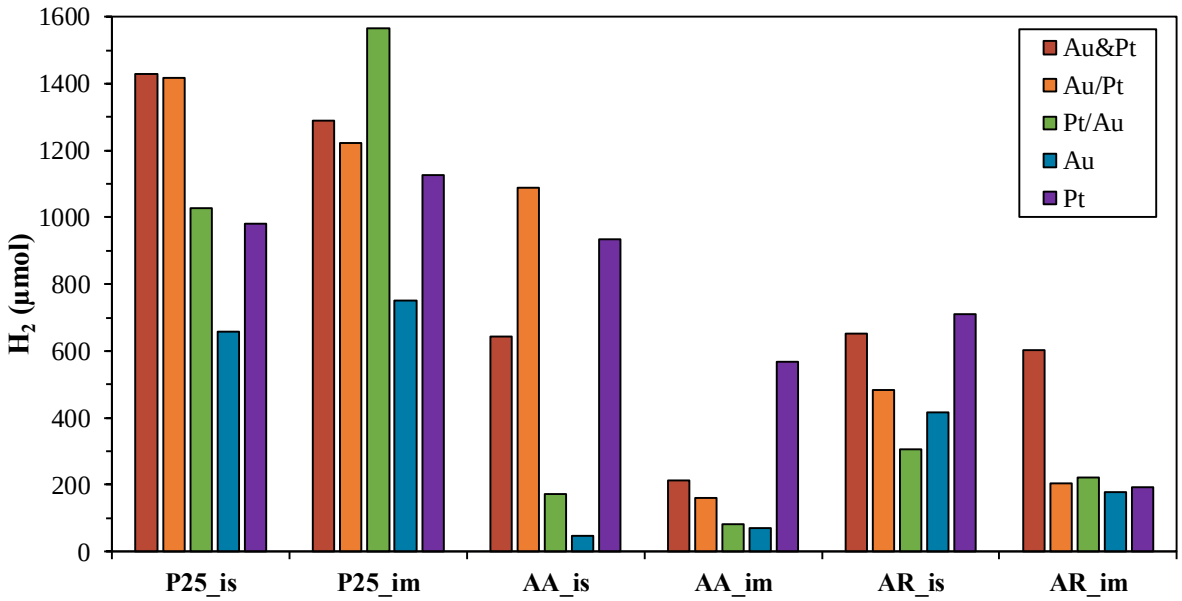

Figure 17. The photocatalytic H_2 production capacities of the used nanocomposites. The bare photocatalyst were not shown, as they do not produce hydrogen under these experimental conditions.

As it can be seen these materials are rather active under UV light in the degradation of oxalic acid and are efficient in the photocatalytic hydrogen generation process. However, this high activity can turn into a severe drawback if these materials would spread out in our

surroundings. One can imagine the situation if such powders could escape into natural waters and would accumulate in static waters, such as lakes. Therefore, **dynamic light scattering (DLS)** measurement were carried out to study the agglomeration of these materials.

As it can be observed in **Figure 18.** the DLS measurements were performed on the materials prepared with most efficient reduction method, which was in most cases Au/Pt composites and their bare counterparts.

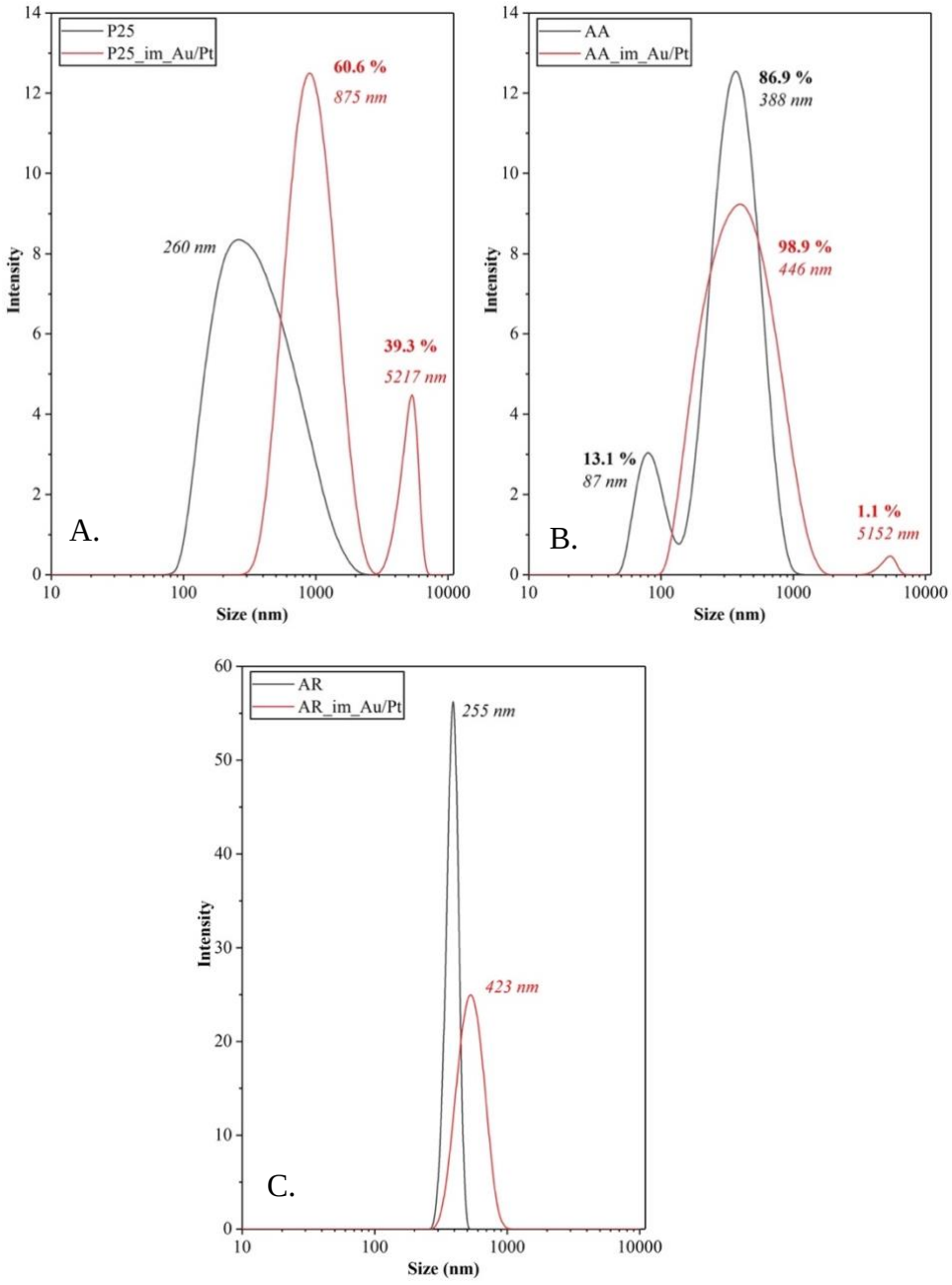

Figure 18. DLS measurements of the composites prepared with most efficient reduction method, which was in most cases Au/Pt composites and their bare counterparts (A-P25, B-AA, C-AR).

AA was the most hydrophilic one showing a bimodal distribution of the particles. The first peak even shows that pure AA can be found also as individual crystals in the suspension, as the obtained peak value corresponds with the size which can be estimated by other techniques (≈80 nm). The second peak was the dominant one suggesting a slight agglomeration of the particles (≈380 nm). Both peaks shifted significantly to higher values (446 nm and 5152 nm) showing that the addition of noble metals (sample AA_im_Au/Pt) increases the agglomeration grade of the semiconductor particles. The same trend was observed for AR as well (peak shifting from 255 to 423 nm as noble metals were deposited – AR_im_Au/Pt), the only difference was that only one peak was observed. The trend continued in the case of P25, but the bimodal spectrum reappeared only in the case of the noble metal deposition - – P25_im_Au/Pt, while the bare P25 showed only one broad peak at 260 nm. The shifting after Au/Pt addition was also observable, while the previously mentioned peaks appeared at 875 nm and 5217 nm. The results clearly show that by the deposition of noble metals the titania nanoparticles suffer intense aggregation which was visible with the eye as well. This kind of behavior may result in a fast sedimentation of the noble metal modified particles under real conditions. It should be also mentioned that the results were supported by the zeta potential measurements as well.

When pure AA, AR and P25 were applied, 5120, 4980 and 3250 was obtained for the IEI number. As noble metals were deposited on their surface in the im_Au/Pt configuration, these number changed to 180, 575 and 7820. This clearly shows that for high particle size titanias (AA and AR) the phenolic intermediates generation is low when noble metals are deposited on its surface, meaning that instead of OH radicals surface oxidation by holes plays a crucial role in the oxalic acid degradation, while in case of P25 an enhanced charge separation was promoted and therefore the generation of higher amount of OH radicals/appropriate intermediates were observed.

5.1.4. Changing the ratio between the two noble metals

After the characterization and testing the photocatalytic activity of the composites the oxalic acid degradation and hydrogen production were compared. The samples that most efficiently (100% conversion and maximum reaction rate) decomposed oxalic acid or samples that produced the most hydrogen were selected. From each series of photocatalysts - made with the best in situ and impregnation - the composition of the composites was changed. Titanium dioxide was kept unaltered at 99 wt.%, and the weight ratio of the precious metals was changed

to 0.25% - 0.75% and 0.75% - 0.25%, respectively. After changing the proportions, the new composites were prepared using the synthesis method mentioned in section 4.2.1. The nomenclature remained as used before, just supplemented with the number 25 or 75 in front of Au or Pt, which state the relative ratio of the noble metals. **Table 4.** summarizes the prepared composites.

Table 4. The as produced composites of commercially available titanias and Au and Pt with the changed ratio.

Base catalyst	**Synthesis strategy**			
	_im		_is	
	Au&Pt		Au/Pt	
P25	0.25 Au	0.75 Au	0.25 Au	0.75 Au
	0.75 Pt	0.25 Pt	0.75 Pt	0.25 Pt
	Au&Pt		Au/Pt	
AA	0.25 Au	0.75 Au	0.25 Au	0.75 Au
	0.75 Pt	0.25 Pt	0.75 Pt	0.25 Pt
	Au&Pt		Au&Pt	
AR	0.25 Au	0.75 Au	0.25 Au	0.75 Au
	0.75 Pt	0.25 Pt	0.75 Pt	0.25 Pt

In the first round the **photodegradation of oxalic acid** was tested. From the P25 based composites the ones made by using in situ reduction the best performing was the sample where the Au was reduced before Pt (P25_is-Au/Pt). In this case the noble metal ratio change did not increase the activity. After an hour the best efficiency belonged to the composite containing 0.5% Au and 0.5% Pt (≈95 %). The second-best catalyst was the composite with 0.25% Pt and 0.75% Au (≈84%) With the impregnation method the ratio between Au and Pt was changed when the Pt was reduced first, then Au (P25_im-Pt/Au). The best result was achieved by the composite with 0.25% Pt and 0.75% Au (after an hour ≈92 %).

For the composites containing AA, using the in situ method, the best result with ≈65 % was shown by the sample in which Au and then Pt was reduced (AA_is-Au/Pt). After the noble metal ratio change, the best efficiency was observed with the Pt content reference catalyst and the composites with 0.5-0.5% noble metals achieving ≈65-70% conversion. After the change of the ratio between the noble metals the one containing 0.25% Au and 0.75% Pt proved to be the next in the line with a conversion of ≈53%. Among the impregnated samples, the noble

metal content change was made when both noble metals were reduced at the same time (AA_im-Au&Pt). The concentration change did not improve in this case neither, while the composite containing 0.5-0.5% noble metal sustained the best efficiency with a ≈60% conversion. By changing the ratio also the composite containing 0.25% Au and 0.75% Pt had the best activity after the 0.5-0.5% catalyst (≈35%).

For AR-based composites, the best results were achieved for both of the preparation method (impregnation and in situ) when gold and platinum were simultaneously reduced (Au&Pt). Following the change in concentration, in both cases the best efficiencies were shown in the samples containing 0.25% Pt and 0.75% Au. The conversion rates were the following: 85% with in situ (AR_is-75Au&25Pt) and 90% with impregnation (AR_im-75Au&25Pt).

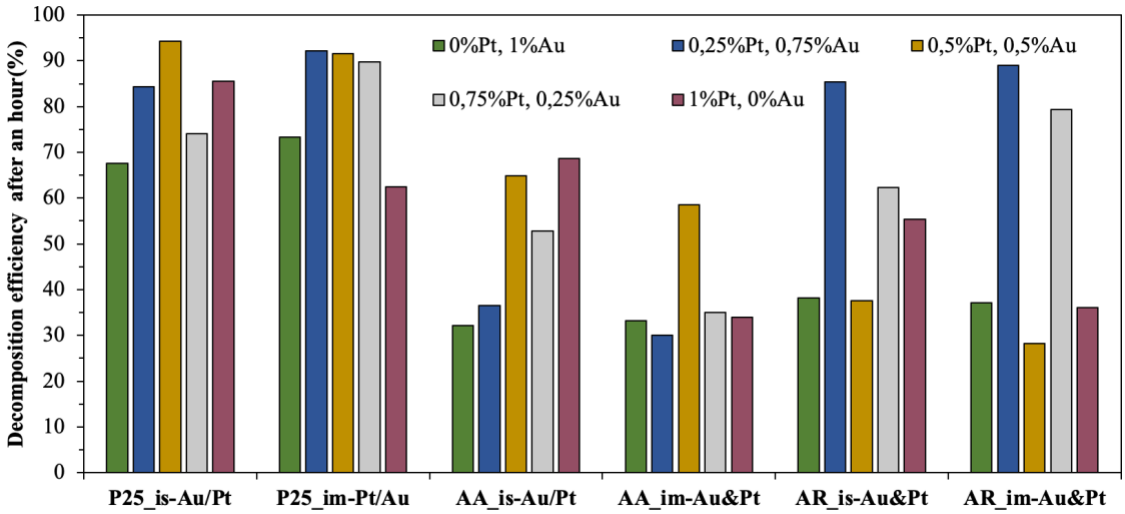

Figure 19. The oxalic acid degradation performances after 1 h of the obtained nanocomposites under UV light. Only in the case of the AR based composites improved the photocatalytic activity the change in the composition.

Overall, considering the two reduction methods the following conclusions can be drawn:

- in situ method: for the P25 and AA based composites the best photocatalytic activity was achieved when the sequential reduction was used - first Au then Pt (Au/Pt). For the AR based composites the simultaneous reduction of the noble metals proved to be the best (Au&Pt).
- impregnation: for the P25 based composites the sequential reduction was the best as well as for the other method (first Pt then Au – Pt/Au). For the AR and AA based catalysts the simultaneous reduction of the nanoparticles proved to be the best according to oxalic acid degradation (Au&Pt).

- regarding the order of the reduction of the two noble metals:
    - first is Au then Pt (Au/Pt): when the base catalyst was AA or P25, using in situ reduction in both cases (AA_is-Au/Pt, P25_is-Au/Pt);
    - first Pt then Au (Pt/Au): when the base catalyst was the P25, using impregnation method (P25_im-Pt/Au);
    - Au and Pt at the same time (Au&Pt): the AR based composites (in situ and impregnation as well - (AR_is-Au&Pt, (AR_im-Au&Pt) and AA based ones, using impregnation (AA_im-Au&Pt).
- the ratio between the noble metals: The photocatalytic activity was improved only in the case of the AR based composites for both synthesis strategies after the change in the composition. For the P25 based composites the change in the composition improved the photocatalytic activity for the catalyst made with impregnation. The photocatalytic activity of the AA based composites was not enhanced by the composition change.

Considering the degradation of carboxylic acids, such as oxalic acid, both gold and platinum nanoparticles deposited on the surface of a titania are good photocatalysts: this is demonstrated by the experiments also, which can be seen in **Figures 19.** and **20.** Overall, it is well known that the synergistic effect between Au and Pt results a significant enhancement in the photocatalytic activity [173]. The presence of both noble metals can result different outcomes: they can be located separately, they can form core-shell structure or alloys [174]. If one nanoparticle is located on the other the electron transfer path is longer, therefore more holes are available for oxidation. This is why the binary composites have better photocatalytic activity.

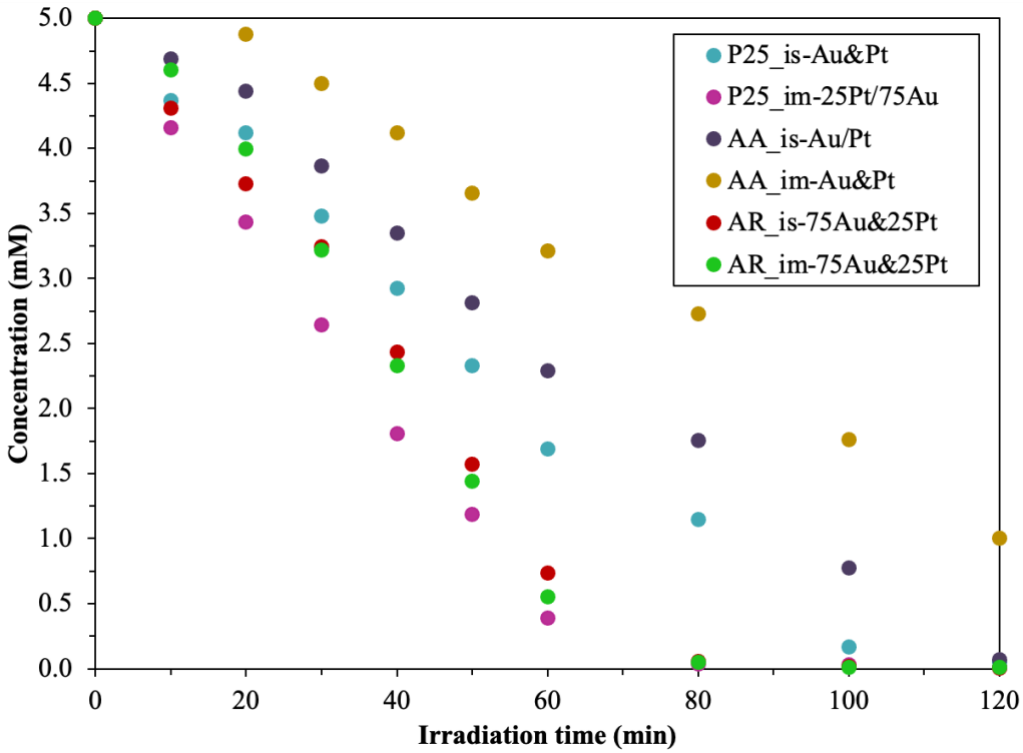

Figure 20. Degradation curves for oxalic acid – those composites are marked which had the best activity for each base catalyst (P25, AA, AR).

Salicylic acid degradation experiments were performed on the composites that demonstrated the best photocatalytic activity on oxalic acid, this is also illustrated in **Figure 16.** For each of the base photocatalysts one in situ and one impregnation-made composite was chosen for salicylic acid photodegradation, this is presented in **Figure 21.**

The binary composites containing P25, Au and Pt (P25_is-Au/Pt – 48%, P25_im-Pt/Au – 36%) did not show better photocatalytic activity than the bare P25 (66.6%). The composite obtained using in situ reduction showed better activity in the first hour, but in the second hour the activity sequence changed. P25 reached 66.6% conversion at the end of the second hour, while the sample named P25_is-Au/Pt decomposed 48% of the salicylic acid. The P25_im-Pt/Au composite showed even lower conversion, only 36% had been degraded from the salicylic acid.

In the second case both (in situ and impregnated) composites achieved better photocatalytic activity than bare AA. The AA_is-Au/Pt composite decomposed the salicylic acid by 93% at the end of the two-hour experiment and less than 0.05 mM of salicylic acid remained in the system. The AA_im-Au&Pt catalyst also achieved relatively high efficiency, and degraded 81% of salicylic acid, while bare AA, reached 40% conversion.

AR itself showed better activity on salicylic acid than its composites with gold and platinum. At the same time, the composite made with in situ reduction (AR_is25Au&75Pt) showed better photocatalytic activity than the impregnated (AR_im-25Pt&75Au) one. The AR_im-25Pt&75Au sample proved to be almost inactive, as only 14% of salicylic acid was decomposed. The efficiency of bare AR was 66%, which was approached by the AR_is25Au&75Pt composite with a conversion value of 45%.

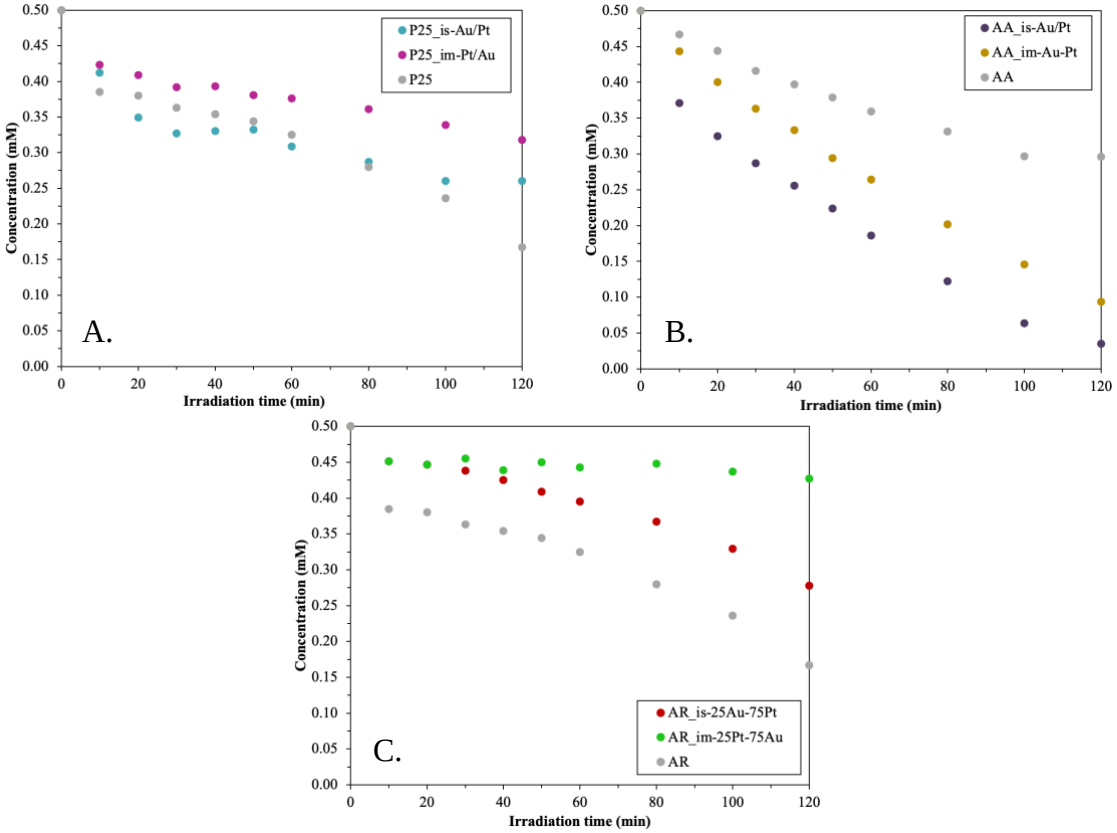

Figure 21. Degradation curves of salicylic acid (A - P25 and its composites, B - AA and its composites, C - AR and its composites) – the AA based composites achieved higher activity than the base catalyst.

Figure 22. illustrates the comparison of the degradation of oxalic acid and salicylic acid of the samples. A general observation is that for the P25 and AR based catalysts the degradation of oxalic acid was much higher than the degradation of salicylic acid. There is only one exception, namely sample AA_im-Au&Pt, where the photocatalytic activity (after an hour) was higher for salicylic acid (47.2 %) then for oxalic acid (25.4 %). The AA based photocatalyst made with in situ method had almost the same decomposition efficiency for salicylic acid and oxalic acid with the values of 62.8 % and 64.8 %.

As detailed in section 5.1.4.1. the presence of the noble metals is essential. During the degradation of salicylic acid surface complexes are generated, so the absorption has a big role

here [175]. This process takes place most easily on the surface of anatase titanias. This is where the explanation lies why only for the AA based composites achieved better activity then the base catalyst: the anatase phase plus the high specific surface area [39] of the AA.

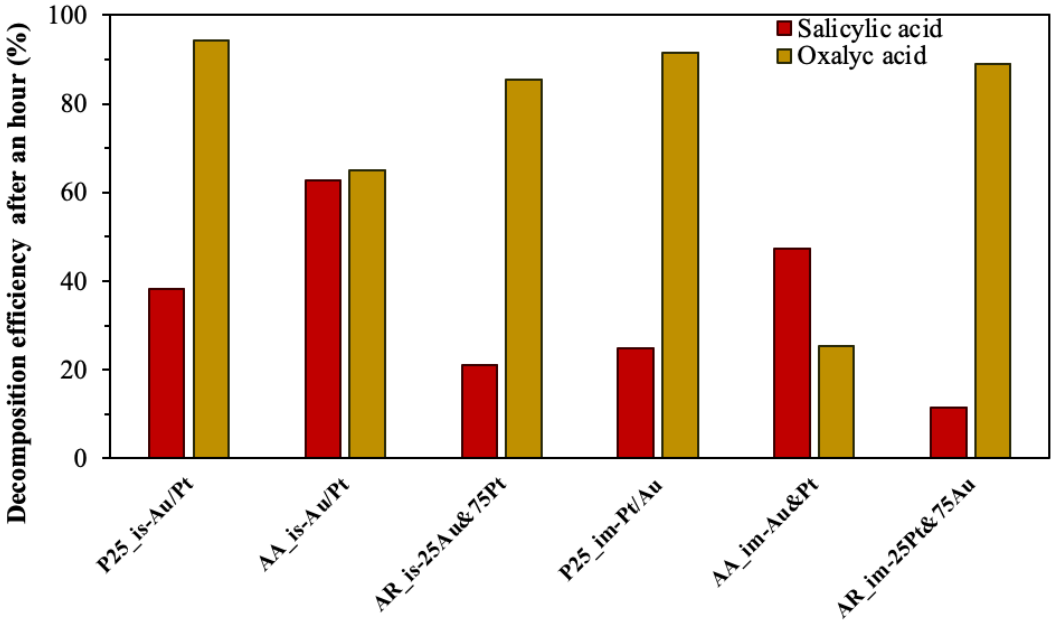

Figure 22. Comparison of the degradation of oxalic acid and salicylic acid of the samples – generally the P25 and AR based composites had higher activity for oxalic acid degradation than for salicylic acid.

After the investigation of the photodegradations **hydrogen production capacity** was examined. **Figure 23.** presents the obtained volume of H_2 during the experiments, expressed in mL. In the case of P25 based catalysts after the changed concentration of the noble metals, the highest amount of hydrogen, 1800 µmol, was produced by the composite named P25_is-75Au/25Pt. For the impregnated composites (P25_im-Pt/Au), the change in concentration did not increase the hydrogen production ability. The best sample remained which contained 0.5% Au and 0.5% Pt (P25_im-Pt/Au), producing 1600 µmol of hydrogen.

The best AA-based photocatalysts was the in situ made AA_is-Au/Pt, which produced 1100 µmol of hydrogen. Using the impregnation method, the reference catalyst containing only Pt (AA_im-Pt) produced, 576 µmol H_2, after this AA_im-Au&Pt, with the 200 µmol of H_2 production proved to be the (second)best.

Neither did show a beneficial effect the change of Au:Pt ratio in the case of AR based composites. Using both reduction methods, that composite proved to be the best when the gold was reduced simultaneously with platinum at 0.5 to 0.5%. With in situ reduction (AR_is-Au&Pt) 650 µmol, with impregnation (AR_im-Au&Pt) 600 µmol of hydrogen was produced.

In the case of using in situ reduction the reference sample (AR_is-Pt) had higher H_2 production rate than the binary composites with the value of 710 µmol.

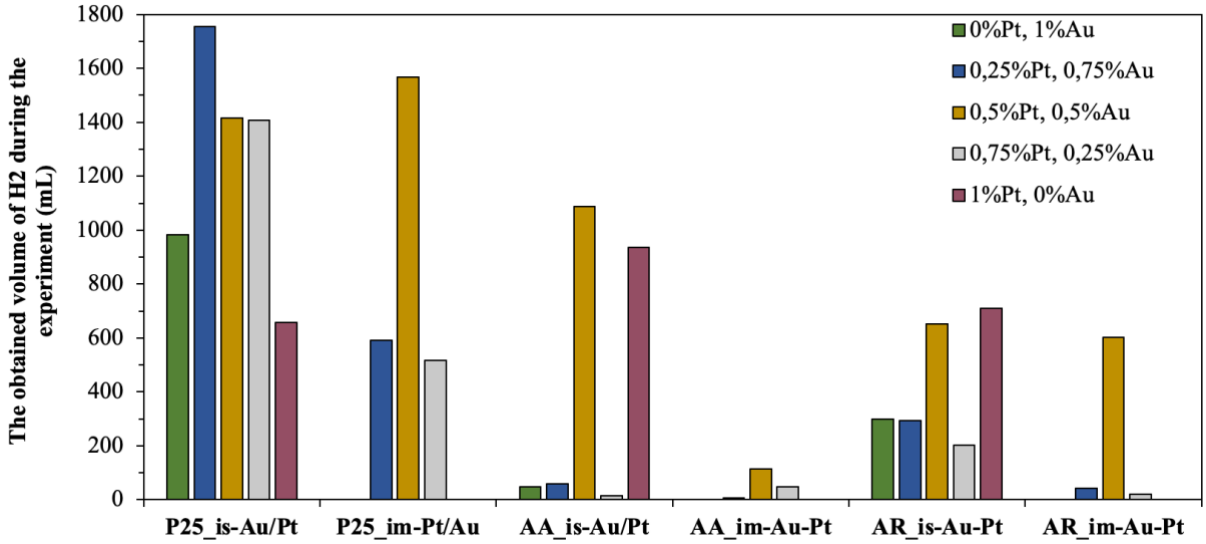

Figure 23. The photocatalytic hydrogen production capacities of the composites. The obtained volume of H_2 is expressed in mL for each composite.

Figure 24. shows the time resolved hydrogen production rates of the composites during the experiment. The best value of all the samples is from the P25 series, named P25_im-Pt/Au. The weakest result was shown, in the same way as the oxalic acid degradation, by the AA composite, named AA_im-Au&Pt.

It is a known fact that for the hydrogen production the presence of the platinum nanoparticles helps produce more H_2: this is demonstrated by the experiments also and by the literature too. Noble metal nanoparticles are needed for shuttling and storing the photogenerated electrons from the titania to the absorbed H^+. Due to the large work function of platinum nanoparticles it is considered the most affective nanoparticle in this field [176]. As mentioned in section 5.1.4.1. if the platinum is located on the surface of gold there are more chances for the hydrogen production. Also, the high specific surface area, and anatase phase are important here as well, that is why the P25 based catalysts produced the most H_2.

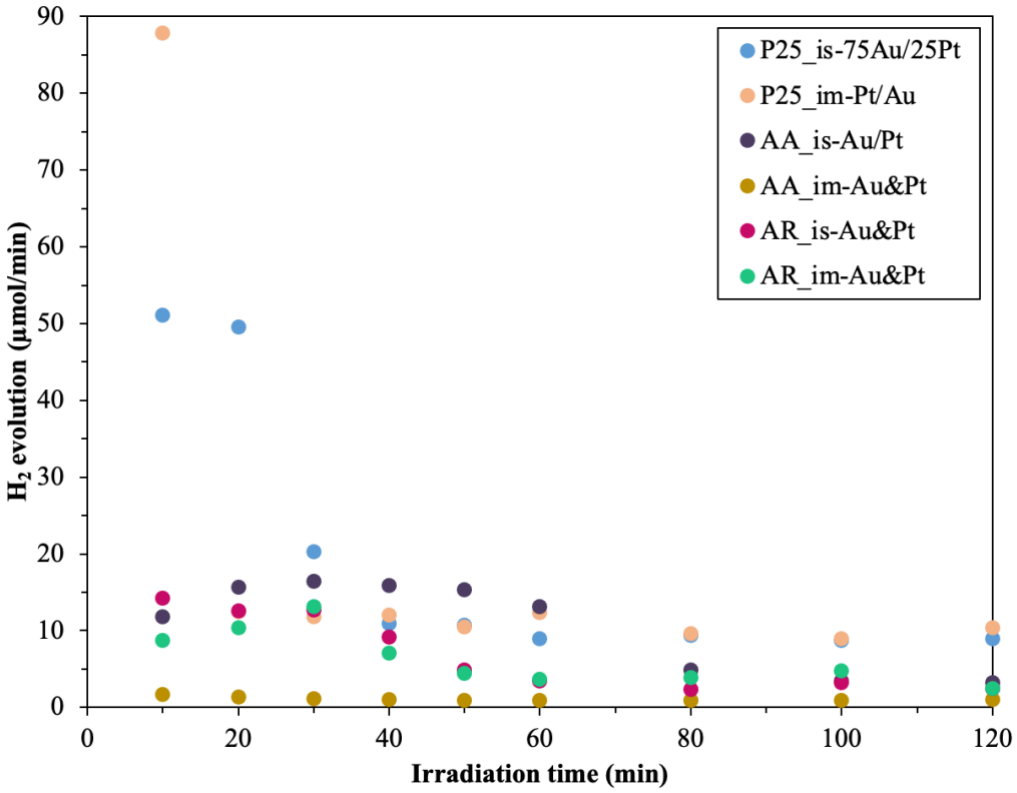

Figure 24. Time resolved hydrogen production rates of the composites which produced the most H_2 – the best value of all the samples is P25_im-Pt/Au.

5.2. Composites consisting of copper nanoparticles and TiO_2

As mentioned beforehand, for a research the price of the prepared and tested materials it is important as well. That is why a side study was performed, where copper nanoparticles were deposited on two of the previously used titanias, on AA and P25.

For the photocatalytic activity, the degradation of methyl orange, ketoprofen, and rhodamine B was performed, which are presented on **Figure 25-27.** Although no better photocatalytic activity was achieved with the composites (both AA- and P25-based ones), it was observed that, for the methyl orange degradation, the samples containing 10% Cu (both AA- and P25-based ones) were the most likely to be able to approach the activity of the base photocatalysts. For ketoprofen degradation, P25-based composites achieved better photocatalytic activity than the base catalyst. In the case of both AA- and P25-based composites, the samples containing 0.5% copper degraded the most in the ketoprofen solution. For the degradation of rhodamine B, 1.5% of the copper nanoparticles was the most suitable value. Finally, on **Figure 28.** the photocatalytic hydrogen production capacity of the produced

composites is shown. Both sets of catalysts managed to develop hydrogen, albeit higher in P25-based ones than those containing AA.

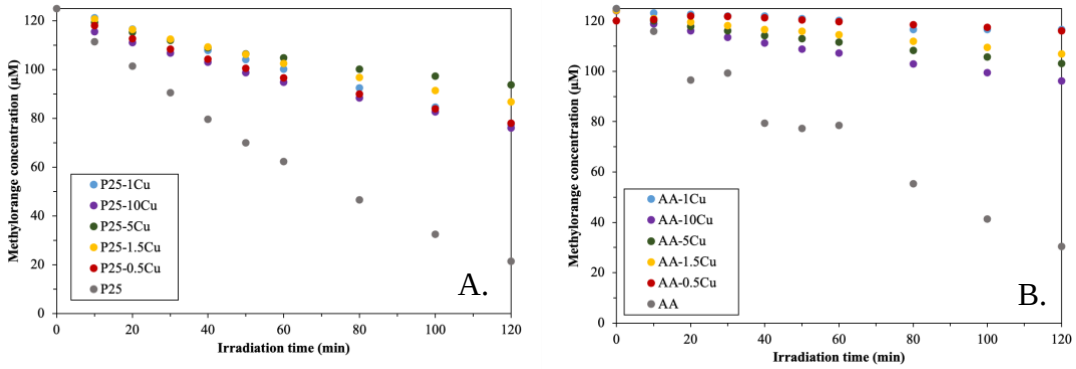

Figure 25. Degradation of methyl orange under UV illumination (A.-P25 based composites, B.-AA based composites) - the composites did not show better activity than the corresponding bare titania. P25-based composites proved to be more efficient than the AA-based ones.

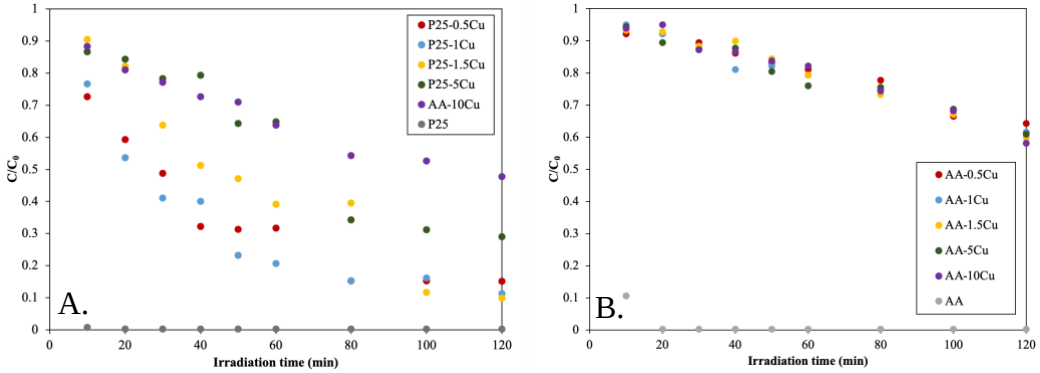

Figure 26. Photocatalytic degradation efficiencies of rhodamine B solution under UV light (A.-P25 based composites, B.-AA based composites) - the P25-based composites showed better activity than the AA-based ones.

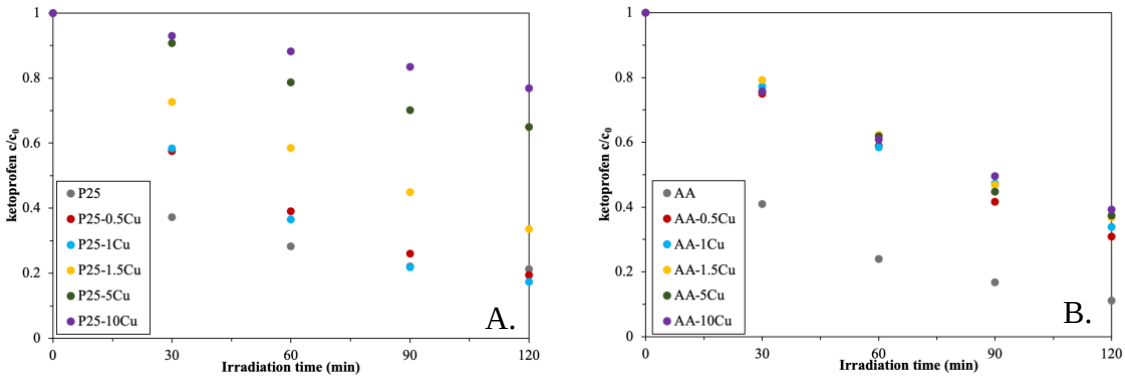

Figure 27. Degradation of ketoprofen under the irradiation of UV light (A.-P25 based composites, B.-AA based composites) - some of the composites achieved better activity than the base catalyst but only in the case of P25.

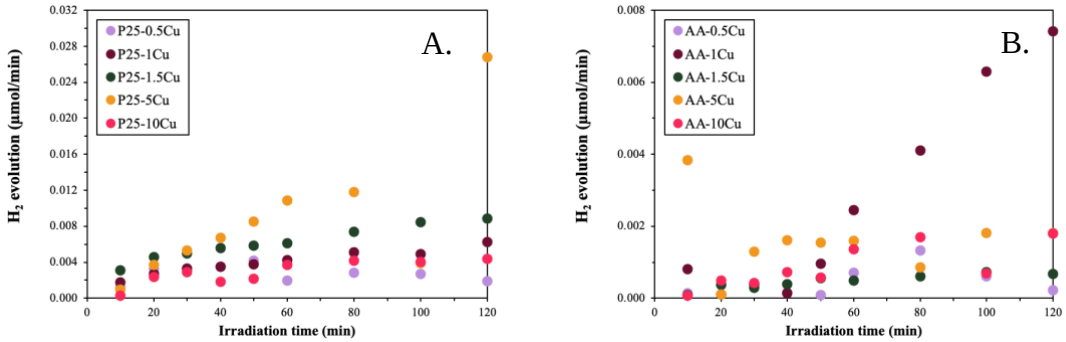

Figure 28. H_2 evolution of the composites (A.-P25 based composites, B.-AA based composites), showing the enhanced H_2 production of P25-based composites.

The above presented results prove that indeed, there are cheaper methods to form composites with TiO_2, but the results may not be as promising as with the composites containing noble metals. However valuable results were gained in this side study, confirming that copper nanoparticles can be used in photocatalysis as well, but maybe sometimes it is worth spending more to achieve better results.

5.3. Composites consisting of lanthanide doped $NaYF_4$, TiO_2 and Au nanoparticle

After the first round of results and studying the literature, a new idea arose. How about enhancing the photocatalytic activity of TiO_2 even further? And how about something new, that no one tried before in our research group?

Thus, it was formed that composites were prepared consisting of TiO_2, lanthanide doped $NaYF_4$ and gold nanoparticles. To challenge myself even more, instead of the commercially available titanias, my goal was to obtain the anatase TiO_2, due to its presumed advantageous properties, which were discussed in the section 2.3. [177,178]. Although it has been shown that copper nanoparticles can be used as photocatalysts, this time I decided to remain with the noble metal nanoparticles, because they proved to be more beneficial. Thus, gold nanoparticles were prepared the same way as before. The reason why only the Au nanoparticles were used lies within its surface plasmon resonance, which could be profitable [179]. Last, but not least, the lanthanide doped $NaYF_4$ was chosen to be the third component of the composite. Theoretically, TiO_2 and gold nanoparticles can utilize the upconverted light, derived from the lanthanide doped $NaYF_4$ [180,181].

5.3.1. Characterization

Based on the **XRD** measurements anatase TiO_2 (JCPDS: 21-1272) and hexagonal $NaYF_4$ [182] (JCPDS: 28-1192) were identified (**Figure 29.**). XRD patterns of the composites containing NYF, TiO_2 and gold nanoparticles are presented in **Figure 29A.**, while the patterns of the samples without NYF are shown in **Figure 29B.** The dots above the patterns indicate the reflections of TiO_2, while the stars indicate the reflections of NYF. There is a minimal difference between the diffraction patterns of the calcined and non-calcined composite samples. In the latter, the peaks are sharpened, indicating an increase in the mean primary crystallite sizes (for example, TiO_2-10.7 nm, TiO_2_calc-13.8 nm), that were calculated with the Scherrer equation and summarized in **Table 5.**

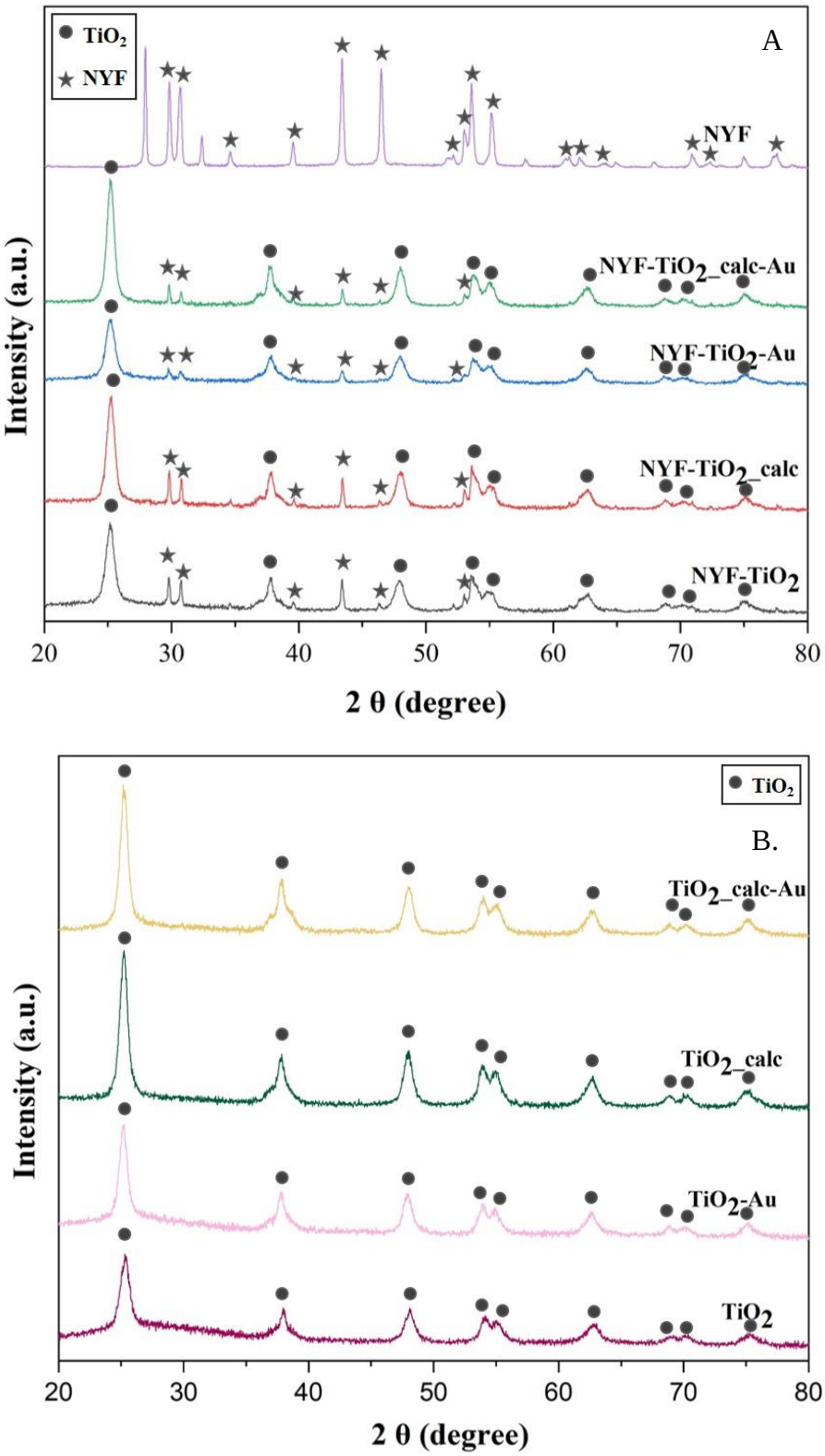

Figure 29. A. - XRD patterns of the composites containing both NYF and TiO_2. The reflections of both materials can be observed, while the reflections of Au nanoparticles were not detectable. B. – XRD patterns of the composites without NYF. The dots indicate the reflections of TiO_2, while the stars indicate the reflections of NYF.

Gold nanoparticles (JCPDS: 04-0784) were not detectable in the Au-containing composites, because their concentration was lower than the detection limit of the instrument, moreover, the gold-specific signals (38°, 45°, 64.5° and 77.5°) overlap with reflections of both TiO_2 and $NaYF_4$. The XRD pattern of the calcined TiO_2-$NaYF_4$ composite was used to calculate the TiO_2:$NaYF_4$ ratio of 71.6:28.4 taking the two most intensive reflections at 25.28° (2θ) for TiO_2 and 53.6° (2θ) for $NaYF_4$ into account.

Based on the data in **Table 5.** it can be seen that the mean primary crystallite size of the TiO_2 and $NaYF_4$ increases, while their specific surface area decreases, as expected.

Table 5. Primary crystallite mean size and band gap energy of the composites.

Sample name	TiO_2 (nm)	$NaYF_4$ (nm)	Band gap energy (eV)
NYF	-	15.3	1.07
TiO_2	10.7	-	1.82
TiO_2_calc	13.8	-	2.97
TiO_2-Au	12.9	-	2.56
TiO_2_calc-Au	13.8	-	2.74
NYF-TiO_2	12.5	11.5	1.82
NYF-TiO_2_calc	13.3	12.2	3.09
NYF-TiO_2-Au	11.6	11.1	2.52
NYF-TiO_2_calc-Au	14.7	12.8	2.87

Based on the **SEM** micrographs of the NYF particles, they have an average length of 5.8–6.8 µm and an average width of 3.2–3.8 µm (**Figure 30.**). It can be observed that a NYF particle has a hollow prism structure with 6 flat surfaces. The calculated mean crystallite sizes derived from the XRD data differ from those determined based on the micrographs, because the Scherrer equation is accurate only for smaller particle sizes (10–80 nm). From the SEM micrographs of TiO_2 and the calcined TiO_2 the following conclusions can be drawn: TiO_2 has an average particle size of 1.5–2.5 µm, the calcination induces a particle size growth, increasing the average size to 4.5–5.5 µm. A similar alteration of the mean primary crystallite size was also obtained from the XRD data.

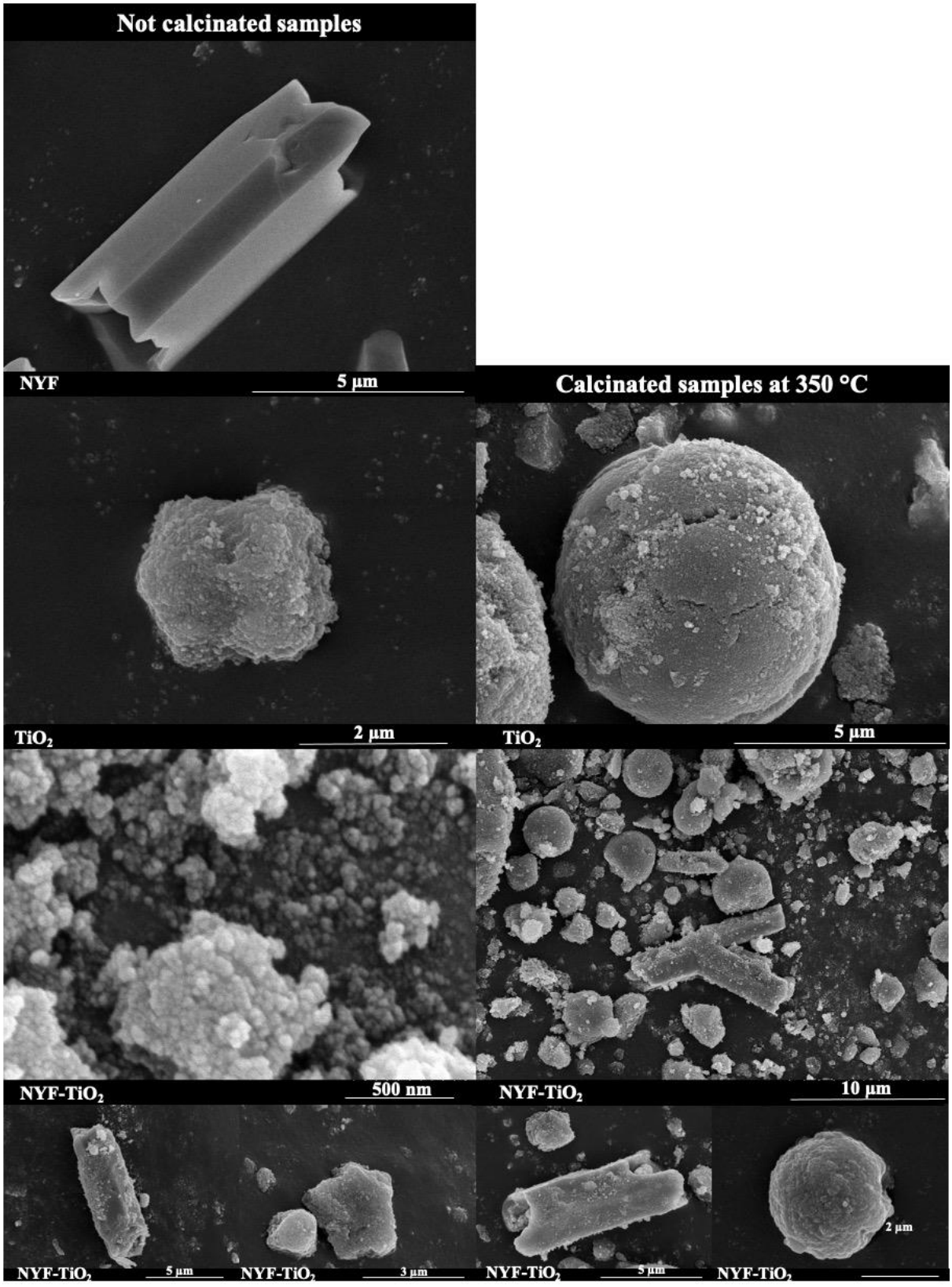

Figure 30. SEM micrographs of the prepared photocatalysts: the first column contains the base catalysts, while the second column contains their heat-treated counterparts.

In **Figure 30.** the left column shows the NYF, TiO_2 and NYF-TiO_2 composite particles, and the right column their calcined counterparts. After calcination the particles that build up the composites have grown, in accordance with the results of the XRD pattern analysis. In addition, these particles have a uniform, smoother surface compared to the samples before calcination. Both spherical and hexagonal particles were formed as it can be seen in the micrographs. Moreover, the structure of the NYF particles is damaged, while irregularly deposited individual TiO_2 crystals can also be found. Furthermore, the effect of calcination does not affect the hollow prism structure of NYF in the composite. The gold nanoparticles cannot be seen in these micrographs, because they are too small to be detected by SEM at the applied magnification. Therefore, EDAX and TEM was used to prove their presence.

In **Figure 31.** the EDAX spectrum of the sample named NYF-TiO_2_calc-Au is presented. All of the constituent elements are present in the composite, therefore the synthesis can be considered successful.

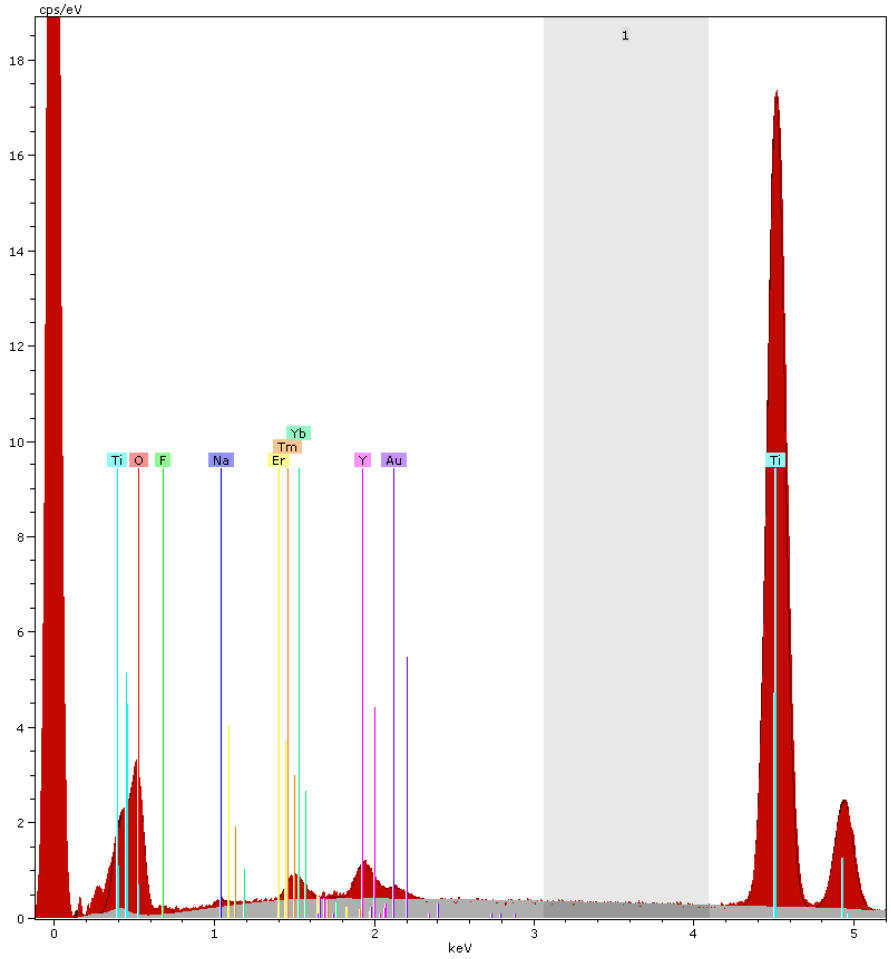

Figure 31. EDAX spectrum of the sample named NYF-TiO_2_calc-Au. All of the constituent elements are present in the composite.

Based on the **TEM** micrographs the gold nanoparticles can be clearly observed as small spheres in the TiO_2-Au, NYF-TiO_2-Au samples, and in their calcined counterparts. **Figure 32.** shows a representative TEM micrograph of the NYF-TiO_2_calc-Au composite sample, where the gold nanoparticles are marked with arrows. As it can be seen in **Figure 33.** the average size of the gold nanoparticles was 5–7 nm, while the average size of TiO_2 particles is 12–14 nm (matching with the calculated results from XRD).

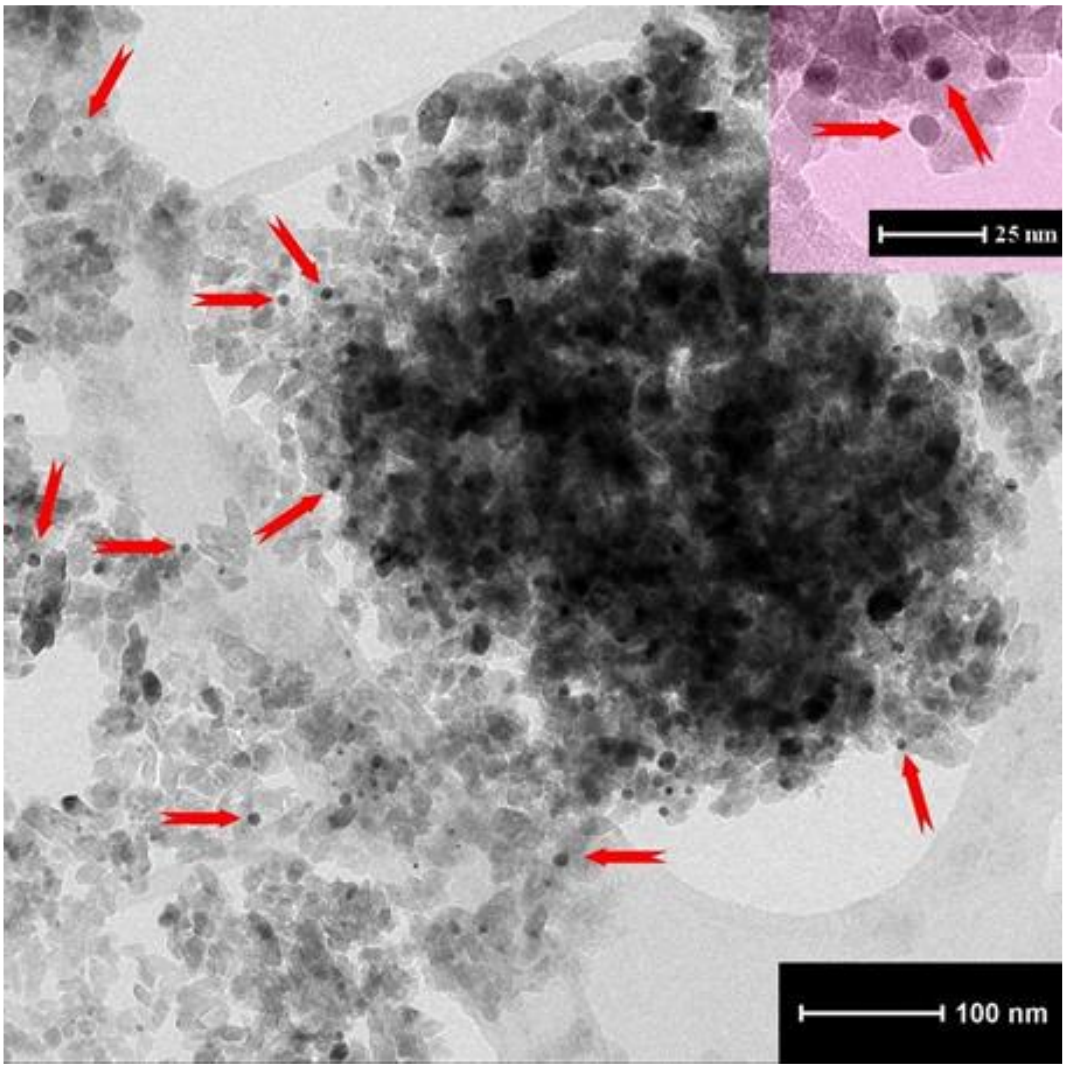

Figure 32. TEM micrograph of NYF-TiO_2_calc-Au: the arrows indicate the positions of the Au nanoparticles, which have spherical shape and an average size of 5–7 nm.

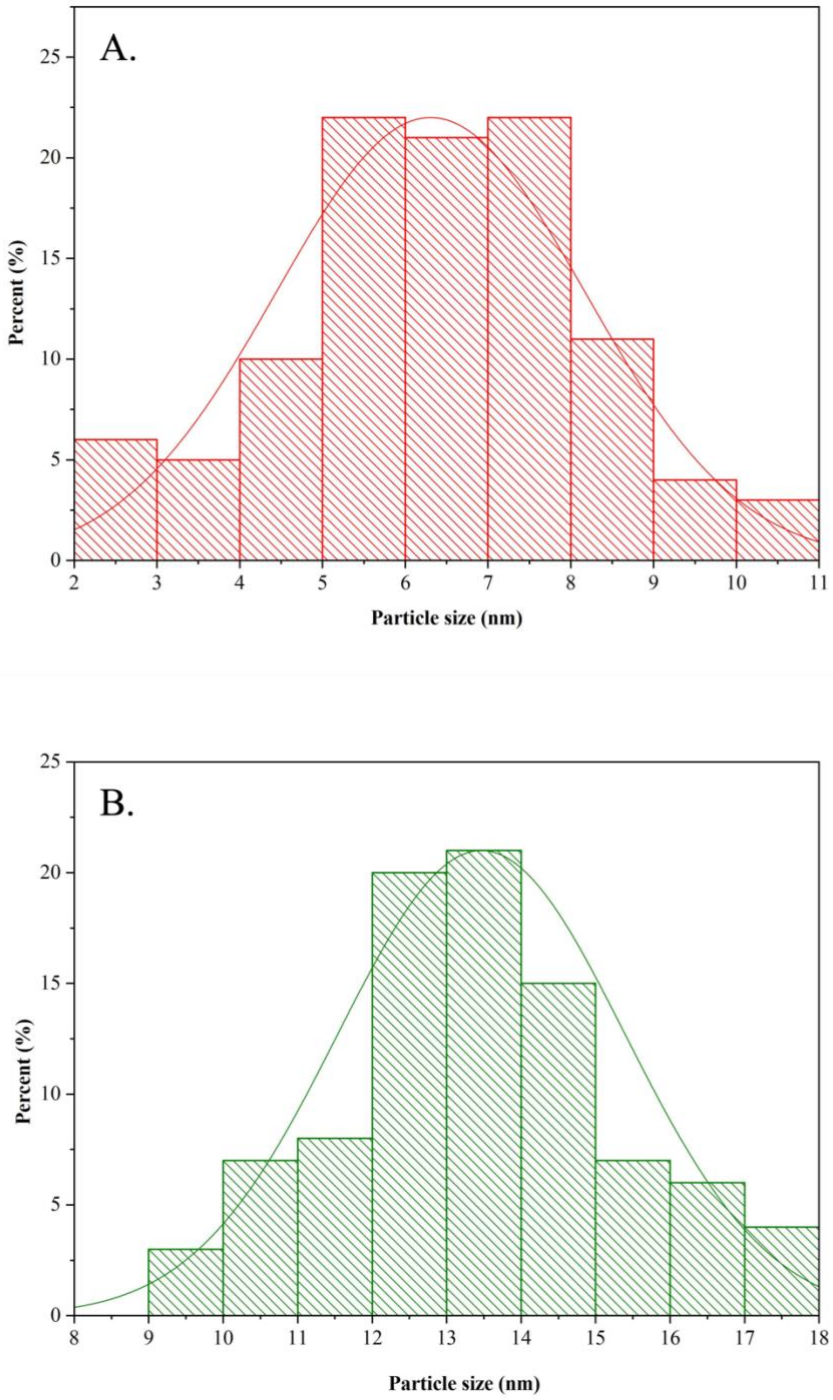

Figure 33. Particle size distribution curve for Au (A) and TiO_2 (B) nanoparticles. The average size of Au being 5-7 nm, while for TiO_2 12-14 nm.

A relatively good dispersion of Au NPs inside the composite can also be observed that ensure the existence of a high number of TiO_2-Au contact points, and consequently improve the degradation efficiency of the samples that contain Au in comparison with those without Au.

The **specific surface area** of the composite samples was determined by nitrogen adsorption and the results are shown in **Figure 34.** TiO_2-Au (163 m^2/g) exhibited the highest specific surface area, while NYF (25 m^2/g) the smallest one. Furthermore, the effect of calcination is also observed here, namely the specific surface area of the samples decreased as the particle size increased. As expected, when a material with lower specific surface area is combined with a sample with higher specific surface area, the resulting specific surface area will be in between those two values [183], as it was the case in this study. The presence of gold facilitated crystallization, therefore it has resulted in the decrease of the specific surface area [184].

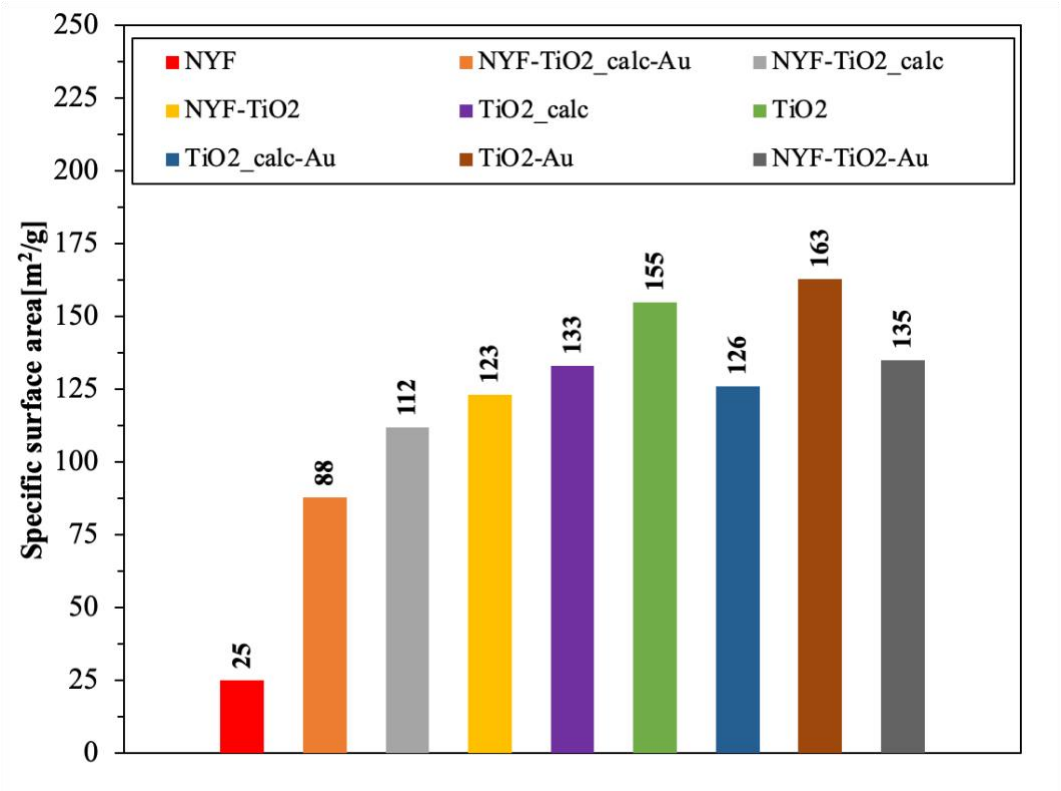

Figure 34. The specific surface area of the composite samples determined by nitrogen adsorption.

The optical properties were investigated by **DRS** measurements. As it can be seen in **Figure 35.** the reflectance values in the visible light region are higher for the calcined samples that do not contain gold nanoparticles. The characteristic plasmonic resonance bands, which appear due to the presence of gold nanoparticles, can be observed at ~550 nm in all composites that contain Au, further reinforcing its presence. Additionally, UV-visible spectroscopy measurements were carried out. In **Figure 36.** the UV-visible spectrum of the gold

nanoparticles is presented. The absorption band at ~500 nm appears due to the surface plasmon resonance of the Au nanoparticles [185].

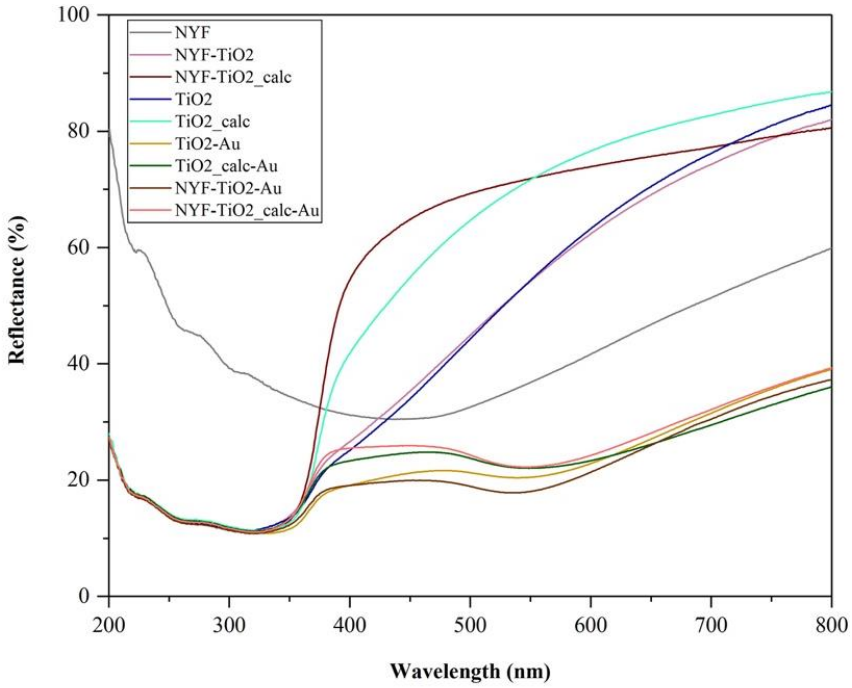

Figure 35. DRS spectra of the prepared samples.

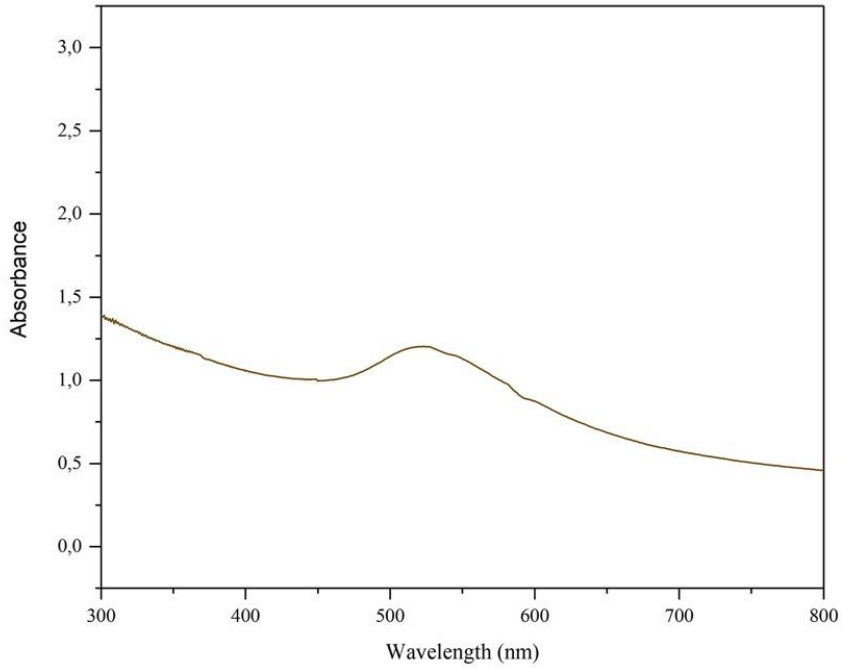

Figure 36. UV-visible spectrum of the gold nanoparticles.

The band gap energies were calculated using the Kubelka-Munk equation and the results were listed in **Table 5.** In all cases, the calcination has led to the increase of the band

gap energy values, implying that these samples became more crystalline. Interestingly, if a sample was not calcined, the loading of gold resulted in the increase of the band gap energy value, and if a gold-containing sample was heat treated then its band gap energy decreased. Another interesting result is the band gap energy of TiO_2, which was calculated to be 1.82 eV.

5.3.2. Photocatalytic activity

In order to test the photocatalytic activity of the prepared composites the degradation of rhodamine B solution was investigated. In **Figure 37.** the photocatalytic activity under UV light is presented.

From the initial and final concentrations of rhodamine B the degradation efficiency was calculated for the prepared samples, and these values are summarized in **Figure 37** and **38.** Results show that among the obtained materials NYF-TiO_2_calc has the highest (86%) decomposition efficiency. Thus, the following order can be established: NYF-TiO_2_calc-Au (75.5%), TiO_2_calc-Au (63.7%), NYF-TiO_2 (49.7%), NYF-TiO_2-Au (48.3%), TiO_2_calc (48.2%), TiO_2-Au (23.2%), TiO_2 (17.3%) and NYF has the lowest degradation efficiency (13.2%).

Furthermore, it can be observed that the calcined counterpart of a composite has a higher efficiency, for example, NYF-TiO_2_calc has an efficiency of 86%, while for the corresponding non-calcined composite (NYF-TiO_2) this value is 49.7%. Calcination promoted crystallization (crystalline anatase is formed), thus increased the photocatalytic activity, this phenomenon was observed by other researchers as well. [169]. The presence of gold in some composites improved the photocatalytic activity, which could be explained as a result of charge separation [186].

Table 6. The surface degradation efficiencies under UV and visible light for the investigated samples.

Sample name	Surface degradation efficiency (UV) (mM/m^2)	Surface Degradation efficiency (Vis) (mM/m^2)
NYF	0.528	0.328
TiO_2	0.111	0.643
TiO_2_calc	0.362	0.466
TiO_2-Au	0.142	0.58
TiO_2_calc-Au	0.505	0.685
NYF-TiO_2	0.404	0.689
NYF-TiO_2_calc	0.767	0.739
NYF-TiO_2-Au	0.357	0.502
NYF-TiO_2_calc-Au	0.857	0.83

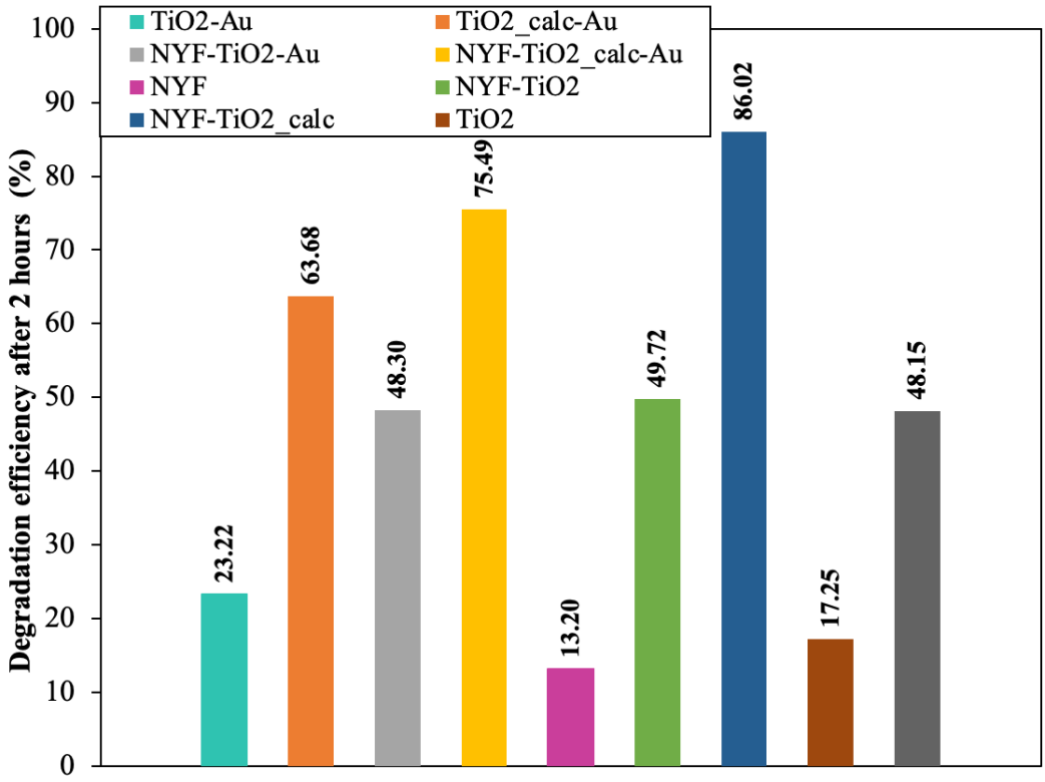

Figure 37. Photocatalytic activity of the composites under UV light.

Similarly to the photocatalytic experiments under UV light, the visible light-degradation efficiency was calculated from the initial and final rhodamine B concentrations, and these values are also summarized in **Figure 38.** From the results it can be concluded that

the prepared composites achieved higher activity in visible light than in UV light. Except for NYF, which had negligible photocatalytic activity (just 8.2%), all composites showed degradation efficiency higher than 60%. TiO_2 decomposed almost all of the rhodamine B even after 60 minutes and its final efficiency was 99.8%, which can be explained by the fact that the band gap energy of TiO_2 is 1.8 eV (already discussed in more detail in Section 3.5). This value was followed closely by TiO_2-Au, with an efficiency of 94.7%. TiO_2_calc-Au, NYF-TiO_2, and NYF-TiO_2_calc had almost the same photocatalytic activity with degradation efficiencies of 86.4%, 84.8%, and 82.8%, respectively. NYF-TiO_2_calc-Au (73.2%), NYF-TiO_2-Au (67.8%) and TiO_2_calc (62%) achieved similar degradation results as well. Calcination did not have such a significant impact on the degradation as in the previous case using UV light irradiation: calcination increased the activity only for NYF-TiO_2-Au (from 67 to 73%). With the deposition of gold nanoparticles, an increase in the activity was expected, however, the presence of gold increased the efficiency only for the TiO_2_calc sample (from 62% to 86.4%). On the other hand, it is worth pointing out that there is no significant difference between the samples with or without Au. Since TiO_2 had the best photocatalytic activity, one can ask why it is worth to deal with the composites. The answer regarding this question lies within the fact that an elucidated mechanism can be provided which can result in further strategies which could lead to higher photocatalytic activity.

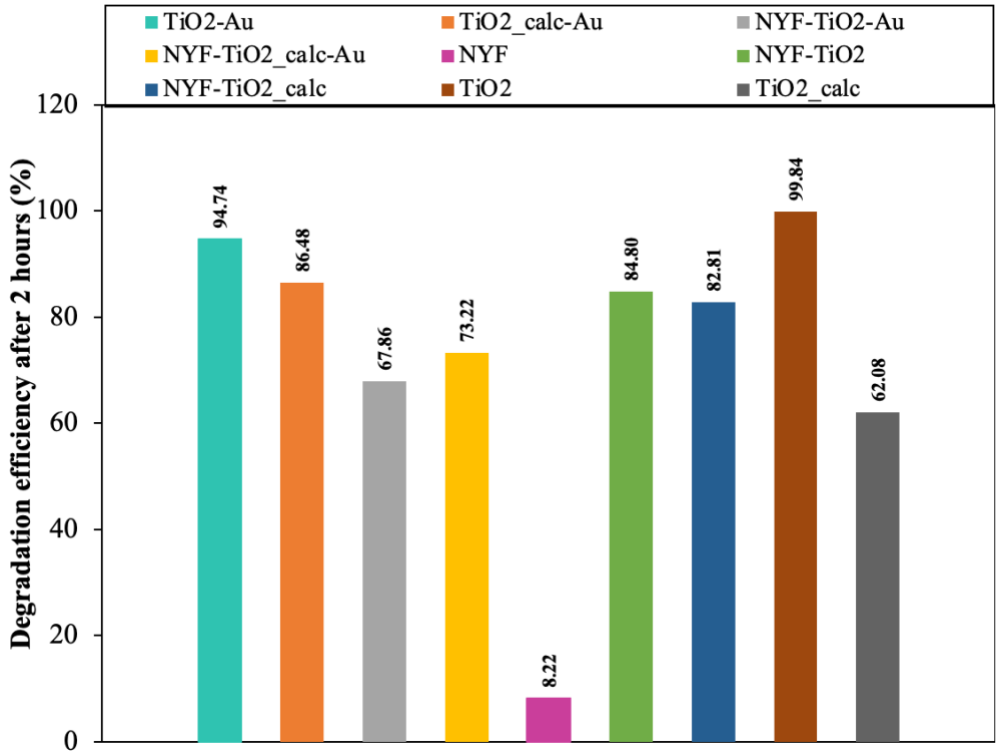

Figure 38. Photocatalytic activity of the composites under visible light.

5.3.3. Photoluminescence measurements and the origin of the activity

The fluorescence measurements were carried out using λ = 365 nm light as the excitation source, because the photocatalytic experiments were also carried out at this wavelength. The following key observations were made:

- when NYF was present in the samples an emission at 460 nm was found, and an asymmetric emission band around 400 nm was also observed. This was the strongest when sample NYF-TiO_2_calc was used. It seems that a down-conversion occurs in these samples, but the emitted light is in the border of UV-A and visible light, that is why under UV irradiation this composite shows high activity.
- Moreover, when Au was deposited the band at 460 nm got weaker, while the one at 400 nm nearly disappeared. As the light emitted at 460 nm was not utilizable by any of the components, the obtained activity for NYF-TiO_2_calc-Au was lower. When the excitation wavelength was changed to 550 nm, no additional fluorescence was observed, therefore the above-registered activity trends were independent from the fluorescence properties of NYF. That is why the best activity was achieved for the TiO_2-Au sample under visible light irradiation.
- Nevertheless, when the excitation wavelength was changed to 900 nm the band at 400 and 460 nm reappeared, pointing out the possible activation of this catalyst under infrared irradiation. For this mechanism to happen the system must go through a set of more complex processes. First, the $^2F_{7/2} \rightarrow {}^2F_{5/2}$ transition must happen in order to absorb the NIR light. For this to happen, Yb^{3+} is the responsible species. The emission band at 400 nm must be the result of the $^1D_2 \rightarrow {}^3H_6$ transition of Tm^{3+} with the possibility of cross relaxing, as the expected wavelength would be around 365 nm. This observation was made by others as well [187]. However, this slight 40 nm difference could originate from the higher energy excitation at 900 nm instead of 980 nm or above. The band at 460 nm seems to originate from Tm^{3+}, as well as from the $^1D_2 \rightarrow {}^3F_4$ transition, meaning that Er^{3+} does not participate in the up-conversion cycle. However, Au could absorb the emitted wavelength above 500 nm, making this transition invisible, while resulting in an electron injection into the conduction band of TiO_2. This finding means that NIR photons can indeed be utilized, however, the buildup of the light path must be carefully developed to maximize the efficiency of this process. Experimental evidence of the NIR activity, with the mechanism proposed above and illustrated in **Figure 5.** was gathered for all the samples. Only in case of sample (NYF-

TiO_2_calc_Au) a 12.5% of degradation was observed. Although, the degradation value seems quite small, it should be mentioned that even such an amount is a great advance, proving that NIR photoactivity is achievable.

To explain the photoactivity, the above-mentioned excitation scenarios can be considered, while not entering in-detail the formation of rhodamine B degradation intermediates and mechanisms (the usual degradation mechanism, driven by direct hole oxidation and OH radical driven degradation). Under UV irradiation, the photoactivity of pure titania can be considered, while a substantial reemission by $NaYF_4$ enhances the activity, by maximizing the overall photon flux, which enters in contact with TiO_2. Interestingly, in case of visible light irradiation the NYF component was inactive, most probably due to the fact that Au was localized mostly on TiO_2, while the latter is not excitable under visible light irradiation. The upconversion mechanism was noticed when carrying out the fluorescence measurements at 900 nm, namely the emission bands at UV and visible light reappeared making possible the excitation pathway detailed in **Figure 5.**

Interestingly, if the amount of degraded rhodamine B was normalized to the available specific surface area the most efficient catalyst would be NYF-TiO_2_calc-Au (**Table 3.**). This shows that the surface quality of this composite is good (the necessary amount of surface defects and catalytically active centers), but due to the lower specific surface area the reemitted light amount and the available surface for the mass transfer is low, thus synthesizing this sample with higher specific surface area shows great potential.

6. Summary

During my research for my Ph.D. thesis a great deal of composites was prepared to improve the photocatalytic activity of TiO_2. The optical and morpho-structural properties of these new materials were investigated in detail.

In the first instance gold and platinum nanoparticles were deposited simultaneously on three different commercial titania photocatalysts: Evonik Aeroxide P25, Aldrich rutile, and Aldrich anatase. For the synthesis of the composites two synthesis strategies were used: in situ and impregnation. As for the noble metal deposition routes two reduction approaches were used: two sequential (Au/Pt, Pt/Au) and one simultaneous (Au&Pt).

The morphological and structural properties were studied/investigated by using XRD, DRS, TEM, HRTEM and EDX. From the XRD it can be concluded that the presence of the noble metals did not influence the semiconductors phase composition and mean crystallite size. Analyzing the DRS spectra, it could be observed that the deposition of noble metal nanoparticles induced significant changes in the optical properties of some commercial titania-based photocatalysts: all composites have smaller band gap energies compared to their base catalyst. In case of AA and AR based composites the decrease of the band gap was less than for the P25 based catalysts, due to the fact that that the particles that build up the base catalysts are significantly smaller in the case of P25 than for AA and AR, and the differences were more accentuated for these particles than for larger particles of the catalysts. The plasmonic band of Au nanoparticles were analyzed in detail. When the plasmonic band did not appear at ≈550 nm two explanations were proposed: the Pt "covers" the Au nanoparticles, forming a so-called core-shell nanostructure or the two noble metals are forming alloys in these binary composites. STEM-HAADF, HRTEM and EDS measurements excluded the presence of core-shell nanoparticles. The obtained size of Au or Pt was between 1 and 5 nm, with a dominance of 3.5 nm particles.

The photocatalytic performances of the nanocomposites were evaluated under UV irradiation, through degradation of oxalic acid and photocatalytic hydrogen production. In general, it can be observed, that the P25-based composites showed the highest photocatalytic efficiencies, degrading more than 75% of the model pollutant. The best performing photocatalyst was obtained by sequential noble metal deposition (first Au followed by Pt) on Evonik Aeroxide P25. As for the hydrogen production capacity, the same composite gave the highest H_2 production rate, as for the oxalic acid degradation.

The last measurement of these composites was the dynamic light scattering to study the agglomeration of the composites prepared with most efficient reduction method, which was in most cases Au/Pt composites and their bare counterparts. The results clearly show that by the deposition of noble metals the titania nanoparticles suffer intense aggregation which was visible with the eye as well.

After the characterization and testing the photocatalytic activity of the composites the oxalic acid degradation and hydrogen production were compared. The samples that most efficiently decomposed oxalic acid or samples that produced the most hydrogen were selected. From each series of photocatalysts - made with the best in situ and impregnation - the composition of the composites was changed. Titanium dioxide remained at 99 wt.%, and the weight ratio of the precious metals was changed to 0.25% - 0.75% and 0.75% - 0.25%, respectively.

The photocatalytic activity and hydrogen production capacity was investigated also. For the oxalic acid degradation, the best photocatalyst was the one that was based on P25, made with in situ method when Au was first reduced then Pt (P25_is-Au/Pt). For the salicylic acid degradation, the best photocatalyst was the one that was based on AA, made with in situ method when Au was first reduced, then Pt (AA_is-Au/Pt). In addition to all, the hydrogen production capacity was investigated as well. The sacrificial agent was the oxalic acid and UV-light was used as well. The most H_2 was produced by the P25 bases sample made with in situ reduction, when first Pt then Au was reduced (P25_is-Pt/Au).

Considering the ratio between the noble metals the following observation can be made: The photocatalytic activity was improved only in the case of the AR based composites for both synthesis strategies after the change in the composition. For the P25 based composites the change in the composition improved the photocatalytic activity for the catalyst made with impregnation. The photocatalytic activity of the AA based composites was not enhanced by the composition change. The hydrogen production capacity was improved only in the case of P25 based catalysts when the concentration of the noble metals was changed, by the composite named P25_is-75Au/25Pt.

In the interest of lowering the price of the prepared composites copper nanoparticles were deposited on two of the commercial titanias (AA and P25). Although, the composites proved to have photocatalytic activity, only some of the composites achieved better activity than the base catalyst and only in the case of the degradation of ketoprofen.

After processing the results from the first round of experiments a new idea arose to enhance the photocatalytic activity of TiO_2 even further. Thus, it was formed that composites

were prepared consisting of TiO_2, lanthanide doped $NaYF_4$ and gold nanoparticles. Instead of the commercially available titanias, the new goal was to obtain the anatase TiO_2, due to its advantageous properties. The noble metal nanoparticles proved to be beneficial, so gold nanoparticles were prepared the same way as before. The reason why only the Au nanoparticles were used lies within its surface plasmon resonance, which could be profitable. Last, but not least, $Yb^{3+,}$ Er^{3+} and Tm^{3+} doped $NaYF_4$ was chosen to be the third component of the composite. Theoretically, TiO_2 and gold nanoparticles can utilize the upconverted light, derived from the lanthanide doped $NaYF_4$.

The morphological and structural properties were studied/investigated by using XRD, SEM, EDAX, TEM, BET method and DRS. Based on the XRD results hexagonal $NaYF_4$ and anatase TiO_2 were obtained. The calcination of the samples increased the primary crystallite sizes. Based on the SEM micrographs the obtained NYF particles had an average length of 5.8–6.8 μm and an average width of 3.2–3.8 μm, while TiO_2 had an average particle size of 1.5–2.5 μm, the calcination induces a particle size growth, increasing the average size to 4.5–5.5 μm, the latter one being a hierarchical structure. The EDAX spectrum proves that all of the constituent elements are present in the composite, therefore the synthesis can be considered successful. The presence of gold nano- particles was proved by TEM, and their average particle size was in the range of 5–7 nm. The specific surface area of the composite samples was determined by nitrogen adsorption. The results showed that TiO_2-Au (163 m^2/g) had the highest specific surface area, while NYF (25 m^2/g) had the smallest one. The optical properties were investigated by DRS measurements. The characteristic plasmonic resonance bands, which appear due to the presence of gold nanoparticles, can be observed at ~550 nm in all composites that contain Au, further reinforcing its presence. The band gap energies were also calculated using the Kubelka-Munk equation. In all cases, the calcination has led to the increase of the band gap energy values, implying that these samples became more crystalline.

The photocatalytic activity was investigated by rhodamine B degradation under the irradiation of UV-, visible and NIR light. As for the degradation under UV light NYF-TiO_2_calc had the highest (86%) decomposition efficiency. Calcination promoted crystallization (crystalline anatase is formed), thus increased the photocatalytic activity. The presence of gold in some composites improved the photocatalytic activity, which could be explained as a result of charge separation. After the degradation under UV light the same experiments were carried out under visible light as well. From the results it can be concluded that the prepared composites achieved higher activity in visible light than in UV light. Calcination did not have such a significant impact on the degradation as in the previous case

using UV light irradiation: calcination increased the activity only for NYF-TiO_2-Au. With the deposition of gold nanoparticles, an increase in the activity was expected, however, the presence of gold increased the efficiency only for the TiO_2_calc sample. After these excellent results came the photodegradation of rhodamine B under NIR light with strong desire for success. Only in case of sample (NYF-TiO_2_calc_Au) a 12.5% of degradation was observed, which seems a quite small degradation efficiency at first. At the same time, in such a less researched field, 4 years is very short time to achieve excellent results, which is why a lot of research is needed in the future to obtain higher efficiency.

In order to understand the origin of the activity photoluminescence measurements were additionally carried out using $\lambda = 365$ nm light as the excitation source. When NYF was present in the samples an emission at 460 nm was found, and an asymmetric emission band around 400 nm was also observed. It seems that a down-conversion occurs in these samples, but the emitted light is in the border of UV-A and visible light, that is why under UV irradiation this composite shows high activity. When Au was deposited the band at 460 nm got weaker, while the one at 400 nm nearly disappeared. When the excitation wavelength was changed to 550 nm, no additional fluorescence was observed, therefore the above-registered activity trends were independent from the fluorescence properties of NYF. Nevertheless, when the excitation wavelength was changed to 900 nm the band at 400 and 460 nm reappeared, pointing out the possible activation of this catalyst under infrared irradiation. Sadly, the experimental results do not support this.

Overall, a great deal of composites were prepared and characterized. The main goal was to increase the photocatalytic activity of TiO_2, which was fulfilled in almost all cases. The photocatalytic activity under NIR light was not successful, although the photoluminescence measurements proved otherwise. The answer may lay in the experimental design, which leaves a new opportunity for a new research.

7. Összefoglalás

A doktori disszertációmhoz kapcsolódó kutatásom során több kompozitot állítottam elő a TiO_2 fotokatalitikus aktivitásának javítása érdekében. Ezen új anyagok optikai és anyagszerkezeti tulajdonságait részletesen megvizsgáltuk.

Először arany és platina nanorészecskéket egyszerre választottam le három különböző kereskedelmi titán dioxid fotokatalizátor felületére: az Evonik Aeroxide P25, az Aldrich rutil és az Aldrich anatázra. A kompozitok szintéziséhez két szintézis stratégiát alkalmaztam: in situ és impregnálás. A nemesfém leválasztási útvonalak esetében két redukciós megközelítést alkalmaztam: két sorozatos (Au / Pt, Pt / Au) és egy egyidejű (Au & Pt).

A morfológiai és szerkezeti tulajdonságokat XRD, DRS, TEM, HRTEM és EDX alkalmazásával vizsgáltuk/tanulmányoztuk. Az XRD-ből arra lehet következtetni, hogy a nemesfémek jelenléte nem befolyásolta a félvezető fázisösszetételt és a kristályok átlagos méretet. A DRS spektrumokat elemezve megfigyelhető volt, hogy a nemesfém nanorészecskék leválasztása jelentős változásokat idézett elő egyes kereskedelmi titán dioxid alapú fotokatalizátorok optikai tulajdonságaiban: az összes kompozitnak kisebb lett a tiltottsáv szélességének az energiája, mint az alapkatalizátoroknak. Az AA és AR alapú kompozitok esetében a tiltottsáv szélesség értékének csökkenése kisebb volt, mint a P25 alapú katalizátoroknál, ami annak a ténynek köszönhető, hogy az alapkatalizátorokat felépítő részecskék lényegesen kisebbek a P25 esetében, mint az AA és AR esetében, és a különbségek jelentősebbek ezeknél a részecskéknél, mint a katalizátorok nagyobb részecskéinél. Az Au nanorészecskék plazmon csúcsát részletesen elemeztük. Amikor a plazmon csúcs nem jelent meg ~ 550 nm hullámhosszon, két magyarázatot vetettünk fel: a Pt „lefedi" az Au nanorészecskéket, úgynevezett mag-héj nanoszerkezetet alkotva, vagy a két nemesfém ötvözetet képez ezekben a tercier kompozitokban. A STEM-HAADF, HRTEM és EDS mérések kizárták a mag-héj nanorészecskék jelenlétét. A kapott Au vagy Pt részecskemérete 1 és 5 nm között volt, 3,5 nm-es részecskék dominanciájával.

A nanokompozitok fotokatalitikus aktivitását UV-fény alatt mértük, oxálsav bontásával és fotokatalitikus hidrogénfejlesztéssel. Általánosságban megfigyelhető, hogy a P25 alapú kompozitok mutatták a legnagyobb fotokatalitikus aktivitást, lebontva a modell szennyező több mint 75%-át. A legjobban teljesítő fotokatalizátort sorozatos nemesfém leválasztással (először Au-t, majd Pt-t) nyertük az Evonik Aeroxide P25-tel. Ami a hidrogénfejlesztést illeti, ugyanaz a kompozit adta a legnagyobb H_2 termelési sebességet, mint az oxálsav lebontása esetén a legnagyobb degradáció %-ot.

Ezekre a kompozitokra az utolsó mérés a dinamikus fényszórás volt, hogy a leghatékonyabb redukciós módszerrel előállított kompozitok agglomerációját tanulmányozzuk, amely a legtöbb esetben az Au/Pt kompozitokat jelentette, illetve az alapkatalizátorokat. Az eredmények egyértelműen azt mutatják, hogy a nemesfémek leválasztása révén a titán dioxid nanorészecskék intenzív aggregációt szenvednek el, amely a szemmel is látható volt.

A jellemzések és a kompozitok fotokatalitikus aktivitásának tesztelése után összehasonlítottuk az oxálsav bontási hatékonyságot és a hidrogéntermelést. Kiválasztottuk azokat a mintákat, amelyek a leghatékonyabban bontották az oxálsavat, vagy azokat a mintákat, amelyek a legtöbb hidrogént termelték. A fotokatalizátorok minden sorozatából - a legjobb in situ és impregnálással készültek - megváltoztattuk a kompozitok összetételét. A titán-dioxid 99 tömeg % maradt, míg a nemesfémek tömegarányát 0,25% - 0,75%, illetve 0,75% - 0,25%-ra változtattuk.

A fotokatalitikus aktivitást és a hidrogénfejlesztő képességet ismét megvizsgáltuk. Az oxálsav bontása szempontjából a legjobb fotokatalizátor az a P25 alapú kompozit volt, amelyet in situ módszerrel állítottam elő, amikor először az Au-t redukáltam, majd Pt-t (P25_is-Au/Pt). A szalicilsav bontásához a legjobb fotokatalizátor az AA alapú kompozit volt, amelyet in situ módszerrel állítottam elő, amikor először az Au-t redukáltam, majd Pt-t (AA_is-Au/Pt). Mindezek mellett megvizsgáltam a hidrogénfejlesztési képességüket is. Az áldozati reagens az oxálsav volt, és UV megvilágítást alkalmaztam. A legtöbb H_2-t az in situ redukcióval készített P25 alapú minta termelte, amikor először Pt-t, majd Au-t redukáltam (P25_is-Pt/Au).

A nemesfémek arányát figyelembe véve a következő megfigyelés tehető: a fotokatalitikus aktivitás csak az AR alapú kompozitok esetében javult mindkét szintézis stratégiához az összetétel megváltozása után. A P25 alapú kompozitok esetében az összetétel megváltozása javította az impregnálással készült katalizátor fotokatalitikus aktivitását. Az AA-alapú kompozitok fotokatalitikus aktivitását az összetétel megváltozása nem javította. A hidrogénfejlesztés csak a P25 alapú katalizátorok esetében javult, amikor a nemesfémek koncentrációját megváltoztattuk, a P25_is-75Au/25Pt elnevezésű kompozit esetében.

Az előállított kompozitok árának csökkentése érdekében réz nanorészecskéket vittem fel két kereskedelmi forgalomban kapható titán-dioxidra (AA és P25). Bár a kompozitok mutattak fotokatalitikus aktivitást, csak néhány kompozit ért el jobb aktivitást, mint az alapkatalizátor, és csak a ketoprofén bontása esetében.

Az első kísérletek eredményeinek feldolgozása után egy új ötlet merült fel a TiO_2 fotokatalitikus aktivitásának további növelésére. Így történt, hogy TiO_2-ból, lantanoida

ionokkal adalékolt $NaYF_4$-ból és arany nanorészecskékből álló kompozitokat állítottam elő. A kereskedelemben kapható titán dioxidok helyett az új cél anatáz TiO_2 előállítása volt, az előnyös tulajdonságainak köszönhetően. A nemesfém nanorészecskék hasznosnak bizonyultak, ezért az arany nanorészecskéket ugyanúgy állítottam elő, mint korábban. Az ok, amiért csak az arany nanorészecskéket tartottam meg, annak felületi plazmonrezonanciájában rejlik, ami nyereséges lehet. Végül, de nem utolsósorban az Yb^{3+}, Er^{3+} és Tm^{3+} ionokkal dópolt $NaYF_4$-ot választottuk a kompozit harmadik összetevőjének. Elméletileg a TiO_2 és az arany nanorészecskék fel tudják használni a lantanoida ionokkal adalékolt $NaYF_4$-tól származó, átalakított fényt.

A szerkezeti és morfológiai tulajdonságokat XRD, SEM, EDAX, TEM, BET módszer és DRS alkalmazásával vizsgáltuk/tanulmányoztuk. Az XRD-ből származó eredmények alapján hexagonális $NaYF_4$-ot és anatáz TiO_2-t kaptunk. A minták kalcinálása megnövelte az elsődleges kristályos méreteket. A SEM felvételek alapján a kapott NYF-részecskék átlagos hossza 5,8–6,8 µm és átlagos szélessége 3,2–3,8 µm volt, míg a TiO_2 átlagos részecskemérete 1,5–2,5 µm, a kalcinálás részecskeméret növekedést váltott ki, így az átlagos méret 4,5–5,5 µm-re nőtt. Az EDAX spektrum bizonyítja, hogy az összes alkotóelem jelen van az kompozitban, ezért a szintézis sikeresnek tekinthető. Az arany nanorészecskék jelenlétét a TEM bizonyította, átlagos részecskeméretük 5–7 nm között volt. A minták fajlagos felületét nitrogén adszorpcióval határoztuk meg. Az eredmények azt mutatták, hogy a TiO_2-Au (163 m^2/g) fajlagos felülete volt a legnagyobb, míg a NYF-é (25 m^2/g) a legkisebb. Az optikai tulajdonságokat DRS mérésekkel vizsgáltuk. A jellegzetes plazmon csúcs, amely az arany nanorészecskék jelenléte miatt jelentkezik, ~550 nm-en megfigyelhetők az összes Au-t tartalmazó kompozitban, tovább erősítve annak jelenlétét. A tiltottsáv szélesség értékeit a Kubelka-Munk egyenlet segítségével számoltuk ki. A kalcinálás minden esetben a tiltottsáv szélesség energiaértékeinek növekedéséhez vezetett, ami azt jelenti, hogy ezek a minták kristályosabbá váltak.

A fotokatalitikus aktivitást rodamin B degradációval vizsgáltuk UV, látható és közeli infravörös (NIR) fény besugárzásával. Ami az UV fény alatt történő bomlást illeti, az NYF-TiO_2_calc rendelkezett a legnagyobb (86%) bomlási hatékonysággal. A kalcinálás elősegítette a kristályosodást (kristályos anatáz képződik), ezáltal fokozta a fotokatalitikus aktivitást. Az arany jelenléte egyes kompozitokban javította a fotokatalitikus aktivitást, ami a töltéselválasztás eredményeként magyarázható. Az UV fény alatt történő bontást követően ugyanezeket a kísérleteket látható fény alatt is elvégeztük. Az eredményekből arra lehet következtetni, hogy az elkészített kompozitok nagyobb aktivitást értek el látható fényben, mint

UV fényben. A kalcinálásnak nem volt olyan jelentős hatása a bontásra, mint az előző esetben UV fénysugárzással: a kalcinálás csak az NYF-TiO_2-Au esetében növelte az aktivitást. Az arany nanorészecskék leválasztásával az aktivitás növekedése volt várható, azonban az arany jelenléte csak a TiO_2_calc minta esetében növelte a hatékonyságot. Ezen kiváló eredmények után a rodamin B fotodegradációja következett NIR fény alatt. Egy minta (NYF-TiO_2_calc_Au) esetében megfigyelhető volt 12,5%-os bontási hatékonyság, ami elsőre kevésnek tűnhet. Ugyanakkor természetesen egy ilyen kevésbé kutatott területen a kiváló eredmények eléréséhez a 4 év igen kevés idő, éppen ezért rengeteg kutatás szükséges a továbbiakban a magasabb hatékonyság eléréséhez.

Az aktivitás eredetének megértése érdekében a továbbiakban fotolumineszcencia méréseket végeztünk, ahol gerjesztési forrásként λ=365 nm fényt alkalmaztunk. Amikor a NYF jelen volt a mintákban, megjelent 460 nm-en egy emissziót, és 400 nm körül egy aszimmetrikus emissziós sávot is megfigyeltünk. Úgy tűnik, hogy ezekben a mintákban 'down-conversion' történik, de a kibocsátott fény az UV-A és a látható fény határában van, ezért UV besugárzás alatt ez a kompozit nagy aktivitást mutat. Amikor Au is jelen volt a sáv 460 nm-nél gyengült, míg a 400 nm-es sáv szinte eltűnt. Amikor a gerjesztési hullámhosszt 550 nm-re változtattuk, további fluoreszcencia nem volt megfigyelhető, ezért a fent bemutatott aktivitási trendek függetlenek a NYF fluoreszcencia tulajdonságaitól. Mindazonáltal, amikor a gerjesztési hullámhosszt 900 nm-re változtattuk, a 400 és 460 nm-es sáv ismét megjelent, rámutatva ennek a katalizátornak az infravörös besugárzás alatt történő lehetséges aktiválására. Sajnos a kísérleti eredmények ezt nem támasztják alá.

Összességében számos kompozitot állítottam elő és jellemeztem. A fő cél a TiO_2 fotokatalitikus aktivitásának növelése volt, amely szinte minden esetben teljesült. A fotokatalitikus aktivitás NIR fény alatt nem volt sikeres, bár a fotolumineszcencia mérések ennek ellenkezőjét bizonyították. A válasz a kísérleti tervezésben rejlik, amely új lehetőséget kínál egy új kutatásra.

8. Acknowledgements

First of all, I would like to express my absolute gratitude to my two supervisors, Prof. Klára Hernádi and Dr. Zsolt Pap who created the opportunity for me to complete my Ph.D. course. I am truly grateful for them for always supporting me and my research ideas, for helping me to achieve my goals and for their scientific guidance. Unquestionably, today I wouldn't be here without their assistance.

I would like to give my special thanks to every member of Environmental Chemistry Research Group, first of all for their friendship, encouragement and support. It helped a lot to be able to work among these cheerful and helping people. From all my colleagues, I would like to especially thank Szilvia Mihálydeákpál, Enikő Bárdos and Dr. Tamás Gyulavári for their contribution of the electron microscopic measurements. My special thank goes also to Kolozsvár, to every member of Bioactive Materials Application of Semiconductors&Sensors research group for always letting me feel welcomed in their laboratory and giving me the opportunity to perform some of my experiment there. I am grateful for calling my colleagues my friends as well.

Last but not least I am infinitely thankful to my family and closest friends for believing in me and for their moral support. I have to highlight my mother who showed me the best example of how to be persistent, humble, and committed for chemistry and my father who always helped me in the practical field of life, for taking part in the construction of the NIR reactor. I am particularly thankful to Hunor, my partner in life, my personal cheerleader who always could make me laugh at the end of the day. Thank you for going through this with me, for inspiring me to be my best version and never letting me give up.

References

1. Hanaor, D.A.H.; Sorrell, C.C. Review of the anatase to rutile phase transformation. *J. Mater. Sci.* **2011**, *46*, 855–874, doi:10.1007/s10853-010-5113-0.
2. Cuerda-Correa, E.M.; Alexandre-Franco, M.F.; Fernandez-Gonzales, C. Advanced Oxidation Processes for the Removal of Antibiotics from Water. An Overview. *Water* **2020**, *12*, 1–50.
3. Poblete, R.; Cortes, E.; Salihoglu, G.; Salihoglu, N.K. Ultrasound and heterogeneous photocatalysis for the treatment of vinasse from pisco production. *Ultrason. Sonochem.* **2020**, *61*, 104825, doi:10.1016/j.ultsonch.2019.104825.
4. Chen, D.; Sivakumar, M.; Ray, A.K. Heterogeneous photocatalysis in environmental remediation. *Dev. Chem. Eng. Miner. Process.* **2000**, *8*, 505–550, doi:10.1002/apj.5500080507.
5. Kaur, R.; Talan, A.; Tiwari, B.; Pilli, S.; Sellamuthu, B.; Tyagi, R.D. *Constructed wetlands for the removal of organic micro-pollutants*; Elsevier B.V., 2020; ISBN 9780128195949.
6. Glaze, W.H.; Kang, J.W.; Chapin, D.H. The chemistry of water treatment processes involving ozone, hydrogen peroxide and ultraviolet radiation. *Ozone Sci. Eng.* **1987**, *9*, 335–352, doi:10.1080/01919518708552148.
7. Deng, Y.; Zhao, R. Advanced Oxidation Processes (AOPs) in Wastewater Treatment. *Curr. Pollut. Reports* **2015**, *1*, 167–176, doi:10.1007/s40726-015-0015-z.
8. Moreira, F.C.; Boaventura, R.A.R.; Brillas, E.; Vilar, V.J.P. Electrochemical advanced oxidation processes: A review on their application to synthetic and real wastewaters. *Appl. Catal. B Environ.* **2017**, *202*, 217–261, doi:10.1016/j.apcatb.2016.08.037.
9. Shinde, S.S.; Bhosale, C.H.; Rajpure, K.Y.; Lee, J.H. Remediation of wastewater: Role of hydroxyl radicals. *J. Photochem. Photobiol. B Biol.* **2014**, *141*, 210–216, doi:10.1016/j.jphotobiol.2014.10.015.
10. Kertèsz, S.; Cakl, J.; Jiránková, H. Submerged hollow fiber microfiltration as a part of hybrid photocatalytic process for dye wastewater treatment. *Desalination* **2014**, *343*, 106–112, doi:10.1016/j.desal.2013.11.013.
11. Feng, L.; van Hullebusch, E.D.; Rodrigo, M.A.; Esposito, G.; Oturan, M.A. Removal of residual anti-inflammatory and analgesic pharmaceuticals from aqueous systems by electrochemical advanced oxidation processes. A review. *Chem. Eng. J.* **2013**, *228*, 944–964, doi:10.1016/j.cej.2013.05.061.

12. Buthiyappan, A.; Abdul Aziz, A.R.; Wan Daud, W.M.A. Recent advances and prospects of catalytic advanced oxidation process in treating textile effluents. *Rev. Chem. Eng.* **2016**, *32*, 1–47, doi:10.1515/revce-2015-0034.
13. Loddo, V.; Bellardita, M.; Camera-Roda, G.; Parrino, F.; Palmisano, L. *Heterogeneous Photocatalysis: A Promising Advanced Oxidation Process*; 2018; ISBN 9780128135495.
14. Liu, H.; Wang, C.; Wang, G. Photocatalytic Advanced Oxidation Processes for Water Treatment: Recent Advances and Perspective. *Chem. - An Asian J.* **2020**, *15*, 3239–3253, doi:10.1002/asia.202000895.
15. Gaya, U.I.; Abdullah, A.H. Heterogeneous photocatalytic degradation of organic contaminants over titanium dioxide: A review of fundamentals, progress and problems. *J. Photochem. Photobiol. C Photochem. Rev.* **2008**, *9*, 1–12, doi:10.1016/j.jphotochemrev.2007.12.003.
16. Zhang, F.; Wang, X.; Liu, H.; Liu, C.; Wan, Y.; Long, Y.; Cai, Z. Recent advances and applications of semiconductor photocatalytic technology. *Appl. Sci.* **2019**, *9*, doi:10.3390/app9122489.
17. Kapinus, E.I.; Khalyavka, T.A.; Shimanovskaya, V. V.; Viktorova, T.I.; Strelko, V. V. Photocatalytic activity of spectro-pure titanium dioxide: Effects of crystalline structure, specific surface area and sorption properties. *Int. J. Photoenergy* **2003**, *5*, 159–166, doi:10.1155/S1110662X0300028X.
18. Carp, O.; Huisman, C.L.; Reller, A. Photoinduced reactivity of titanium dioxide. *Prog. Solid State Chem.* **2004**, *32*, 33–177, doi:10.1016/j.progsolidstchem.2004.08.001.
19. Foster, H.A.; Ditta, I.B.; Varghese, S.; Steele, A. Photocatalytic disinfection using titanium dioxide: Spectrum and mechanism of antimicrobial activity. *Appl. Microbiol. Biotechnol.* **2011**, *90*, 1847–1868, doi:10.1007/s00253-011-3213-7.
20. Pelaez, M.; Nolan, N.T.; Pillai, S.C.; Seery, M.K.; Falaras, P.; Kontos, A.G.; Dunlop, P.S.M.; Hamilton, J.W.J.; Byrne, J.A.; O'Shea, K.; et al. A review on the visible light active titanium dioxide photocatalysts for environmental applications. *Appl. Catal. B Environ.* **2012**, *125*, 331–349, doi:10.1016/j.apcatb.2012.05.036.
21. Zinke, R.K.; Werkheiser, W.H. Critical mineral resources of the United States—Economic and environmental geology and prospects for future supply: U.S. Geological Survey Professional Paper 1802. *Encycl. Toxicol. Third Ed.* **2014**, 797.
22. Allen, N.S.; Mahdjoub, N.; Vishnyakov, V.; Kelly, P.J.; Kriek, R.J. The effect of crystalline phase (anatase, brookite and rutile) and size on the photocatalytic activity of

calcined polymorphic titanium dioxide (TiO2). *Polym. Degrad. Stab.* **2018**, *150*, 31–36, doi:10.1016/j.polymdegradstab.2018.02.008.

23. Di Paola, A.; Bellardita, M.; Palmisano, L. *Brookite, the least known TiO2 photocatalyst*; 2013; Vol. 3; ISBN 3909170250.
24. Bakardjieva, S.; Stengl, V.; Szatmary, L.; Subrt, J.; Lukac, J.; Murafa, N.; Niznansky, D.; Cizek, K.; Jirkovsky, J.; Petrova, N. Transformation of brookite-type TiO 2 nanocrystals to rutile: Correlation between microstructure and photoactivity. *J. Mater. Chem.* **2006**, *16*, 1709–1716, doi:10.1039/b514632a.
25. Lance, R. Optical Analysis of Titania: Band Gaps of Brookite, Rutile and Anatase. **2018**, 24.
26. Samat, M.H.; Ali, A.M.M.; Taib, M.F.M.; Hassan, O.H.; Yahya, M.Z.A. Hubbard U calculations on optical properties of 3d transition metal oxide TiO2. *Results Phys.* **2016**, *6*, 891–896, doi:10.1016/j.rinp.2016.11.006.
27. Haider, A.J.; Jameel, Z.N.; Al-Hussaini, I.H.M. Review on: Titanium dioxide applications. *Energy Procedia* **2019**, *157*, 17–29, doi:10.1016/j.egypro.2018.11.159.
28. Jovanović, B.; Cvetković, V.J.; Mitrović, T.L. Effects of human food grade titanium dioxide nanoparticle dietary exposure on Drosophila melanogaster survival, fecundity, pupation and expression of antioxidant genes. *Chemosphere* **2016**, *144*, 43–49, doi:10.1016/j.chemosphere.2015.08.054.
29. Zhang, L.; Xie, X.; Zhou, Y.; Yu, D.; Deng, Y.; Ouyang, J.; Yang, B.; Luo, D.; Zhang, D.; Kuang, H. Gestational exposure to titanium dioxide nanoparticles impairs the placentation through dysregulation of vascularization, proliferation and apoptosis in mice. *Int. J. Nanomedicine* **2018**, *13*, 777–789, doi:10.2147/IJN.S152400.
30. Baranowska-Wójcik, E.; Szwajgier, D.; Oleszczuk, P.; Winiarska-Mieczan, A. Effects of Titanium Dioxide Nanoparticles Exposure on Human Health—a Review. *Biol. Trace Elem. Res.* **2020**, *193*, 118–129, doi:10.1007/s12011-019-01706-6.
31. Fujishima, A.; Honda, K. Electrochemical Photolysis of Water at a Semiconductor Electrode. *Nature* **1972**, *238*, 37–38.
32. Schneider, J.; Matsuoka, M.; Takeuchi, M.; Zhang, J.; Horiuchi, Y.; Anpo, M.; Bahnemann, D.W. Understanding TiO 2 Photocatalysis Mechanisms and Materials. *Chem. Rev.* **2014**, *114*, 9919−9986.
33. Jangid, N.K.; Jadoun, S.; Yadav, A.; Srivastava, M.; Kaur, N. *Polyaniline-TiO2-based photocatalysts for dyes degradation*; 2020; ISBN 0028902003318.
34. Liu, Y.; Li, Z.; Green, M.; Just, M.; Li, Y.Y.; Chen, X. Titanium dioxide

nanomaterials for photocatalysis. *J. Phys. D. Appl. Phys.* **2017**, *50*, doi:10.1088/1361-6463/aa6500.

35. Guo, Q.; Ma, Z.; Zhou, C.; Ren, Z.; Yang, X. Single Molecule Photocatalysis on TiO2 Surfaces. *Chem. Rev.* **2019**, *119*, 11020–11041, doi:10.1021/acs.chemrev.9b00226.
36. Fujishima, A.; Rao, T.N.; Tryk, D.A. Titanium dioxide photocatalysis. *J. Photochem. Photobiol. C Photochem. Rev.* **2000**, *1*, 1–21.
37. Yang, H.G.; Sun, C.H.; Qiao, S.Z.; Zou, J.; Liu, G.; Smith, S.C.; Cheng, H.M.; Lu, G.Q. Anatase TiO2 single crystals with a large percentage of reactive facets. *Nature* **2008**, *453*, 638–641, doi:10.1038/nature06964.
38. Vittadini, A.; Casarin, M.; Selloni, A. Chemistry of and on TiO2-anatase surfaces by DFT calculations: A partial review. *Theor. Chem. Acc.* **2007**, *117*, 663–671, doi:10.1007/s00214-006-0191-4.
39. Guo, Q.; Zhou, C.; Ma, Z.; Yang, X. Fundamentals of TiO2 Photocatalysis: Concepts, Mechanisms, and Challenges. *Adv. Mater.* **2019**, *31*, 1–26, doi:10.1002/adma.201901997.
40. Ma, Y.; Wang, X.; Jia, Y.; Chen, X.; Han, H.; Li, C. Titanium dioxide-based nanomaterials for photocatalytic fuel generations. *Chem. Rev.* **2014**, *114*, 9987–10043, doi:10.1021/cr500008u.
41. Jiang, X.; Manawan, M.; Feng, T.; Qian, R.; Zhao, T.; Zhou, G.; Kong, F.; Wang, Q.; Dai, S.; Pan, J.H. Anatase and rutile in evonik aeroxide P25: Heterojunctioned or individual nanoparticles? *Catal. Today* **2018**, *300*, 12–17, doi:10.1016/j.cattod.2017.06.010.
42. Uddin, M.J.; Cesano, F.; Chowdhury, A.R.; Trad, T.; Cravanzola, S.; Martra, G.; Mino, L.; Zecchina, A.; Scarano, D. Surface Structure and Phase Composition of TiO2 P25 Particles After Thermal Treatments and HF Etching. *Front. Mater.* **2020**, *7*, 1–12, doi:10.3389/fmats.2020.00192.
43. Moma, J.; Baloyi, J. Modified Titanium Dioxide for Photocatalytic Applications. *Photocatal. - Appl. Attrib.* **2019**, doi:10.5772/intechopen.79374.
44. Xu, Z.; Quintanilla, M.; Vetrone, F.; Govorov, A.O.; Chaker, M.; Ma, D. Harvesting lost photons: Plasmon and upconversion enhanced broadband photocatalytic activity in core@shell microspheres based on lanthanide-doped NaYF4, TiO2, and Au. *Adv. Funct. Mater.* **2015**, *25*, 2950–2960, doi:10.1002/adfm.201500810.
45. Xin, B.; Jing, L.; Ren, Z.; Wang, B.; Fu, H. Effects of simultaneously doped and deposited Ag on the photocatalytic activity and surface states of TiO 2. *J. Phys. Chem.*

B **2005**, *109*, 2805–2809, doi:10.1021/jp0469618.

46. Liu, R.; Wang, P.; Wang, X.; Yu, H.; Yu, J. UV- and visible-light photocatalytic activity of simultaneously deposited and doped Ag/Ag(I)-TiO 2 photocatalyst. *J. Phys. Chem. C* **2012**, *116*, 17721–17728, doi:10.1021/jp305774n.
47. Sung-Suh, H.M.; Choi, J.R.; Hah, H.J.; Koo, S.M.; Bae, Y.C. Comparison of Ag deposition effects on the photocatalytic activity of nanoparticulate TiO2 under visible and UV light irradiation. *J. Photochem. Photobiol. A Chem.* **2004**, *163*, 37–44, doi:10.1016/S1010-6030(03)00428-3.
48. Tian, Y.; Tatsuma, T. Mechanisms and applications of plasmon-induced charge separation at TiO2 films loaded with gold nanoparticles. *J. Am. Chem. Soc.* **2005**, *127*, 7632–7637, doi:10.1021/ja042192u.
49. Ansari, S.A.; Khan, M.M.; Ansari, M.O.; Cho, M.H. Gold nanoparticles-sensitized wide and narrow band gap TiO2 for visible light applications: A comparative study. *New J. Chem.* **2015**, *39*, 4708–4715, doi:10.1039/c5nj00556f.
50. Yoshida, T.; Misu, Y.; Yamamoto, M.; Tanabe, T.; Kumagai, J.; Ogawa, S.; Yagi, S. Effects of the amount of Au nanoparticles on the visible light response of TiO2 photocatalysts. *Catal. Today* **2020**, *352*, 34–38, doi:10.1016/j.cattod.2019.12.035.
51. Fodor, S.; Kovács, G.; Hernádi, K.; Danciu, V.; Baia, L.; Pap, Z. Shape tailored Pd nanoparticles' effect on the photocatalytic activity of commercial TiO2. *Catal. Today* **2017**, *284*, 137–145, doi:10.1016/j.cattod.2016.11.011.
52. Yan, J.; Li, X.; Jin, B.; Zeng, M.; Peng, R. Synthesis of TiO2/Pd and TiO2/PdO Hollow Spheres and Their Visible Light Photocatalytic Activity. *Int. J. Photoenergy* **2020**, *2020*, doi:10.1155/2020/4539472.
53. Hariharan, D.; Thangamuniyandi, P.; Selvakumar, P.; Devan, U.; Pugazhendhi, A.; Vasantharaja, R.; Nehru, L.C. Green approach synthesis of Pd@TiO2 nanoparticles: characterization, visible light active picric acid degradation and anticancer activity. *Process Biochem.* **2019**, *87*, 83–88, doi:10.1016/j.procbio.2019.09.024.
54. Kovács, G.; Fodor, S.; Vulpoi, A.; Schrantz, K.; Dombi, A.; Hernádi, K.; Danciu, V.; Pap, Z.; Baia, L. Polyhedral Pt vs. spherical Pt nanoparticles on commercial titanias: Is shape tailoring a guarantee of achieving high activity? *J. Catal.* **2015**, *325*, 156–167, doi:10.1016/j.jcat.2015.02.008.
55. Qiu, H.; Ma, X.; Sun, C.; Zhao, B.; Chen, F. Surface oxygen vacancies enriched Pt/TiO2 synthesized with a defect migration strategy for superior photocatalytic activity. *Appl. Surf. Sci.* **2020**, *506*, 145021, doi:10.1016/j.apsusc.2019.145021.

56. Zielinska-Jurek, A.; Wei, Z.; Janczarek, M.; Wysocka, I.; Kowalska, E. Size-Controlled Synthesis of Pt Particles on TiO2 Surface: Physicochemical Characteristic and Photocatalytic Activity. *Catalysts* **2019**, *9*, 1–18.
57. Hampel, B.; Pap, Z.; Sapi, A.; Szamosvolgyi, A.; Baia, L.; Hernadi, K. Application of TiO2-Cu composites in photocatalytic degradation different pollutants and hydrogen production. *Catalysts* **2020**, *10*, 1–20, doi:10.3390/catal10010085.
58. Martinelli, A.; Alberti, S.; Caratto, V.; Lova, P.; Locardi, F.; Pampararo, G.; Villa, S.; Ferretti, M. Structural studies on copper and nitrogen doped nanosized anatase. *Zeitschrift fur Krist. - Cryst. Mater.* **2018**, *233*, 867–876, doi:10.1515/zkri-2017-2143.
59. Ohno, T.; Mitsui, T.; Matsumura, M. Photocatalytic activity of S-doped TiO2 photocatalyst under visible light. *Chem. Lett.* **2003**, *32*, 364–365, doi:10.1246/cl.2003.364.
60. Huang, Z.; Gao, Z.; Gao, S.; Wang, Q.; Wang, Z.; Huang, B.; Dai, Y. Facile synthesis of S-doped reduced TiO2-x with enhanced visible-light photocatalytic performance. *Cuihua Xuebao/Chinese J. Catal.* **2017**, *38*, 821–830, doi:10.1016/S1872-2067(17)62825-0.
61. Wang, J.; Tafen, D.N.; Lewis, J.P.; Hong, Z.; Manivannan, A.; Zhi, M.; Li, M.; Wu, N. Origin of photocatalytic activity of Nitrogen-doped TiO2 nanobelts. *J. Am. Chem. Soc.* **2009**, *131*, 12290–12297, doi:10.1021/ja903781h.
62. Zhou, L.; Cai, M.; Zhang, X.; Cui, N.; Chen, G.; Zou, G. yan In-situ nitrogen-doped black TiO2 with enhanced visible-light-driven photocatalytic inactivation of Microcystis aeruginosa cells: Synthesization, performance and mechanism. *Appl. Catal. B Environ.* **2020**, *272*, 119019, doi:10.1016/j.apcatb.2020.119019.
63. Morikawa, T.; Asahi, R.; Ohwaki, T. Visible-light photocatalyst-nitrogen-doped titanium dioxide. *R&D Rev. Toyota CRDL* **2005**, *40*, 45–50.
64. Su, R.; Tiruvalam, R.; Logsdail, A.J.; He, Q.; Downing, C.A.; Jensen, M.T.; Dimitratos, N.; Kesavan, L.; Wells, P.P.; Bechstein, R.; et al. Designer titania-supported Au-Pd nanoparticles for efficient photocatalytic hydrogen production. *ACS Nano* **2014**, *8*, 3490–3497, doi:10.1021/nn500963m.
65. Stroyuk, A.L.; Shvalagin, V. V.; Kuchmii, S.Y. Photochemical synthesis and optical properties of binary and ternary metal-semiconductor composites based on zinc oxide nanoparticles. *J. Photochem. Photobiol. A Chem.* **2005**, *173*, 185–194, doi:10.1016/j.jphotochem.2005.02.002.
66. Arora, N.; Mehta, A.; Mishra, A.; Basu, S. 4-Nitrophenol reduction catalysed by Au-

Ag bimetallic nanoparticles supported on LDH: Homogeneous vs. heterogeneous catalysis. *Appl. Clay Sci.* **2018**, *151*, 1–9, doi:10.1016/j.clay.2017.10.015.

67. Chanu, I.; Krishnamurthi, P.; Manoharan, P.T. Effect of Silver on Plasmonic, Photocatalytic, and Cytotoxicity of Gold in AuAgZnO Nanocomposites. *J. Phys. Chem. C* **2017**, *121*, 9077–9088, doi:10.1021/acs.jpcc.7b02232.
68. Zhang, L.; Mohamed, H.H.; Dillert, R.; Bahnemann, D. Kinetics and mechanisms of charge transfer processes in photocatalytic systems: A review. *J. Photochem. Photobiol. C Photochem. Rev.* **2012**, *13*, 263–276, doi:10.1016/j.jphotochemrev.2012.07.002.
69. Bamwenda, G.R.; Tsubota, S.; Nakamura, T.; Haruta, M. Photoassisted hydrogen production from a water-ethanol solution-a comparison of activities of Au-TiO2 and Pt-TiO2. **1995**, *89*, 177–189.
70. Han, Y.; Ouyang, Y.; Xie, Z.; Chen, J.; Chang, F.; Yu, G. Controlled Growth of Pt–Au Alloy Nanowires and Their Performance for Formic Acid Electrooxidation. *J. Mater. Sci. Technol.* **2016**, *32*, 639–645, doi:10.1016/j.jmst.2016.04.014.
71. Yang, T.; Zhou, N.; Li, Q.; Guan, Q.; Zhang, W.; Jiao, K. Highly sensitive electrochemical impedance sensing of PEP gene based on integrated Au-Pt alloy nanoparticles and polytyramine. *Colloids Surfaces B Biointerfaces* **2012**, *97*, 150–154, doi:10.1016/j.colsurfb.2012.04.007.
72. Verbruggen, S.W.; Keulemans, M.; Filippousi, M.; Flahaut, D.; Van Tendeloo, G.; Lacombe, S.; Martens, J.A.; Lenaerts, S. Plasmonic gold-silver alloy on TiO2 photocatalysts with tunable visible light activity. *Appl. Catal. B Environ.* **2014**, *156–157*, 116–121, doi:10.1016/j.apcatb.2014.03.027.
73. Guo, H.; Kemell, M.; Heikkilä, M.; Leskelä, M. Noble metal-modified TiO2 thin film photocatalyst on porous steel fiber support. *Appl. Catal. B Environ.* **2010**, *95*, 358–364, doi:10.1016/j.apcatb.2010.01.014.
74. Zielińska-Jurek, A.; Hupka, J. Preparation and characterization of Pt/Pd-modified titanium dioxide nanoparticles for visible light irradiation. *Catal. Today* **2014**, *230*, 181–187, doi:10.1016/j.cattod.2013.09.045.
75. Tálas, E.; Pászti, Z.; Korecz, L.; Domján, A.; Németh, P.; Szíjjártó, G.P.; Mihály, J.; Tompos, A. PtOx-SnOx-TiO2 catalyst system for methanol photocatalytic reforming: Influence of cocatalysts on the hydrogen production. *Catal. Today* **2018**, *306*, 71–80, doi:10.1016/j.cattod.2017.02.009.
76. Hajipour, M.J.; Fromm, K.M.; Akbar Ashkarran, A.; Jimenez de Aberasturi, D.;

Larramendi, I.R. de; Rojo, T.; Serpooshan, V.; Parak, W.J.; Mahmoudi, M. Antibacterial properties of nanoparticles. *Trends Biotechnol.* **2012**, *30*, 499–511, doi:10.1016/j.tibtech.2012.06.004.

77. Yang, Z.; Liu, Z.W.; Allaker, R.P.; Reip, P.; Oxford, J.; Ahmad, Z.; Ren, G. A review of nanoparticle functionality and toxicity on the central nervous system. *J. R. Soc. Interface* **2010**, *7*, doi:10.1098/rsif.2010.0158.focus.
78. Jafari, A.; Pourakbar, L.; Farhadi, K.; Mohamadgolizad, L.; Goosta, Y. Biological synthesis of silver nanoparticles and evaluation of antibacterial and antifungal properties of silver and copper nanoparticles. *Turkish J. Biol.* **2015**, *39*, 556–561, doi:10.3906/biy-1406-81.
79. Welch, C.M.; Hyde, M.E.; Banks, C.E.; Compton, R.G. The detection of nitrate using in-situ copper nanoparticle deposition at a boron doped diamond electrode. *Anal. Sci.* **2005**, *21*, 1421–1430, doi:10.2116/analsci.21.1421.
80. Kim, D.; Resasco, J.; Yu, Y.; Asiri, A.M.; Yang, P. Synergistic geometric and electronic effects for electrochemical reduction of carbon dioxide using gold-copper bimetallic nanoparticles. *Nat. Commun.* **2014**, *5*, 1–8, doi:10.1038/ncomms5948.
81. Welch, C.M.; Compton, R.G. The use of nanoparticles in electroanalysis: A review. *Anal. Bioanal. Chem.* **2006**, *384*, 601–619, doi:10.1007/s00216-005-0230-3.
82. Eastman, J.A.; Choi, S.U.S.; Li, S.; Yu, W.; Thompson, L.J. Anomalously increased effective thermal conductivities of ethylene glycol-based nanofluids containing copper nanoparticles. *Appl. Phys. Lett.* **2001**, *78*, 718–720, doi:10.1063/1.1341218.
83. Ranu, B.C.; Dey, R.; Chatterjee, T.; Ahammed, S. Copper nanoparticle-catalyzed carbon-carbon and carbon-heteroatom bond formation with a greener perspective. *ChemSusChem* **2012**, *5*, 22–44, doi:10.1002/cssc.201100348.
84. Ranu, B.C.; Saha, A.; Jana, R. Microwave-assisted simple and efficient ligand free copper nanoparticle catalyzed aryl-sulfur bond formation. *Adv. Synth. Catal.* **2007**, *349*, 2690–2696, doi:10.1002/adsc.200700289.
85. Adams, R.D.; Captain, B.; Fu, W.; Hall, M.B.; Manson, J.; Smith, M.D.; Webster, C.E. Bimetallic Cluster Complexes: The Synthesis, Structures, and Bonding of Ruthenium Carbonyl Cluster Complexes Containing Palladium and Platinum with the Bulky Tri-tert-butyl-phosphine Ligand. *J. Am. Chem. Soc.* **2004**, *126*, 5253–5267, doi:10.1021/ja039541p.
86. Amorós-Pérez, A.; Cano-Casanova, L.; Lillo-Ródenas, M.Á.; Román-Martínez, M.C. Cu/TiO2 photocatalysts for the conversion of acetic acid into biogas and hydrogen.

Catal. Today **2017**, *287*, 78–84, doi:10.1016/j.cattod.2016.09.009.

87. Babu, B.; Mallikarjuna, K.; Reddy, C.V.; Park, J. Facile synthesis of Cu@TiO2 core shell nanowires for efficient photocatalysis. *Mater. Lett.* **2016**, *176*, 265–269, doi:10.1016/j.matlet.2016.04.146.
88. Tseng, I.H.; Wu, J.C.S.; Chou, H.Y. Effects of sol-gel procedures on the photocatalysis of Cu/TiO2 in CO2 photoreduction. *J. Catal.* **2004**, *221*, 432–440, doi:10.1016/j.jcat.2003.09.002.
89. Zhao, X.; Zhang, G.; Zhang, Z. TiO2-based catalysts for photocatalytic reduction of aqueous oxyanions: State-of-the-art and future prospects. *Environ. Int.* **2020**, *136*, doi:10.1016/j.envint.2019.105453.
90. Turkten, N.; Cinar, Z.; Tomruk, A.; Bekbolet, M. Copper-doped TiO2 photocatalysts: application to drinking water by humic matter degradation. *Environ. Sci. Pollut. Res.* **2019**, *26*, 36096–36106, doi:10.1007/s11356-019-04474-x.
91. Park, H.S.; Kim, D.H.; Kim, S.J.; Lee, K.S. The photocatalytic activity of 2.5 wt% Cu-doped TiO2 nano powders synthesized by mechanical alloying. *J. Alloys Compd.* **2006**, *415*, 51–55, doi:10.1016/j.jallcom.2005.07.055.
92. Sahu, M.; Biswas, P. Single-step processing of copper-doped titania nanomaterials in a flame aerosol reactor. *Nanoscale Res. Lett.* **2011**, *6*, 1–14, doi:10.1186/1556-276X-6-441.
93. Daneshvar, N.; Salari, D.; Khataee, A.R. Photocatalytic degradation of azo dye acid red 14 in water on ZnO as an alternative catalyst to TiO2. *J. Photochem. Photobiol. A Chem.* **2004**, *162*, 317–322, doi:10.1016/S1010-6030(03)00378-2.
94. Bica, B.O.; de Melo, J.V.S. Concrete blocks nano-modified with zinc oxide (ZnO) for photocatalytic paving: Performance comparison with titanium dioxide (TiO2). *Constr. Build. Mater.* **2020**, *252*, 119120, doi:10.1016/j.conbuildmat.2020.119120.
95. Neppolian, B.; Choi, H.C.; Sakthivel, S.; Arabindoo, B.; Murugesan, V. Solar/UV-induced photocatalytic degradation of three commercial textile dyes. *J. Hazard. Mater.* **2002**, *89*, 303–317, doi:10.1016/S0304-3894(01)00329-6.
96. Basahel, S.N.; Ali, T.T.; Mokhtar, M.; Narasimharao, K. Influence of crystal structure of nanosized ZrO2 on photocatalytic degradation of methyl orange. *Nanoscale Res. Lett.* **2015**, *10*, doi:10.1186/s11671-015-0780-z.
97. Karunakaran, C.; Senthilvelan, S. Photocatalysis with ZrO2: Oxidation of aniline. *J. Mol. Catal. A Chem.* **2005**, *233*, 1–8, doi:10.1016/j.molcata.2005.01.038.
98. Sang, Y.; Liu, H.; Umar, A. Photocatalysis from UV/Vis to near-infrared light:

Towards full solar-light spectrum activity. *ChemCatChem* **2015**, *7*, 559–573, doi:10.1002/cctc.201402812.

99. Fu, Z.; Zhang, S.; Fu, Z. Hydrothermal preparation of NaTaO3/rGO composite photocatalyst to enhance UV photocatalytic activity. *Results Phys.* **2019**, *15*, 102669, doi:10.1016/j.rinp.2019.102669.
100. Nazari, A. Preparation of Electroconductive, Antibacterial, Photoactive Cotton Fabric Through Green Synthesis of ZnO/reduced Graphene Oxide Nanocomposite. *Fibers Polym.* **2019**, *20*, 2618–2624, doi:10.1007/s12221-019-9180-9.
101. Ngaloy, R.T.; Fontanilla, A.M.; Soriano, M.S.R.; Pascua, C.S.; Matsushita, Y.; Agulo, I.J.A. Highly Efficient Photocatalysis by Zinc Oxide-Reduced Graphene Oxide (ZnO-rGO) Composite Synthesized via One-Pot Room-Temperature Chemical Deposition Method. *J. Nanotechnol.* **2019**, *2019*, doi:10.1155/2019/1895043.
102. Aawani, E.; Memarian, N.; Dizaji, H.R. Synthesis and characterization of reduced graphene oxide–V2O5 nanocomposite for enhanced photocatalytic activity under different types of irradiation. *J. Phys. Chem. Solids* **2019**, *125*, 8–15, doi:10.1016/j.jpcs.2018.09.028.
103. Cheng, L.; Xiang, Q.; Liao, Y.; Zhang, H. CdS-Based photocatalysts. *Energy Environ. Sci.* **2018**, *11*, 1362–1391, doi:10.1039/c7ee03640j.
104. Han, G.; Jin, Y.H.; Burgess, R.A.; Dickenson, N.E.; Cao, X.M.; Sun, Y. Visible-Light-Driven Valorization of Biomass Intermediates Integrated with H2 Production Catalyzed by Ultrathin Ni/CdS Nanosheets. *J. Am. Chem. Soc.* **2017**, *139*, 15584–15587, doi:10.1021/jacs.7b08657.
105. Han, B.; Liu, S.; Zhang, N.; Xu, Y.J.; Tang, Z.R. One-dimensional CdS@MoS2 core-shell nanowires for boosted photocatalytic hydrogen evolution under visible light. *Appl. Catal. B Environ.* **2017**, *202*, 298–304, doi:10.1016/j.apcatb.2016.09.023.
106. Ma, D.; Shi, J.W.; Zou, Y.; Fan, Z.; Ji, X.; Niu, C. Highly Efficient Photocatalyst Based on a CdS Quantum Dots/ZnO Nanosheets 0D/2D Heterojunction for Hydrogen Evolution from Water Splitting. *ACS Appl. Mater. Interfaces* **2017**, *9*, 25377–25386, doi:10.1021/acsami.7b08407.
107. Wu, J.; Bai, S.; Shen, X.; Jiang, L. Preparation and characterization of graphene/CdS nanocomposites. *Appl. Surf. Sci.* **2010**, *257*, 747–751, doi:10.1016/j.apsusc.2010.07.058.
108. Dong, P.; Hou, G.; Xi, X.; Shao, R.; Dong, F. WO3-based photocatalysts: morphology control, activity enhancement and multifunctional applications. *Environ. Sci. Nano*

2017, *4*, 539–557, doi:10.1039/c6en00478d.

109. Fodor, S.; Baia, L.; Focșan, M.; Hernádi, K.; Pap, Z. Designed and controlled synthesis of visible light active copper(I)oxide photocatalyst: From cubes towards the polyhedrons - with Cu nanoparticles. *Appl. Surf. Sci.* **2019**, *484*, 175–183, doi:10.1016/j.apsusc.2019.03.288.
110. Li, G.; Wang, Y.; Mao, L. Recent progress in highly efficient Ag-based visible-light photocatalysts. *RSC Adv.* **2014**, *4*, 53649–53661, doi:10.1039/c4ra08044k.
111. Fu, H.; Pan, C.; Yao, W.; Zhu, Y. Visible-light-induced degradation of rhodamine B by nanosized Bi2WO6. *J. Phys. Chem. B* **2005**, *109*, 22432–22439, doi:10.1021/jp052995j.
112. Tan, H.L.; Amal, R.; Ng, Y.H. Alternative strategies in improving the photocatalytic and photoelectrochemical activities of visible light-driven BiVO4: A review. *J. Mater. Chem. A* **2017**, *5*, 16498–16521, doi:10.1039/c7ta04441k.
113. Lim, S.Y.; Shen, W.; Gao, Z. Carbon quantum dots and their applications. *Chem. Soc. Rev.* **2015**, *44*, 362–381, doi:10.1039/c4cs00269e.
114. Li, H.; Kang, Z.; Liu, Y.; Lee, S.T. Carbon nanodots: Synthesis, properties and applications. *J. Mater. Chem.* **2012**, *22*, 24230–24253, doi:10.1039/c2jm34690g.
115. Zheng, Y.; Liu, J.; Liang, J.; Jaroniec, M.; Qiao, S.Z. Graphitic carbon nitride materials: Controllable synthesis and applications in fuel cells and photocatalysis. *Energy Environ. Sci.* **2012**, *5*, 6717–6731, doi:10.1039/c2ee03479d.
116. Akhavan, O.; Abdolahad, M.; Abdi, Y.; Mohajerzadeh, S. Synthesis of titania/carbon nanotube heterojunction arrays for photoinactivation of E. coli in visible light irradiation. *Carbon N. Y.* **2009**, *47*, 3280–3287, doi:10.1016/j.carbon.2009.07.046.
117. Zhang, H.; Lv, X.; Li, Y.; Wang, Y.; Li, J. P25-graphene composite as a high performance photocatalyst. *ACS Nano* **2010**, *4*, 380–386, doi:10.1021/nn901221k.
118. Gyulavári, T.; Veréb, G.; Pap, Z.; Réti, B.; Baan, K.; Todea, M.; Magyari, K.; Szilágyi, I.M.; Hernadi, K. Utilization of carbon nanospheres in photocatalyst production: From composites to highly active hollow structures. *Materials (Basel).* **2019**, *12*, doi:10.3390/ma12162537.
119. Bakos, L.P.; Justh, N.; Hernádi, K.; Kiss, G.; Réti, B.; Erdélyi, Z.; Parditka, B.; Szilágyi, I.M. Core-shell carbon nanosphere-TiO2 composite and hollow TiO2 nanospheres prepared by atomic layer deposition. *J. Phys. Conf. Ser.* **2016**, *764*, doi:10.1088/1742-6596/764/1/012005.
120. Justh, N.; Bakos, L.P.; Hernádi, K.; Kiss, G.; Réti, B.; Erdélyi, Z.; Parditka, B.;

Szilágyi, I.M. Photocatalytic hollow TiO2 and ZnO nanospheres prepared by atomic layer deposition. *Sci. Rep.* **2017**, *7*, 2–10, doi:10.1038/s41598-017-04090-0.

121. Réti, B.; Mogyorósi, K.; Dombi, A.; Hernádi, K. Substrate dependent photocatalytic performance of TiO2/MWCNT photocatalysts. *Appl. Catal. A Gen.* **2014**, *469*, 153–158, doi:10.1016/j.apcata.2013.10.001.
122. Réti, B.; Major, Z.; Szarka, D.; Boldizsár, T.; Horváth, E.; Magrez, A.; Forró, L.; Dombi, A.; Hernádi, K. Influence of TiO2 phase composition on the photocatalytic activity of TiO2/MWCNT composites prepared by combined sol-gel/hydrothermal method. *J. Mol. Catal. A Chem.* **2016**, *414*, 140–147, doi:10.1016/j.molcata.2016.01.016.
123. Qin, W.; Zhang, D.; Zhao, D.; Wang, L.; Zheng, K. Near-infrared photocatalysis based on YF3:Yb3+, Tm3+/TiO2 core/shell nanoparticles. *Chem. Commun.* **2010**, *46*, 2304–2306, doi:10.1039/b924052g.
124. Kumar, A.; Reddy, K.L.; Kumar, S.; Kumar, A.; Sharma, V.; Krishnan, V. Rational Design and Development of Lanthanide-Doped NaYF4@CdS-Au-RGO as Quaternary Plasmonic Photocatalysts for Harnessing Visible-Near-Infrared Broadband Spectrum. *ACS Appl. Mater. Interfaces* **2018**, *10*, 15565–15581, doi:10.1021/acsami.7b17822.
125. Lingeshwar Reddy, K.; Balaji, R.; Kumar, A.; Krishnan, V. Lanthanide Doped Near Infrared Active Upconversion Nanophosphors: Fundamental Concepts, Synthesis Strategies, and Technological Applications. *Small* **2018**, *14*, 1–27, doi:10.1002/smll.201801304.
126. Zhang, Y.; Hong, Z. Synthesis of lanthanide-doped NaYF4@TiO2 core-shell composites with highly crystalline and tunable TiO2 shells under mild conditions and their upconversion-based photocatalysis. *Nanoscale* **2013**, *5*, 8930–8933, doi:10.1039/c3nr03051b.
127. Xu, J.; Shi, Y.; Chen, Y.; Wang, Q.; Cheng, J.; Li, P. Enhanced photocatalytic activity of TiO2 in visible and infrared light through the synergistic effect of upconversion nanocrystals and quantum dots. *Mater. Res. Express* **2019**, *6*, doi:10.1088/2053-1591/aaf1f2.
128. Huang, H.; Li, H.; Wang, Z.; Wang, P.; Zheng, Z.; Liu, Y.; Dai, Y.; Li, Y.; Huang, B. Efficient near-infrared photocatalysts based on NaYF4:Yb3+,Tm3+@NaYF4:Yb3+,Nd3+@TiO2 core@shell nanoparticles. *Chem. Eng. J.* **2019**, *361*, 1089–1097, doi:10.1016/j.cej.2018.12.174.
129. Wang, W.; Huang, W.; Ni, Y.; Lu, C.; Xu, Z. Different upconversion properties of β-

NaYF4:Yb 3+,Tm3+/Er3+ in affecting the near-infrared-driven photocatalytic activity of high-reactive TiO2. *ACS Appl. Mater. Interfaces* **2014**, *6*, 340–348, doi:10.1021/am404389g.

130. Cushing, S.K.; Li, J.; Meng, F.; Senty, T.R.; Suri, S.; Zhi, M.; Li, M.; Bristow, A.D.; Wu, N. Photocatalytic activity enhanced by plasmonic resonant energy transfer from metal to semiconductor. *J. Am. Chem. Soc.* **2012**, *134*, 15033–15041, doi:10.1021/ja305603t.
131. Craciun, A.M.; Focsan, M.; Magyari, K.; Vulpoi, A.; Pap, Z. Surface plasmon resonance or biocompatibility-key properties for determining the applicability of noble metal nanoparticles. *Materials (Basel).* **2017**, *10*, doi:10.3390/ma10070836.
132. Wang, Y.; Zhu, Y.; Yang, X.; Shen, J.; Zhu, J.; Qian, S.; Li, C. Plasmonic Au Decorated Single-crystal-like TiO2-NaYF4 Mesoporous Microspheres for Enhanced Broadband Photocatalysis. *Chinese J. Chem.* **2017**, *35*, 949–956, doi:10.1002/cjoc.201600771.
133. Chang, M.; Wang, M.; Shu, M.; Zhao, Y.; Ding, B.; Huang, S.; Hou, Z.; Han, G.; Lin, J. Enhanced photoconversion performance of NdVO4/Au nanocrystals for photothermal/photoacoustic imaging guided and near infrared light-triggered anticancer phototherapy. *Acta Biomater.* **2019**, *99*, 295–306, doi:10.1016/j.actbio.2019.08.026.
134. Chen, M.; Wang, J.H.; Luo, Z.J.; Cheng, Z.Q.; Zhang, Y.F.; Yu, X.F.; Zhou, L.; Wang, Q.Q. Facile synthesis of flower-shaped Au/GdVO4:Eu core/shell nanoparticles by using citrate as stabilizer and complexing agent. *RSC Adv.* **2016**, *6*, 9612–9618, doi:10.1039/c5ra23958c.
135. Barolet, D.; Christiaens, F.; Hamblin, M.R. Infrared and skin: Friend or foe. *J. Photochem. Photobiol. B Biol.* **2016**, *155*, 78–85, doi:10.1016/j.jphotobiol.2015.12.014.
136. Tian, Q.; Yao, W.; Wu, W.; Jiang, C. NIR light-activated upconversion semiconductor photocatalysts. *Nanoscale Horizons* **2019**, *4*, 10–25, doi:10.1039/c8nh00154e.
137. Méndez-Ramos, J.; Acosta-Mora, P.; Ruiz-Morales, J.C.; Sierra, M.; Redondas, A.; Ruggiero, E.; Salassa, L.; Borges, M.E.; Esparza, P. Rare-earth doped colour tuneable up-conversion ZBLAN phosphor for enhancing photocatalysis. *Opt. Mater. (Amst).* **2015**, *41*, 98–103, doi:10.1016/j.optmat.2014.10.045.
138. Kalyani, T.N.; Swart, H.; Dhoble, S.J. *Principles and applications of organic light emitting diodes (OLEDs)*; Woodhead Publishing Series in Electronic and Optical

Materials, 2017; ISBN 9781437778236.

139. Wouterlood, F.G.; Boekel, A.J. Fluorescence Microscopy in the Neurosciences. *Encycl. Neurosci.* **2009**, 253–260, doi:10.1016/B978-008045046-9.00666-5.
140. Valeur, B.; Berberan-Santos, M.N. A brief history of fluorescence and phosphorescence before the emergence of quantum theory. *J. Chem. Educ.* **2011**, *88*, 731–738, doi:10.1021/ed100182h.
141. Gamelin, D.R.; Güdel, H.U. Design of luminescent inorganic materials: New photophysical processes studied by optical spectroscopy. *Acc. Chem. Res.* **2000**, *33*, 235–242, doi:10.1021/ar990102y.
142. Safdar, M.; Ghazy, A.; Lastusaari, M.; Karppinen, M. Lanthanide-based inorganic-organic hybrid materials for photon-upconversion. *J. Mater. Chem. C* **2020**, *8*, 6946–6965, doi:10.1039/d0tc01216e.
143. Wang, R.; Zhang, F. NIR luminescent nanomaterials for biomedical imaging. *J. Mater. Chem. B* **2014**, *2*, 2422–2443, doi:10.1039/c3tb21447h.
144. Chen, C.; Li, C.; Shi, Z. Current Advances in Lanthanide-Doped Upconversion Nanostructures for Detection and Bioapplication. *Adv. Sci.* **2016**, *3*, doi:10.1002/advs.201600029.
145. Wang, Y. The role of an inert shell in improving energy utilization in lanthanide-doped upconversion nanoparticles. *Nanoscale* **2019**, *11*, 10852–10858, doi:10.1039/c9nr03205c.
146. Xu, B.; Li, D.; Huang, Z.; Tang, C.; Mo, W.; Ma, Y. Alleviating luminescence concentration quenching in lanthanide doped CaF2 based nanoparticles through Na+ ion doping. *Dalt. Trans.* **2018**, *47*, 7534–7540, doi:10.1039/c8dt00519b.
147. Wang, F.; Liu, X. Recent advances in the chemistry of lanthanide-doped upconversion nanocrystals. *Chem. Soc. Rev.* **2009**, *38*, 976–989, doi:10.1039/b809132n.
148. Gulzar, A.; Xu, J.; Yang, P.; He, F.; Xu, L. Upconversion processes: Versatile biological applications and biosafety. *Nanoscale* **2017**, *9*, 12248–12282, doi:10.1039/c7nr01836c.
149. Bettinelli, M.; Carlos, L.; Liu, X. Lanthanide-doped upconversion nanoparticles. *Phys. Today* **2015**, *68*, 38–44, doi:10.1063/PT.3.2913.
150. Zhu, X.; Zhang, J.; Liu, J.; Zhang, Y. Recent Progress of Rare-Earth Doped Upconversion Nanoparticles: Synthesis, Optimization, and Applications. *Adv. Sci.* **2019**, *6*, doi:10.1002/advs.201901358.
151. Gao, D.; Zhang, X.; Gao, W. Tuning upconversion emission by controlling particle

shape in NaYF4:Yb3+/Er3+ nanocrystals. *J. Appl. Phys.* **2012**, *111*, 3–8, doi:10.1063/1.3681293.

152. Zhang, F. *Photon Upconversion Nanomaterials*; Springer, 2017; Vol. 3; ISBN 9783662455968.
153. Chen, D.; Yu, Y.; Huang, F.; Huang, P.; Yang, A.; Wang, Z.; Wang, Y. Monodisperse upconversion Er3+/Yb3+:MFCl (M = Ca, Sr, Ba) nanocrystals synthesized via a seed-based chlorination route. *Chem. Commun.* **2011**, *47*, 11083–11085, doi:10.1039/c1cc13763h.
154. Gong, G.; Xie, S.; Song, Y.; Tan, H.; Xu, J.; Zhang, C.; Xu, L. Synthesis of Lanthanide-Ion-Doped NaYF 4 RGB Up-Conversion Nanoparticles for Anti-Counterfeiting Application . *J. Nanosci. Nanotechnol.* **2018**, *18*, 8207–8215, doi:10.1166/jnn.2018.15801.
155. Liang, G.; Wang, H.; Shi, H.; Wang, H.; Zhu, M.; Jing, A.; Li, J.; Li, G. Recent progress in the development of upconversion nanomaterials in bioimaging and disease treatment. *J. Nanobiotechnology* **2020**, *18*, 1–22, doi:10.1186/s12951-020-00713-3.
156. Saha, S.; Pala, R.G.S.; Sivakumar, S. Catalyzing Cubic-to-Hexagonal Phase Transition in NaYF4 via Ligand Enhanced Surface Ordering. *Cryst. Growth Des.* **2018**, *18*, 5080–5088, doi:10.1021/acs.cgd.8b00535.
157. Shi, F.; Zhai, X.; Zheng, K.; Zhao, D.; Qin, W. Synthesis of monodisperse NaYF 4:Yb, Tm@SiO 2 nanoparticles with intense ultraviolet upconversion luminescence. *J. Nanosci. Nanotechnol.* **2011**, *11*, 9912–9915, doi:10.1166/jnn.2011.5248.
158. Rodríguez-Sevilla, P.; Zhang, Y.; Haro-González, P.; Sanz-Rodríguez, F.; Jaque, F.; Solé, J.G.; Liu, X.; Jaque, D. Thermal Scanning at the Cellular Level by an Optically Trapped Upconverting Fluorescent Particle. *Adv. Mater.* **2016**, *28*, 2421–2426, doi:10.1002/adma.201505020.
159. Ramasamy, P.; Kim, J. Combined plasmonic and upconversion rear reflectors for efficient dye-sensitized solar cells. *Chem. Commun.* **2014**, *50*, 879–881, doi:10.1039/c3cc47290f.
160. Shang, M.; Geng, D.; Kang, X.; Yang, D.; Zhang, Y.; Lin, J. Hydrothermal derived LaOF:Ln 3+ (Ln = Eu, Tb, Sm, Dy, Tm, and/or Ho) nanocrystals with multicolor-tunable emission properties. *Inorg. Chem.* **2012**, *51*, 11106–11116, doi:10.1021/ic301662c.
161. Yb, U.N.; Upconversion, E.; Wang, M.; Mi, C.; Wang, W.; Liu, C.; Wu, Y.; Xu, Z.; Mao, B.; Xu, S. Immunolabeling and NIR-Excited Fluorescent Imaging ofHeLa Cells

by Using NaYF4:Yb,Er Upconversion Nanoparticles. *3*, 1580–1586.

162. Klier, D.T.; Kumke, M.U. Analysing the effect of the crystal structure on upconversion luminescence in Yb3+,Er3+-co-doped NaYF4 nanomaterials. *J. Mater. Chem. C* **2015**, *3*, 11228–11238, doi:10.1039/c5tc02218e.
163. Pin, M.W.; Park, E.J.; Choi, S.; Kim, Y. Il; Jeon, C.H.; Ha, T.H.; Kim, Y.H. Atomistic evolution during the phase transition on a metastable single NaYF4:Yb,Er upconversion nanoparticle. *Sci. Rep.* **2018**, *8*, 1–10, doi:10.1038/s41598-018-20702-9.
164. Chen, G.; Qiu, H.; Prasad, P.N.; Chen, X. Upconversion nanoparticles: Design, nanochemistry, and applications in Theranostics. *Chem. Rev.* **2014**, *114*, 5161–5214, doi:10.1021/cr400425h.
165. Auzel, F. Upconversion and Anti-Stokes Processes with f and d Ions in Solids. *Chem. Rev.* **2004**, *104*, 139–173, doi:10.1021/cr020357g.
166. Shyichuk, A.; Câmara, S.S.; Weber, I.T.; Carneiro Neto, A.N.; Nunes, L.A.O.; Lis, S.; Longo, R.L.; Malta, O.L. Energy transfer upconversion dynamics in YVO4:Yb3+,Er3+. *J. Lumin.* **2016**, *170*, 560–570, doi:10.1016/j.jlumin.2015.07.005.
167. Joubert, M.F. Photon avalanche upconversion in rare earth laser materials. *Opt. Mater. (Amst).* **1999**, *11*, 181–203, doi:10.1016/S0925-3467(98)00043-3.
168. Kmetykó, Á.; Mogyorósi, K.; Pusztai, P.; Radu, T.; Kónya, Z.; Dombi, A.; Hernádi, K. Photocatalytic H2 evolution using different commercial TiO2 catalysts deposited with finely size-tailored au nanoparticles: Critical dependence on au particle size. *Materials (Basel).* **2014**, *7*, 7615–7633, doi:10.3390/ma7127615.
169. Soo, J.Z.; Ang, B.C.; Ong, B.H. Influence of calcination on the morphology and crystallinity of titanium dioxide nanofibers towards enhancing photocatalytic dye degradation. *Mater. Res. Express* **2019**, *6*, doi:10.1088/2053-1591/aaf013.
170. Jenkins, R.; Snyder, R. Introduction to X-ray Powder Diffractometry. *John Wiley Sons* **1996**, 47–95.
171. Murphy, A.B. Band-gap determination from diffuse reflectance measurements of semiconductor films, and application to photoelectrochemical water-splitting. *Sol. Energy Mater. Sol. Cells* **2007**, *91*, 1326–1337, doi:10.1016/j.solmat.2007.05.005.
172. Qian, L.; Sha, Y.; Yang, X. Simple and convenient preparation of Au-Pt core-shell nanoparticles on surface via a seed growth method. *Thin Solid Films* **2006**, *515*, 1349–1353, doi:10.1016/j.tsf.2006.03.036.
173. Xue, J.; Ma, S.; Zhou, Y.; Zhang, Z.; He, M. Facile photochemical synthesis of Au/Pt/g-C3N4 with plasmon-enhanced photocatalytic activity for antibiotic

degradation. *ACS Appl. Mater. Interfaces* **2015**, *7*, 9630–9637, doi:10.1021/acsami.5b01212.

174. Hampel, B.; Kovács, G.; Czekes, Z.; Hernádi, K.; Danciu, V.; Ersen, O.; Girleanu, M.; Focşan, M.; Baia, L.; Pap, Z. Mapping the Photocatalytic Activity and Ecotoxicology of Au, Pt/TiO2 Composite Photocatalysts. *ACS Sustain. Chem. Eng.* **2018**, *6*, 12993–13006, doi:10.1021/acssuschemeng.8b02465.
175. Regazzoni, A.E.; Mandelbaum, P.; Matsuyoshi, M.; Schiller, S.; Bilmes, S.A.; Blesa, M.A. Adsorption and photooxidation of salicylic acid on titanium dioxide: A surface complexation description. *Langmuir* **1998**, *14*, 868–874, doi:10.1021/la970665n.
176. Khan, M. 美国科学院学报 Materials Chemistry A 材料化学 a. *J. Mater. Chem. A* **2015**, 121.
177. Bui, V.K.H.; Van Tran, V.; Moon, J.Y.; Park, D.; Lee, Y.C. Titanium dioxide microscale and macroscale structures: A mini-review. *Nanomaterials* **2020**, *10*, 1–31, doi:10.3390/nano10061190.
178. Bui, V.K.H.; Park, D.; Lee, Y.C. Chitosan combined with ZnO, TiO2 and Ag nanoparticles for antimicrobialwound healing applications: A mini review of the research trends. *Polymers (Basel).* **2017**, *9*, doi:10.3390/polym9010021.
179. Huang, X.; El-Sayed, M.A. Gold nanoparticles: Optical properties and implementations in cancer diagnosis and photothermal therapy. *J. Adv. Res.* **2010**, *1*, 13–28, doi:10.1016/j.jare.2010.02.002.
180. Qin, H.; Wu, D.; Sathian, J.; Xie, X.; Ryan, M.; Xie, F. Tuning the upconversion photoluminescence lifetimes of NaYF4:Yb3+, Er3+ through lanthanide Gd3+ doping. *Sci. Rep.* **2018**, *8*, 2–9, doi:10.1038/s41598-018-30983-9.
181. Wang, W.; Ding, M.; Lu, C.; Ni, Y.; Xu, Z. A study on upconversion UV-vis-NIR responsive photocatalytic activity and mechanisms of hexagonal phase NaYF4: Yb3+,Tm3+@TiO2 core-shell structured photocatalyst. *Appl. Catal. B Environ.* **2014**, *144*, 379–385, doi:10.1016/j.apcatb.2013.07.035.
182. Li, C.; Wang, F.; Zhu, J.; Yu, J.C. NaYF4:Yb,Tm/CdS composite as a novel near-infrared-driven photocatalyst. *Appl. Catal. B Environ.* **2010**, *100*, 433–439, doi:10.1016/j.apcatb.2010.08.017.
183. Iliev, V.; Tomova, D.; Rakovsky, S.; Eliyas, A.; Puma, G.L. Enhancement of photocatalytic oxidation of oxalic acid by gold modified WO3/TiO2 photocatalysts under UV and visible light irradiation. *J. Mol. Catal. A Chem.* **2010**, *327*, 51–57,

doi:10.1016/j.molcata.2010.05.012.

184. Pap, Z.; Radu, A.; Hidi, I.J.; Melinte, G.; Diamandescu, L.; Popescu, T.; Baia, L.; Danciu, V.; Baia, M. Behavior of gold nanoparticles in a titania aerogel matrix: Photocatalytic activity assessment and structure investigations. *Cuihua Xuebao/Chinese J. Catal.* **2013**, *34*, 734–740, doi:10.1016/s1872-2067(11)60500-7.
185. Rahme, K.; Holmes, J.D. Gold Nanoparticles: Synthesis, Characterization, and Bioconjugation. *Dekker Encycl. Nanosci. Nanotechnology, Third Ed.* **2015**, 1–11, doi:10.1081/e-enn3-120053520.
186. Durán-Álvarez, J.C.; Santiago, A.L.; Ramírez-Ortega, D.; Acevedo-Peña, P.; Castillón, F.; Ramírez-Zamora, R.M.; Zanella, R. Surface modification of B–TiO2 by deposition of Au nanoparticles to increase its photocatalytic activity under simulated sunlight irradiation. *J. Sol-Gel Sci. Technol.* **2018**, *88*, 474–487, doi:10.1007/s10971-018-4815-7.
187. Reddy, K.L.; Kumar, S.; Kumar, A.; Krishnan, V. Wide spectrum photocatalytic activity in lanthanide-doped upconversion nanophosphors coated with porous TiO2 and Ag-Cu bimetallic nanoparticles. *J. Hazard. Mater.* **2019**, *367*, 694–705, doi:10.1016/j.jhazmat.2019.01.004.